SMART HEALTH MONITORING SYSTEM BASED ON FIBER OPTIC SENSORS

LYU WEIMIN

PhD

The Hong Kong Polytechnic University

2025

The Hong Kong Polytechnic University

Department of Electrical and Electronic Engineering

Smart Health Monitoring System Based on Fiber Optic Sensors

LYU Weimin

A thesis submitted in partial fulfillment of the requirements
for the degree of Doctor of Philosophy

July 2024

Certificate of Originality

I hereby declare that this thesis is my own work and that, to the best of my knowledge and belief, it reproduces no material previously published or written, nor material that has been accepted for the award of any other degree or diploma, except where due acknowledgment has been made in the text.

(Signed)

LYU Weimin (Name of student)

Abstract

As the population ages in modern society, people begin to pay attention to daily medical care. There are already some vital sign monitoring products on the market, such as Xiaomi Smart Band, Fitbit Watch, Apple Watch, etc. However, these products are all wearable devices. Not only will wearing it for a long time cause discomfort, but long-term contact measurements may also trigger allergic reactions. BCG, a signal of tiny vibrations in the body caused by the heart's pumping of blood, can be measured non-invasively by FOSs. In this work, a fiber optic interferometer-based BCG monitoring system was developed. During exercise and sleep states, the BCG signal based on the FOS has a high correlation with the reference signal collected by commercial equipment. Through the BCG signal collected by this system, the health status of the heart, such as myocardial contractility and HRV, can be analyzed.

FOSs based on special optical fibers were first proposed for non-contact vital signs monitoring. One is a new online MZI sensor based on self-made SCF, and the other is an SI sensor based on self-made SH-HiBiF. The advantage of the former is that the sensor is simple to manufacture, low in cost, and has high repeatability. The advantage of the latter is that the sensing fiber used is not sensitive to temperature, and the system does not need to use demodulation to solve the signal fading problem. During the experiment, the sensing fiber was packaged under the mattress to monitor vital sign signals for a long time. Through filtering and FFT procedures, accurate RR and HR can be obtained. At the same time, the proposed system can also diagnose premature beats in a non-contact manner with an accuracy of 97.9%.

Furthermore, we also propose a single-mode fiber-based MZI for non-contact vital sign monitoring. The system uses 3×3 coupler demodulation scheme to solve the signal fading problem and can be used stably for a long time. And due to its high sensitivity, this sensor can not only be placed under the mattress for sleep monitoring, but can also be attached to the wrist for pulse diagnosis. The measurement results of RR and HR at rest and during exercise showed high accuracy. This work verifies the feasibility of the proposed system in sleep, pulse diagnosis and driver monitoring applications. And the heart health status is evaluated based on the long-term BCG data collected by the proposed system.

Acknowledgments

At this point, I realize that I am practically done with my PhD study. Here, I would like to extend my heartfelt appreciation to several individuals whose support has been invaluable throughout this process.

Firstly, I am deeply grateful to my supervisor, Prof. YU Changyuan. He provided me with the opportunity to join his research group during my master's degree and allowed me to stay in his group as a research assistant after my graduation. He has helped me a lot in my study and life during this special and challenging COVID-19 era. As my mentor, Prof. Yu taught me a lot in terms of research direction and social skills. I am very lucky and glad to be able to work under the guidance of Prof. Yu.

Additionally, I formed many valuable friendships at PolyU, which greatly supported me throughout my PhD journey. Their assistance was crucial in enabling me to complete my research efficiently. I am particularly thankful to Dr. TAN Fengze and Dr. CHEN Shuyang for their significant help at the beginning of my PhD studies. I would also like to thank Dr. WANG Zhuo, Dr. YUAN Weihao, Dr. WANG Yu, Dr. YAN Yaxi, Dr. LUO Huaijian, Dr. YANG Zongru, Dr. QU Jiaqi, Dr. LIU Yifan, Mr. LIU Zhongxu, Mr. Li Yujian, Mr. CHEN Jiajian, Mr. ZHOU Jing, Mr. YU Jianxun, Mr. CHENG Zhi, Miss WANG Yue, Mr. ZHANG Jingming, Mr. CUI Mingjie, Mr. XU Pin, Mr. WANG Qing, and Miss. WANG Xiuyuan.

Finally, I wish to express my deepest gratitude to my parents, Mr. LYU Xiangzhi and Ms. ZHONG Jie, for their unwavering support and encouragement

throughout my life and academic journey. Since my childhood, they have provided me with a relaxed living environment and unconditional support for my choices. I am also immensely thankful to my wife, Ms. WEI Qian. Even though we were separated for most of the years while I was pursuing my PhD degree, she remained fully supportive of me. Completing my PhD would not have been possible without the wholehearted backing of my family.

LYU Weimin
The Hong Kong Polytechnic University
July 2024

Publications

Journal:

1. Y. Huang, L. Chen, C. Li, J. Peng, Q. Hu, Y. Sun, H. Ren, ***W. Lyu***, W. Jin, J. Tian, C. Yu, W. Cheng, K. Wu, and Q. Zhang, "AI-driven System for Non-contact Continuous Nocturnal Blood Pressure Monitoring Using Fiber Optic Ballistocardiography," Communications Engineering, vol. 3, no. 1, pp. 183–11, 2024.
2. Y. Li, P. Xu, ***W. Lyu***, Y. Liu, and C. Yu, "Fiber Lateral Stress Sensor Based on Michelson Interference and Optical Vernier Effect," Journal of Lightwave Technology, vol. 42, no. 18, pp. 6219–6224, 2024.
3. ***W. Lyu***, W. Yuan, J. Yu, Q. Wang, S. Chen, J. Qin, and C. Yu, "Non-contact Short-term Heart Rate Variability Analysis under Paced Respiration Based on a Robust Fiber Optic Sensor System," IEEE Transactions on Instrumentation & Measurement, vol. 73, pp. 1–13, 2024.
4. L. Wang, H. Li, Y. Yao, D. Han, C. Yu, ***W. Lyu***, and H. Wu, "Smart Cushion-based Non-invasive Mental Fatigue Assessment of Construction Equipment Operators: A Feasible Study," Advanced Engineering Informatics, vol. 58, pp. 102134, 2023.
5. S. Chen, H. Luo, ***W. Lyu***, J. Yu, J. Qin, and C. Yu, "A Compressed Sensing Framework for BCG Signals Based on The Optical Fiber Sensor," Optics Express, vol. 31, no. 18, pp. 29606-29618, 2023.

6. Q. Wang, ***W. Lyu***, J. Zhou, and C. Yu, “Sleep Condition Detection and Assessment with Optical Fiber Interferometer Based on Machine Learning,” iScience, vol. 26, no. 7, pp. 107244–107244, 2023.
7. Q. Wang, ***W. Lyu***, S. Chen, and C. Yu, “Non-Invasive Human Ballistocardiography Assessment Based on Deep Learning,” IEEE Sensors Journal, vol. 3, no. 12, pp. 13702 – 13710, 2023.
8. Q. Wang, ***W. Lyu***, Z. Cheng, and C. Yu, “Noninvasive Measurement of Vital Signs with the Optical Fiber Sensor Based on Deep Learning,” Journal of Lightwave Technology, vol. 41, no. 13, pp. 4452–4462, 2023.
9. S. Chen, F. Tan, ***W. Lyu***, H. Luo, J. Yu, J. Qu, and C. Yu, “Deep Learning-based Ballistocardiography Reconstruction Algorithm on the Optical Fiber Sensor,” Optics Express, vol. 30, no. 8, pp. 13121-13133, 2022.
10. F. Yang, W. Xu, ***W. Lyu***, F. Tan, C. Yu, and B. Dong, “High Fidelity MZI-BCG Sensor With Homodyne Demodulation for Unobtrusive HR and BP Monitoring,” IEEE Sensors Journal, vol. 22, no. 8, pp. 7798–7807, 2022.
11. ***W. Lyu***, S. Chen, F. Tan, and C. Yu, “Vital Signs Monitoring Based on Interferometric Fiber Optic Sensors,” Photonics, vol. 9, no. 2, pp. 50, February 2022.
12. ***W. Lyu***, W. Xu, F. Yang, S. Chen, F. Tan, and C. Yu, “Non-invasive measurement for cardiac variations using a fiber optic sensor,” IEEE Photonics Technology Letters, vol. 33, no. 18, pp. 990-993, September 2021.

13. S. Chen, F. Tan, ***W. Lyu***, and C. Yu, “Ballistocardiography Monitoring System Based on Optical Fiber Interferometer Aided with Heartbeat Segmentation Algorithm,” Biomedical Optics Express, vol. 11, no. 10, pp. 5458-5469, October 2020.
14. F. Tan, ***W. Lyu***, S. Chen, Z. Liu, and C. Yu, “Contactless Vital Signs Monitoring Based on Few-mode and Multi-core Fibers,” Opto-Electronic Advances, vol. 3, no. 5, Paper 190034, pp. 1-2, May 2020.
15. F. Tan, S. Chen, ***W. Lyu***, Z. Liu, C. Yu, and H.Y. Tam, “Non-invasive Human Vital Signs Monitoring Based on Twin-core Optical Fiber Sensors,” Biomedical Optics Express, vol. 10, no. 11, pp. 5940-5952, November 2019.

Conference paper:

1. T. Chen, ***W. Lyu,*** S. Chen, and C. Yu, “A Real-Time Sleep Monitoring System Based on Fiber Optic Sensor,” Asia Communications and Photonics Conference and Exhibition (ACP) 2024, pp. 1-4, Beijing, China, November 2-5, 2024, (**Best Student Paper Award**).
2. ***W. Lyu***, S. Chen, W. Yuan, Y. Li, Q. Wang, and C. Yu, "Non-contact Short-term HRV Analysis of Patients with Premature Beats Based on a Fiber Optic Sensor,” 28th International Conference on Optical Fiber Sensors (OFS) 2023, pp. Tu4-2, Hamamatsu, Japan, November 20-24, 2023, ***(Oral presentation)***.
3. Y. Li, P. Xu, ***W. Lyu***, Y. Liu, and C. Yu. "Optical Fiber Lateral Stress Sensor Based on Michelson Interference and Optical Vernier Effect." 8th

International Conference on Optical Fiber Sensors (OFS) 2023, pp. Th6-49, Hamamatsu, Japan, November 20-24, 2023.

4. Q. Wang, ***W. Lyu***, J. Zhou, and C. Yu. "A Novel Machine Learning-Based Framework for Human Vital Sleep Assessment with Optical Fiber Interferometer." 28th International Conference on Optical Fiber Sensors (OFS) 2023, pp. Tu3-94, Hamamatsu, Japan, November 20-24, 2023.
5. Y. Li, ***W. Lyu***, Z. Liu, Yuan W, and C. Yu, “Optical Fiber Gas Pressure Sensor Based on the Michelson Interferometer with Optical Vernier Effect,” 28th International Conference on Optical Fiber Sensors (OFS) 2023, pp. W4-58, Hamamatsu, Japan, November 20-24, 2023.
6. ***W. Lyu***, S. Chen, Z. Liu, P. Xu, Y. Li, and C. Yu, "Non-invasive Vital Signs Monitoring and Premature Beats Recognition System Based on a Six Holes High Birefringence Fiber, OFS, accept.
7. Y. Li, ***W. Lyu***, Y. Li, Q. Wang, X. Wang, W. Yuan, and C. Yu, "A Gas Pressure Sensor Based on Optical Fiber Fabry-Perot Interference," In 2023 Asia Communications and Photonics Conference/2023 International Photonics and Optoelectronics Meetings (ACP/POEM), pp. 1-3, Wuhan, China, November 4-7, 2023.
8. Q. Zhang, ***W. Lyu***, Q. Wang, and C. Yu, "A Deep Learning-Based Model for Human Non-Invasive Vital Sign Signal Monitoring with Optical Fiber Sensor," In 2023 Asia Communications and Photonics Conference/2023 International Photonics and Optoelectronics Meetings (ACP/POEM), pp. 1-4, Wuhan, China, November 4-7, 2023.

9. Y. Chen, ***W. Lyu***, W. Yuan, and C. Yu, "Smart Health Monitoring System Based on a Fiber Optic Sensor," In 2023 Asia Communications and Photonics Conference/2023 International Photonics and Optoelectronics Meetings (ACP/POEM), pp. 1-3, Wuhan, China, November 4-7, 2023, **(Best Poster Award)**.
10. Y. Li, ***W. Lyu***, Y. Liu, and C. Yu, "Acoustic Wave Sensor Based on the Optical Fiber-Diaphragm Composite Structure," 2023 Photonics Global Conference (PGC), pp. 67-70, Stockholm, Sweden, August 21-23, 2023.
11. ***W. Lyu***, J. Yu, Q. Wang, S. Chen, Y. Li, and C. Yu, "Drivers' Heart Rate Monitoring System Based on Dual Fiber Optic Sensors," 2023 Photonics Global Conference (PGC), pp. 74-76, Stockholm, Sweden, August 21-23, 2023.
12. ***W. Lyu***, Y. Li, S. Chen, Q. Wang, and C. Yu, "Short Time HRV Assessment Based on a Fiber Optic Sensor," in 2023 Conference on Lasers and Electro-Optics Europe & European Quantum Electronics Conference (CLEO/Europe-EQEC), Paper cl_p_7, Munich, Germany, June 26 – 30, 2023.
13. ***W. Lyu***, Y. Yan, J. Yu, S. Chen, C. Yu, C. Lu, and A. P. T. Lau, "Measurement of Wrist Pulse Using Fiber Optic MZI for Analysis of Heart Rate and Respiration Rate." In TENCON 2022-2022 IEEE Region 10 Conference (TENCON), pp. 1-3, Hong Kong, November 1-4, 2022.
14. S. Chen, F. Tan, ***W. Lyu***, and C. Yu, "Ballistocardiography Reconstruction Based on Optical Fiber Sensor Using Deep Learning Algorithm,"

Optoelectronics and Communications Conference (OECC) 2021, Paper T3F.5, pp. 1-3, Hong Kong, China, July 3-7, 2021.

15. ***W. Lyu***, S. Chen, F. Tan, and C. Yu, "Non-invasive Heart Rate Variability Measurement During Sleep Based on Fiber Optic Sensor," Optoelectronics and Communications Conference (OECC) 2021, Paper JS3F.2, pp. 1-3, Hong Kong, China, July 3-7, 2021.
16. F. Yang, ***W. Lyu***, C. Pan, S. Yang, F. Tan, S. Chen, and C. Yu, "Contactless Vital Signs Monitoring Based on Optical Fiber Mach-Zehnder Interferometer Aided with Passive Homodyne Demodulation Methods," Asia Communications and Photonics Conference and Exhibition (ACP) 2020, Paper M4A.79, pp. 1-3, Beijing, China, October 24-27, 2020.
17. S. Chen, F. Tan, ***W. Lyu***, and C. Yu, "A Ballistocardiography Monitor Based on Optical Fiber Interferometer," Photonics Asia 2020, Paper 11547-58, pp. 1-6, Beijing, China, October 11-16, 2020.
18. C. Yu, F. Tan, S. Chen, ***W. Lyu***, X. Zhu, and J. Luo, "Bionic Palpation Based on Optical Fiber Sensor," 5th Optoelectronic Global Conference (OGC) 2020, pp. 1, Shenzhen, China, September 7-11, 2020.
19. ***W. Lyu***, F. Tan, S. Chen, and C. Yu, "Myocardial Contractility Assessment Using Fiber Optic Sensors," Asia Communications and Photonics Conference and Exhibition (ACP) 2019, Paper M4A.152, pp. 1-3, Chengdu, China, November 2-5, 2019.

Contents

List of Abbreviations

A	
AHA	American Heart Association
AF	Atrial fibrillation
ANS	Autonomic nervous system
B	
BCG	Ballistocardiography
BP	Blood pressure
BPF	Band-pass filter
C	
CVDs	Cardiovascular disease
COPD	Chronic obstructive pulmonary disease
CO	Cardiac output
D	
DAQ card	Data acquisition card
DFB laser	Distributed feedback laser
DSE	Dynamic squat exercise
E	
ECG	Electrocardiography
EMFi	Electromechanical film
EMI	Electromagnetic interference
EEG	Electroencephalogram
F	

FBG	Fiber Bragg grating
FPI	Fabry-Perot interferometer
FOS	Fiber optic sensor
FMF	Few-mode fiber
FFT	Fast Fourier transform
FSR	Free spectral range
G	
Ge	Germanium
H	
HR	Heart rate
HRV	Heart rate variability
HF	High frequency
HPF	High-pass filter
I	
IoT	Internet of things
IBI	Interbeat interval
IoMT	Internet of medical things
IRG	Impedance respirography
ICG	Impedance cardiography
L	
LED	Light-emitting diode
LPF	Low-pass filter
LVET	Left ventricular ejection time
LF	Low frequency

LBNP	Lower body negative pressure
M	
MZI	Mach-Zehnder interferometer
MI	Michelson interferometer
MRI	Magnetic resonance imaging
MMF	Multi-mode fiber
MCF	Multi core fiber
MCU	Microcontroller unit
P	
PEP	Pre-ejection period
PTT	Pulse transit time
PD	Photodetector
PPG	Photoplethysmography
PZT	piezo-electrical transducer
PSD	Power spectral density
PID	Proportional-integral-derivative
PSG	Polysomnography
PNS	Parasympathetic nervous system
PCF	Photonic crystal fibers
PWV	Pulse wave velocity
Q	
Q-point	Quadrature point
R	
RES exercise	Respiration exercise

RMS	Root mean square
RI	Refractive index
RR	Respiratory rate
RSA	Respiratory sinus arrhythmia
S	
SCF	Seven-core fiber
SI	Sagnac interferometer
SNR	Signal-to-noise ratio
SMF	Single-mode fiber
SEM	Scanning electron microscope
SVM	Support vector machine
SH-HiBiF	Six-hole high birefringence fiber
SNS	Sympathetic nervous systems
SV	Stroke volume
SBP	Systolic blood pressure
T	
TCF	Twin core fiber
TL	Tunable laser
V	
VCSEL	Vertical-cavity surface-emitting laser
VAD	Vapor axial deposition
VM	Valsalva maneuver
VLF	Very low frequency
W	

WDM	Wavelength division multiplexing

List of Figures

List of Tables

Chapter 1

Introduction

1.1 Overview and research motivations

In recent decades, with the steady growth of income, people's living standards have gradually improved. Increasing work pressure has led to a decline in physical health, which has gradually increased people's health awareness. People are willing to buy some health monitoring devices to record their daily health conditions. HR, RR, blood oxygen, BP, body temperature, etc., are indicators that reflect human health. Among these vital sign indicators, HR and RR are particularly important due to their close association with chronic diseases such as CVD and COPD [1]. Daily vital sign monitoring can help to evaluate people's health status, which is of great significance in many healthcare applications. Due to increasing concerns about health issues, researchers are interested in developing user-friendly and convenient methods for monitoring vital signs. CVD has become the leading single cause of death in developed countries, accounting for more than 30% of all deaths in most countries. The AHA reports that CVD was responsible for approximately 19.05 million deaths worldwide in 2020.

Additionally, one in three people die from cardiovascular-related diseases [2]. Long-term service is indispensable for HR and RR monitoring, whether in clinical or home applications. Vital sign monitoring equipment is particularly necessary in areas with an aging population and scarce medical resources.

In order to provide more convenient vital sign monitoring, many devices have been developed and widely used in daily life. The most commonly used cardiac monitoring device in the current healthcare system is the ECG device [2]. The heart's electrical signals can be collected by attaching several electrodes to the chest, abdomen, and limbs. In addition to ECG, PPG is a common heartbeat measurement method, and the pulse signal can be obtained by clipping a pulse oximeter on the finger [3]. The measurement principle of PPG devices is to analyze cardiac information by collecting changes in reflected or transmitted light intensity on the skin. Spirometry, capnometry, and impedance pneumography are commonly used methods for respiratory monitoring [4]. However, traditional medical devices have some limitations that need to be addressed. During the ECG measurement process, several patches need to be attached to the body, which can cause discomfort to the user. PPG is also a contact measurement method. Clamping the finger with the device for a long time will cause poor blood flow. Spirometry interferes with the natural respiration of users, making continuous respiration monitoring difficult. As a contact measurement method, capnography also causes discomfort to the users. IRG requires the use of special equipment for analysis, resulting in high costs.

Therefore, these HR and RR measurement devices cannot meet the needs of daily use at home. BCG reflects information about the vibration of the heart without attaching any patches to the body. At the same time, respiratory information can also be obtained from the BCG raw data. Taking advantage of the difference in heartbeat and respiratory rates, simultaneous monitoring of HR and RR can be achieved through a single monitoring system.

BCG is a biomedical signal reflecting the body recoils in reaction to heart ejection during each cardiac cycle, in which the body recoils refer to global movements of the body. It is a combination of multiple forces including blood flow within the heart, blood flow within arteries (mainly the aorta), and heart movement. BCG signals can be detected via non-invasive and non-wearable means [4]. Many research groups have explored various sensing schemes to track the BCG waveform. Among them, electronic sensors are the most common type adopted to fabricate the BCG monitor. In 2006, Alametsä et al. recorded BCG signals with an EMFi sensor and assessed the severity of breathing disturbances during sleep [5]. They embedded the EMFi sensor into the cushion and users could obtain the heartbeat signal when they sat on the cushion. Subsequently, in 2011, Wiard et al. applied a designed bathroom scale to measure BCG and improve the SNR [6]. Users could obtain their BCG signal by standing on the scale and keeping still. In addition, remote vital signs monitoring based on video or radar technologies has also caused much concern in recent years. In 2017, Hassan et al. proposed a camera-based robust BCG monitoring system by measuring head movement [7]. They obtained the approximative BCG signals by estimating the face's microscopic color change or rigid motion. More recently, in 2020, Cimr et al. measured a quantity correlated with the PWV by using the Cartan curvature and transformed it into direct BP measurement by using the Moens–Korteweg relation [8]. Though these technologies provide feasible schemes to monitor heartbeat or breath, some drawbacks will greatly reduce the performance of sensors. For example, the limited sensitivity could result in the loss of details in biomedical signals, and EMI can also affect performance. In addition, for video or radar technologies-based remote health monitoring, motion artifacts will introduce large errors into the monitoring systems.

Optical fiber-based sensors as a novel sensing technology own many merits, including low cost, high sensitivity, electrical isolation, and immune to EMI, which is intrinsically safe and reliable. Optical fiber-based sensing technologies have been widely used in strain [9], humidity [10], temperature [11], acceleration [12], and RI [13] measurements. In addition, there are several vital signs monitors based on different types of FOS. For example, X. Yang et al. built a wearable textile micro-bend FOS to monitor HR and RR based on the principle of micro-bend loss [14]. Ł. Dziuda et al. developed an FBG strain sensor to acquire HR and RR information of the user during MRI survey [15]. However, the mentioned FOS technologies have some defects: the sensitivity of the micro-bend loss-based sensing method is limited and the demodulation equipment of FBG is expensive. To address these problems, we pay more attention on the phase-based FOS.

For optical fiber interferometers, the signal fading problem makes it unsuitable for long-term use. Numerous modulation and demodulation schemes, including the PGC demodulation method [16] and PZT phase modulation method [17], can be used to solve this limitation, but they have significant limitations for BCG monitoring. Signal generators and PZT modulation devices are too bulky to be integrated into the compact vital signs monitoring system.

In this thesis, the BCG monitoring system based on different fiber optic interferometers is proposed to obtain long-term, real-time, stable, and accurate BCG signals. The high-quality BCG signals collected through this system are then used in cardiac health assessment, sleep monitoring, driver monitoring, etc. This long-term and real-time BCG monitoring system has tremendous potential in future healthcare applications.

1.2 BCG signal and applications

1.2.1 Overview

The BCG signal reflects the subtle vibrations of the human body caused by each heartbeat and is able to be obtained in a non-contact method through highly sensitive sensors [18]. Gordon first observed this phenomenon in 1877. He discovered that while standing on a scale, the hands deflected on either side of the dial with every heartbeat [19]. In 1939, an instrument for measuring this signal was developed by Starr et al. [18]. However, due to limitations of measurement technology, BCG-related technologies were not further studied. In the past decade or so, BCG has regained the favor of researchers with its increasingly mature sensing and signal processing technology.

The blood travels along the vascular with each heartbeat, which causes changes in the body’s center of mass. Then, tiny body movements caused by recoil forces can maintain the overall momentum. BCG is a recording of these movements, and it can be obtained as displacement, velocity, or acceleration information. BCG can be divided into longitudinal and transverse BCG depending on the movements in different directions. The longitudinal BCG represents vibrations in the head-to-foot direction, while the transverse BCG represents vibrations in the dorsoventral direction. The longitudinal BCG is the maximum projection of 3-D forces caused by cardiac ejection. However, for some measurement methods, forces from multiple directions are inevitably mixed. Despite the 3-D nature of BCG, researchers have primarily studied longitudinal BCG. The main measurements of longitudinal BCGs were based on force sensors placed on chairs or weighing scales, and thus the subject could be in a vertical position to detect the change of head-to-foot force. Subsequently, lots of bed-based sensors were widely studied to detect transverse BCG successfully.

BCG waveform is generated with each cardiac contraction, and each waveform owns several peaks and valleys, as shown in Fig. 1.1. A complete BCG waveform records several peaks, mainly including H, I, J, K, and L peaks with different amplitudes. These peaks reflect the pumping status of the heart. For example, the amplitude of the IJK complex can reflect aortic pulse pressure [20]. J peaks of BCG can be used to estimate HR and HRV of the subject, which has great potential in cardiac health care.

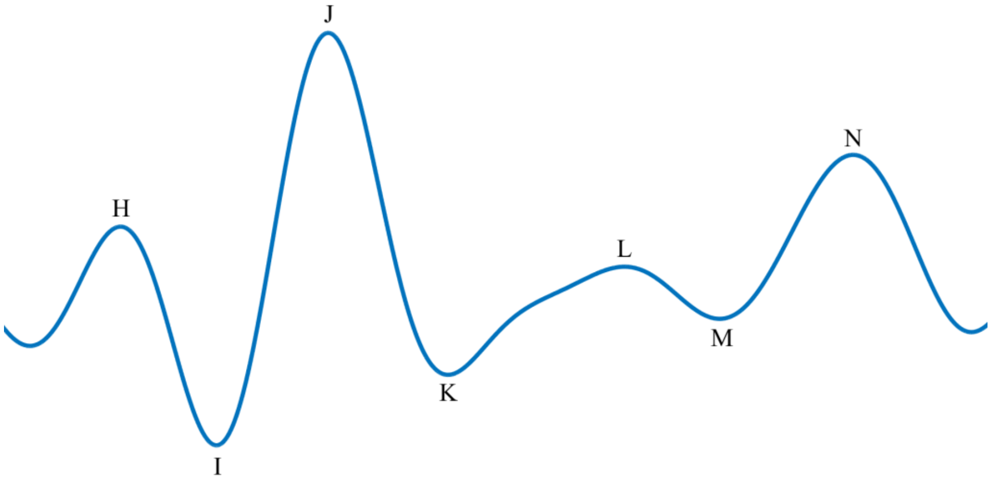

Fig. 1.1. A typical BCG waveform.

1.2.2 Measurement methods

The currently widely investigated BCG detection systems are mainly based on weighing scales, beds, and chairs.

The weighing scale-based BCG system was first proposed by Jim Williams et al. in 1990, which was based on an electronic scale [21]. They built a high-precision electronic scale and then found the motion artifacts during the measuring process, which is mainly composed of the BCG signal. The standing posture of the subject guarantees the measured BCG is completely longitudinal, which is the main advantage of this type of measurement. Moreover, since weighing scales are a common household device, it is easy to popularize this heartbeat monitoring system by enhancing the capabilities of the traditional weighing scale. Therefore, many researchers have investigated this BCG measurement. In 2009, O. T. Inan et al. proposed a BCG monitoring system based on a modified weighing scale [22]. Gonzalez-Landaeta et al. [23] and Shin et al. [24] have also successfully built BCG monitors based on weighing scales. The BCG signals collected by their system have a similar shape and amplitude to the recordings detected by Starr et al. At the same time, however, this kind of measurement also exists the issue of being susceptible to motion artifacts and environmental disturbances. In addition, the weighing scale-based BCG system also limits the duration of the measurement since it is uncomfortable for the subject to stand still on the scale for a long time, especially for a patient.

Bed-based BCG systems can access the BCG signals during sleep, which can be used in the evaluation of sleep stages and sleep-related disorders. Since the BCG devices do not need to attach electrodes to the skin of subjects, they will not disturb the sleep behaviors of subjects compared to ECG devices during the data collection stage. Bed-based BCG systems can be integrated with the sleeping environment based on different types of sensors. Alihanka et al. proposed a static charge-sensitive bed in 1981, which was the first time such a bed-based BCG sensor has been proposed [25]. Subsequently, film-type force sensors [26], EMFi sensors [27], piezoelectric film sensors [28], polyvinylidene fluoride sensors [29], and hydraulic sensors [30] have been proposed to detect BCG on the bed. In addition, sensor arrays have been developed to replace the single sensor to improve performance [31]. These sensors can not only detect heartbeat signals, but also other physiological information such as respiration signals and body movements, which can be used to improve the accuracy of sleep analysis.

Chair-based BCG systems can obtain the BCG in the sitting position. Walter et al. proposed an EMFi sensors-based BCG monitor embedded in the driver’s seat in the car, which could be used to monitor the fitness of the driver [32]. J. Alamesa et al. developed an EMFi-based seated BCG monitoring device and demonstrated a better performance than acceleration sensor-based BCG monitoring devices. [33]. In general, chair-based BCG monitors provide a heartbeat monitoring way during the day, and they can work with bed-based BCG monitors to realize a sound cardiac health monitoring system in daily life. However, chair-based BCG signals own less signal amplitude compared to bed-based BCG and weighing-scale-based BCG signals, which need more sensitive sensors to detect.

1.2.3 BCG applications

Initially, BCG was proposed as a clinical diagnostic tool, and doctors could make diagnoses of patients' cardiovascular health based on BCG records [34,35]. However, large inter-subject variability in the BCG signal hampered the continuation of this proposal. In contrast, studies have shown that the variability of serially measured signals across subjects is actually low unless cardiovascular health changes [36]. Therefore, BCG has been proposed as a tool to monitor changes in the cardiovascular status of the same patient over time.

To reveal the correlation between BCG signal characteristics and clinical diseases, large number of researchers have conducted studies on healthy subjects using modern instrumentation and analytical tools. They primarily use non-invasive protocols to alter cardiac hemodynamics and time intervals, such as running, VM, whole-body tilt test, or LBNP, and then compare changes in BCG to changes in gold standard measurements (e.g. ICG or Doppler ultrasound).

Many researchers have examined the signal itself as well as the time intervals between BCG characteristics and other physiological signals (such as ECG or PPG) in an attempt to find correlations between these time intervals and well-known parameters (such as PEP, PTT or LVET). PEP is usually measured by ICG, which characterizes myocardial contractility. The time interval between the R peak of the ECG and the J peak of the BCG has been suggested as a reference for PEP assessment [37,38]. These researchers used the VM and whole-body tilt test to alter the autonomic balance between the SNS and PNS to modulate PEP. They compared the measured RJ interval with PEP measured using ICG to assess the feasibility of the RJ interval as a surrogate for PEP. Etemadi et al. illustrated a strong correlation between RJ interval and PEP for 2126 beats in 10 subjects performing the VM [38]. He et al. reached similar conclusions with the VM and whole-body tilt test in one subject [37].

The amplitude component of BCG has been found to change with the variations in left ventricular function, specifically variations in SV or CO. After studying 275 data points in 9 subjects, Inan et al. verified that exercise-induced RMS power changes measured during a 10-min recovery period were closely related to CO changes measured by Doppler ultrasound [39].

Pinheiro et al. suggested using BCG and PPG for PTT estimation and extracting BP-related information through the known relationship between PTT and PWV [40]. Shin et al. revealed a strong correlation between RJ interval and SBP by comparing RJ interval using VM-modulated BCG with beat-to-beat SBP using the Finapres system [41]. Nevertheless, Casanella et al. found that the correlation between RJ interval and SBP was not always observed in the context of hemodynamic changes caused by paced respiration, and this phenomenon depended on the subject [42]. Winokur et al. found that the time interval between the BCG and PPG collected from subject's ears correlates with PTT, which can be used to estimate BP [43].

LVET is another health parameter, which expresses the duration of systolic ejection. Javaid et al. used a wearable BCG device to measure contraction intervals during walking at different speeds [44]. Using pattern matching techniques and multi-sensor data fusion, they demonstrated good correlations between PEP from the gold standard ICG and BCG features, and also between LVET from both modalities.

1.3 Optical fibers and fiber optic sensors

1.3.1 Overview

Optical fibers were first invented by K. C. Kao in 1966, which is a dielectric waveguide operating in the optical band [45]. The RI of the core in an optical fiber is higher than that of the cladding, which enables the transmission of energies at optical frequencies to travel in optical fibers according to the total internal reflection phenomenon. Optical fibers have been extensively studied since then, and SMFs have been produced for use in practical communication systems.

An optical fiber consists of a core, cladding, and coating. The cladding surrounds a silica glass core. According to the variation of RI, optical fiber is divided into step-index fibers and graded-index fibers. Step-index fibers have an abrupt RI change at the core-cladding interface while the RI of the core reduces gradually and then is equal to that of the cladding at the interface in graded-index fibers. The cross-section and the corresponding index profile of two kinds of optical fiber are shown in Fig. 1.2. a and b are radius and n_1 and n_2 are the RIs of the core and cladding. Generally, a and b are 8 μm and 125 μm in the SMF. Other than the common SMF, several structures of optical fibers are designed and fabricated based on various requirements, such as FMFs [46], MMFs [47], MCFs [48], and PCF [49].

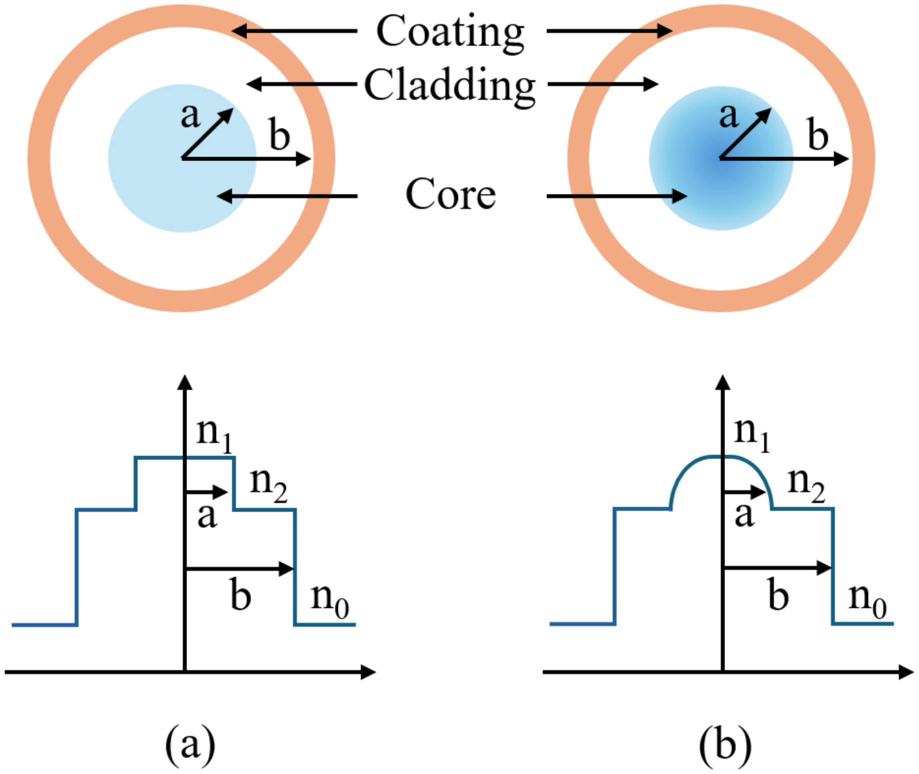

Fig. 1.2. The cross-section and the corresponding index profile of (a) step-index fiber and (b) graded-index fiber.

Optical fibers have been used worldwide in communications due to the intrinsic merits of long transmission distance, large information capacity, lightweight, immunity to EMI, and safety. With the development of optical fiber technology, optical fibers have also been investigated and utilized in the application of sensing. FOSs have been demonstrated to be available for strain, temperature, acceleration, and RI sensing. The principle of FOSs is that the light from a laser or LED propagates through the optical fiber and is modulated by measured parameters in the sensing area. The characteristics of light, like optical intensity, wavelength, frequency, phase, and polarization state, will be changed. The formed modulated signal can be delivered to the demodulation system to obtain the measured parameter. At present, FOSs have been widely used in the field of well logging technology [50], medical applications [51], and structure health monitoring [52]. Furthermore, an FOS can be utilized in many extreme conditions, such as high temperature [53] and intensity magnetic field [54], owing to its remarkable properties of which.

As mentioned, variational measured parameters can change the optical properties of light. Therefore, there are several types of FOSs based on different principles including intensity-based, wavelength-based, and phase-based, which will be introduced briefly in the following part.

1.3.2 Fiber optic sensors

For intensity-based FOSs, the optical intensity will change with the measured parameter, and variation of the transformed electrical signal from the PD is related to the measured parameter. There are several types of intensity-based sensors. The first type is based on the transmission/reflection light. The example illustrated in Fig. 1.3(a) is a displacement FOS based on transmission light [55]. The light intensity can change with the lateral displacement between the sensing arm and the reference arm. The second type is utilizing the principle of bending loss. Fig. 1.3(b) is a micro-bend FOS [56]. Cyclic bending of optical fiber resulting from comb deformer with fixed spatial period can convert part of guided modes to radiation modes, which changes the light intensity. The third type is based on the varying refraction index. Fig. 1.3(c) is a liquid-level detector [57] using an optical fiber and a prism. When the probe enters the liquid, the light intensity can change with the variational critical angle. The device is used to detect the RI of the liquid.

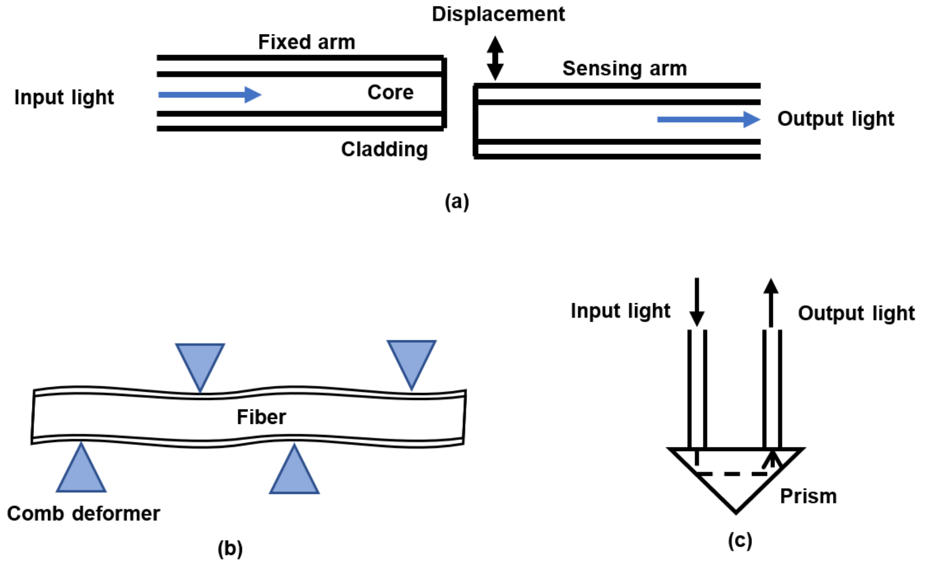

Fig. 1.3. (a) Fiber-optic displacement sensor. (b) Micro-bend fiber-optic sensor. (c) Liquid level detector.

As long as the measurement parameter changes, the changes of light wavelength can be detected by the PD of the wavelength-based fiber optic sensor. The most widely used of these sensors is FBG, which has periodical perturbation of the RI in the fiber core. Variations in RI can be achieved by exposing the core to a strong ultraviolet energy interference pattern. In fact, it can be thought of as a distributed Bragg reflector, reflecting light of specific wavelengths and transmitting all other wavelengths [58]. This is achieved by the grating period, which will lead to a specific wavelength dielectric mirror. Based on FBG's ability to transmit and reflect specific wavelengths, it can be used not only as a filter but also as a mirror. Fig. 1.4 shows the principle of FBG.

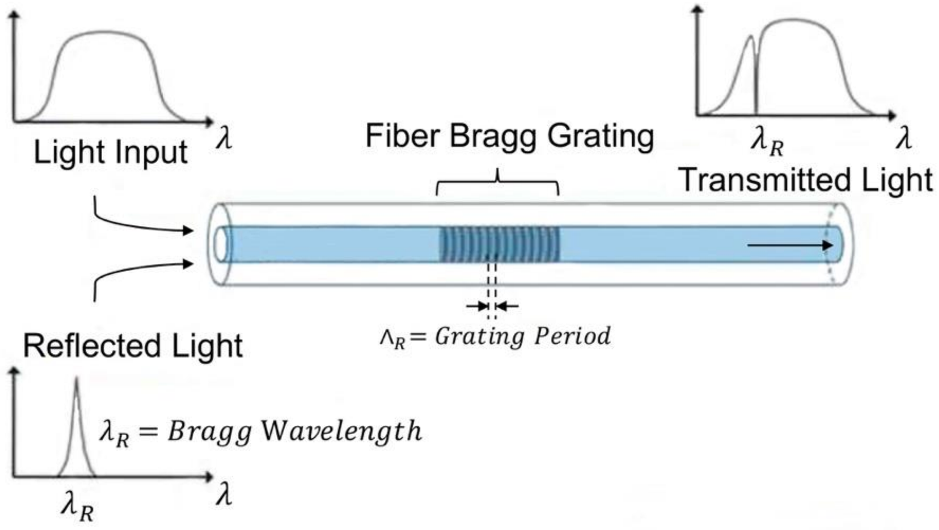

Fig. 1.4. The principle of FBG-based sensor.

FBG-based sensor has high sensitivity and can realize multi-point measurement within one optical fiber. Thus, it is ideal for measuring temperature, strain, pressure, and sound waves [59,60]. The main advantage is that the information being measured is wavelength-encoded, giving the sensor a self-referencing function that is immune to fluctuating light levels and other sources of optical noise. Benefiting from the inherent wavelength characteristics of FBG, even if the light intensity is lost or attenuated due to the optical fiber during transmission, the sensor measurement results can still remain accurate. [61-63].

For phase-based FOS, phase variation cannot be obtained directly by PD. Therefore, interferometers are utilized to convert phase change into optical intensity variation. There are several typical types of interferometers. The first one is a fiber-optic MI [64], as shown in Fig. 1.5(a). Two mirrors are placed at the end of the sensing arm and reference arm, respectively. The phase of sensing light can change with measured parameters. Two reflected light form interference at the coupler and the varying light beam can propagate back to PD. Fig. 1.5(b) shows the structure of fiber optic MZI [65]. The light beam is split into two paths by the first coupler and transmitted in the sensing arm and the reference arm, respectively. the two modulated light beams are coupled at the second coupler, and interference light intensity can be obtained by PD. The third type is a fiber optic FPI [66], which is shown in Fig. 1.5(c). A microcavity is fabricated by coating two high reflection films in the fiber, as shown in Fig. 1.5(d), and then multiple reflective lights generate interference in the optical fiber. The length of microcavity changes with the measured parameter and the variational light intensity can be obtained in the PD.

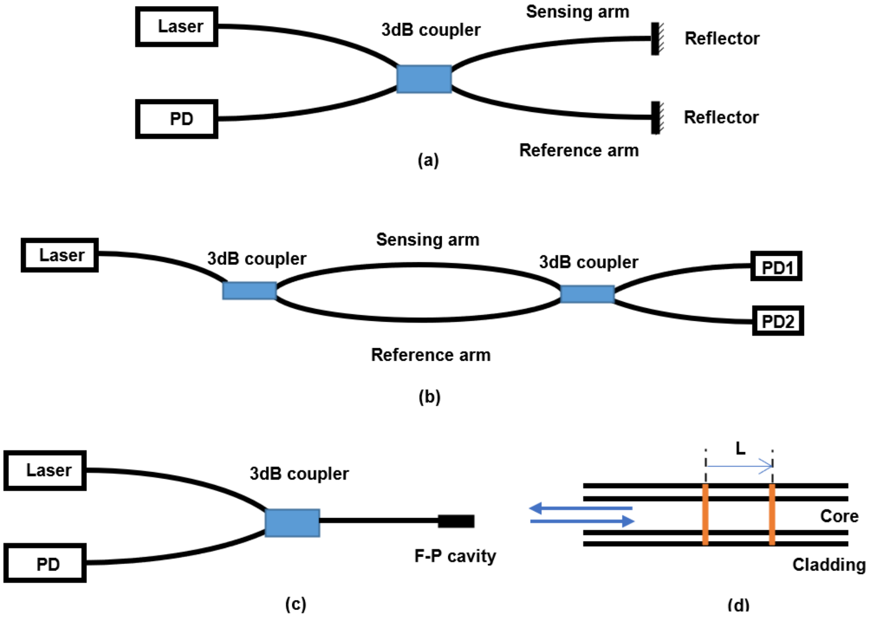

Fig. 1.5. (a) Fiber optic MI. (b) Fiber optic MZI. (c) Fiber optic FPI. (d) Microcavity.

1.4 Research objectives

The research goal of this study is to develop an intelligent health monitoring system based on FOS, which can be summarized as follows:

- Verify the feasibility of FOS based on special optical fibers for vital signs monitoring.
- Construct a robust real-time vital sign monitoring system based on the fiber optic interferometer for daily use. And the 3×3 coupler demodulation method is used to solve the signal fading problem that seriously affects the signal quality in the fiber interferometer.
- Apply the proposed vital signs monitoring system in different scenarios (such as sleep monitoring, pulse detection and driver monitoring).
- Analyze cardiac health status (such as PEP, HRV) based on the proposed vital signs monitoring system.

1.5 Organization of this thesis

This thesis mainly investigates the vital signs monitoring system based on FOS. The research contributions have been illustrated in the following chapters:

Chapter 1 gives an overview of this thesis.

Chapter 2 introduces the application of special optical fibers in vital sign monitoring.

Chapter 3 proposes a robust FOS system based on MZI, which can obtain high-quality vital sign signals stably over a long period of time.

Chapter 4 verifies the feasibility of robust FOS for practical applications in sleep monitoring, pulse monitoring, and driver monitoring.

Chapter 5 demonstrates the application of FOS-based BCG signal in cardiac health analysis.

Chapter 6 Summarizes the research works and possible suggestions for the future work.

Chapter 2

Special optical fiber-based vital signs monitoring sensor

2.1 Introduction

Population aging has become an unavoidable trend around the world, placing increasing medical and nursing pressure on individuals and governments [67]. CVDs have become one of the leading causes of death worldwide over the past decade. Most heart diseases are chronic diseases, often accompanied by symptoms of cardiac arrhythmias [68]. The premature beat is a type of arrhythmia, which is a beat that occurs earlier than expected [69]. Therefore, accurate recognition can provide valuable assistance to physicians in diagnosis. Not only can it help with early diagnosis of heart diseases, but it can also provide patients with targeted treatment option. In today's society, young people are under tremendous work and life pressure, and they face a high incidence of disease [70]. Timely diagnosis and early treatment of chronic diseases can greatly reduce the risk of death [71-73]. Therefore, daily health monitoring has become an important means to detect and control diseases, especially cardiovascular diseases [74,75]. However, at this stage, the number of medical institutions is limited and they can only provide services to a small number of people. Furthermore, most of the work can only be performed by trained personnel, resulting in considerable waiting times for medical treatment. For people who are busy with work, frequent and long-term visits to the hospital for check-ups are unrealistic. In view of these limitations, it would be valuable to investigate low-cost vital signs monitoring devices that can be used daily at home [76,77]. These research results will effectively reduce the medical burden and benefit the entire society.

FOSs have the advantages of immunity to EMI, lightweight, small size, high sensitivity, robust performance, and ability to withstand harsh environments. Different physical parameters, such as RI, temperature and strain, can modulate the light in special optical fibers through elastic or thermo-optical effects. To date, the use of special optical fibers as sensors to measure RI, temperature and strain has been widely used in civil engineering, environmental monitoring, biomedical engineering and other fields.

2.2 Seven-core fiber-based vital signs monitoring sensor

2.2.1 Overview

HR and RR are important indicators for evaluating health conditions and disease diagnosis [78]. Identifying and analyzing abnormal HR and RR can help users detect some diseases at an early stage, such as sleep apnea syndrome, premature beats, asthma, etc. [79,80]. It is worth noting that most chronic diseases are accompanied by breathing or heartbeat abnormalities. ECG is the most commonly used commercial medical device for accurate and stable monitoring of HR [81]. This method usually requires 3 or more electrodes attached to the body. A common method of detecting breathing is to detect changes in the subject's exhaled airflow and chest volume. This approach typically requires patients to wear masks during testing. Complex operating procedures and contact-based measurement methods make traditional HR and RR measurements unsuitable for long-term use.

In the past few years, various novel vital sign monitoring devices have been developed based on different principles to overcome the shortcomings of the above methods, such as Wi-Fi signal-based devices [82], Doppler radar-based devices [83], and motion microscopy-based devices [84]. These devices provide users with a more comfortable experience. However, the low stability and high cost of the systems limit the possibilities for home use. In the past few decades, FOSs have attracted widespread attention due to their unique advantages, including lightweight, immunity to EMI, low cost, etc. These excellent characteristics have inspired researchers to investigate optical fiber-based HR and RR monitoring systems. The recently developed FOSs can simultaneously serve as a sensing element to obtain information and as a medium to transmit signals [85-88].

The idea of optical fiber-based non-invasive vital sign monitoring technology was proposed and attempted a few decades ago [89,90]. The rise and fall of the chest with breathing causes changes in the pressure exerted on the FOS. The body produces tiny vibrations as blood is pumped during each heartbeat. Fiber optic interferometers are very sensitive to these smile perturbations, and the collected data can be filtered to extract HR and RR. Since the optical signal is limited to the optical fiber and has no contact with the human body, the user's safety and comfort are significantly improved. Thanks to the advantages of interferometers, many scholars have proposed various interference-based FOS for vital sign measurement. In 2012, Sprager et al. reported an MI-based HR and RR monitoring FOS placed within a mattress [91]. In 2014, Yang et al. proposed on a textile FOS for HR and RR measurement based on fiber microbending effects [92]. In 2018, Chen et al. developed a novel few-mode fiber-based FOS for HR and RR monitoring [93]. The proposed FOS structure can significantly reduce the complexity of sensor production, since it has only one optical fiber. One year later, Tan et al. proposed an interferometer based on strongly coupled TCF for non-invasive HR and RR monitoring [80]. However, the performance of above-mentioned FMF- and TCF-based interferometers is highly dependent on the non-repeatable fusing splicing process. They are not suitable for large-scale commercial production. Compared with the above-mentioned fibers, strongly coupled SCF has stable and balanced mode excitation and distribution. The SCF-based interferometer has high repeatability and is suitable for commercial production. SCF has been investigated and applied in different applications, such as temperature, curvature, strain, vibration, displacement, and RI [87, 88, 94-101]. It is expected to be a better choice for vital signs monitoring.

A low-cost, stable, and repeatable FOS based on strongly coupled SCF is proposed for non-contact vital sign measurement. Based on interference principle, an optical fiber fusion splicer is used to sandwich the SCF between two sections of SMF. The SCF-based FOS is encapsulated in a cushion to achieve the monitoring of RR and HR. Comparing the BCG signal obtained by FOS with the reference ECG signals obtained by the AD8232 module simultaneously, the usability of SCF-based FOS in the field of vital signs monitoring was confirmed.

2.2.2 Principle and simulation

Fig. 2.1(a) shows the effective RI of the two supermodes of the proposed sensor, and Fig. 2.1(b) shows FOS structure. A strongly coupled SCF is fusing splicing between two sections of SMF. Sensor fabrication requires only standard fiber cutting and splicing procedures, ensuring repeatability and durability. The SCF used by the sensor is homemade. First, the VAD method was used to prepare Ge-doped silica rods, and seven silica rods with smaller diameters were pulled out. Then, seven silica hollow tubes were prepared, the diameter of these hollow tubes was slightly larger than the silica rods. After pickling and drying, seven silica rods are inserted into the silica hollow tube and stacked in a hexagonal shape. Finally, a jacked tube is added to the silica hollow tube in which the quartz rod is inserted to create a preform. SCF can be drawn in an optical fiber drawing tower of our laboratory at approximately 1900°C. Fig. 2.1(c) demonstrates an SEM image of the proposed SCF. The homemade SCF consists of seven cores with a distance of 11 μm and a diameter of 8.2 μm, and a pure silica cladding with a diameter of 125 μm. The RI difference between the core and the cladding is 0.0049. Since the center core diameter of the SCF is the same as that of the SMF core and the diameters of the two fiber claddings are the same, the insertion loss caused by mode mismatch and the risk of breakage caused by bending at the splicing point are reduced.

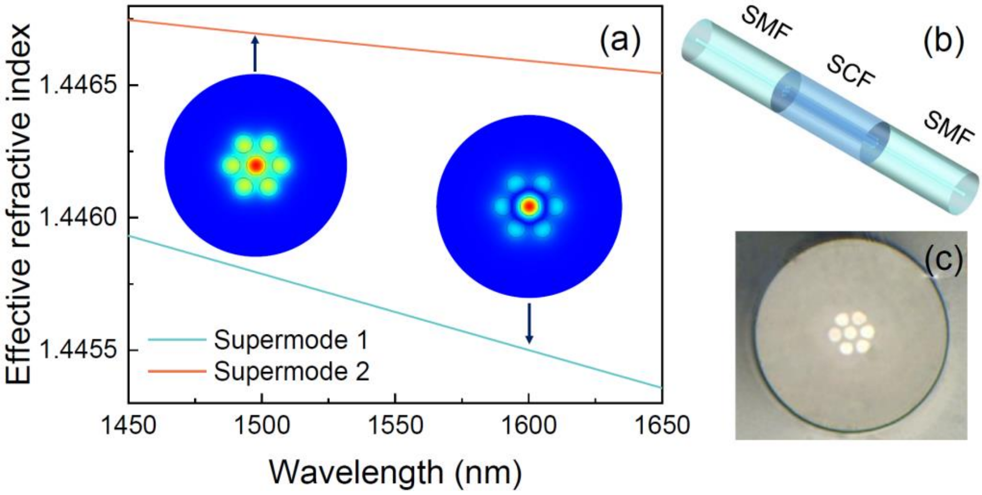

Fig. 2.1 (a) The effective RI of two supermodes and mode profiles. (b) The structure of SCF-based FOS. (c) SEM image of SCF cross-section.

In the practical application of the proposed system based on self-made strong coupling SCF, the optical signal is injected from the SMF, and multiple supermodes are excited when passing through the first splicing point. These modes couple into another segment of SMF as they propagate along the SCF to the second splicing point. Generally, multiple modes of transmission can be supported in the SCF. However, because of the geometric symmetry of proposed SCF and the excitation of fundamental mode by SMF, only two modes transmission can be supported in the SCF of the proposed sensor [102]. In the second SMF, the two modes of light will interfere and form interference fringes. Since the effective RI of the two modes are different, the intensity of the interference light can be expressed as:

$$I = I_1 + I_2 + 2\sqrt{I_1 I_2}\cos\frac{2\pi L(n_1 - n_2)}{\lambda}, \tag{2.1}$$

where I_1 and I_2 are the intensities of two supermodes that interfere, L is the length of the SCF, n_1 and n_2 are the effective RIs of two modes, and λ_m is wavelength of the input light. Therefore, the wavelength of m-order interference valley can be expressed as:

$$\lambda_m = \frac{2(n_1 - n_2)L}{2m+1}. \tag{2.2}$$

The FSR of the SCF can be expressed as:

$$\Lambda = \frac{\lambda^2}{(n_1 - n_2)L}. \tag{2.3}$$

The photoelastic effect will cause the effective RI of the two supermodes to change when the SCF is bent, causing a shift in the wavelength of the interference valley of the transmission spectrum. The shift of the interference valley will cause the interference light intensity of the second SMF to change. The bending curvature of MZI can be obtained by monitoring changes in interference light intensity.

Full vector FEM simulations were performed using COMSOL Multiphysics to investigate the theoretical basis of the proposed SCF-based vital signs sensor. As mentioned above, although SCF can theoretically support multiple modes of transmission, only the two most powerful modes make a major contribution to interference at the second welding point. Fig. 2.1(a) shows the simulation results of COMSOL Multiphysics. The effective RI of both supermodes decreases with the increase of operating wavelength, and the change rate of Supermode-1 is higher than that of supermode-2. The inset shows the profiles of the two modes at a wavelength of 1550nm.

Substituting RI into Eq. 2.1, the normalized transmission spectrum of SCF-based FOS can be obtained. Because the intensity of the two modes only determines the fringe contrast and not the valley wavelength, the intensity values of the two modes are set to $I_1 = I_2$. Fig. 2.2 illustrates the interference spectrum results of SCFs with three lengths: 3.6 cm, 4.8 cm, and 100 cm. Substituting the effective RI of the two modes into Eq. 2.3, it can be found that the FSR corresponding to the three lengths of SCF are 37.5 nm, 28.2 nm, and 1.42 nm.

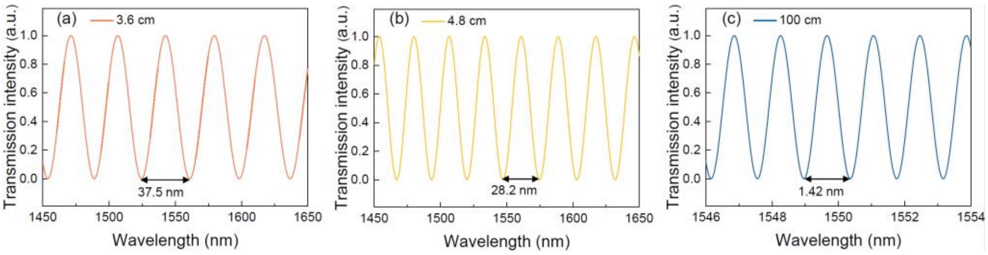

Fig. 2.2. The interference spectrum results of SCFs with three different lengths: (a) 3.6 cm, (b) 4.8 cm, and (c) 100 cm.

As shown in Fig. 2.3(a), when SCF bends, the RI of the two modes is obtained by the method in [103]. By applying a conformal transformation with an RI profile, straight fibers can be used as an equivalent substitution for curved fibers:

$$n_b(x, y) = n(x, y) \cdot e^{x/R}, \quad (2.4)$$

where R is the bend radius of SCF and $n(x, y)$ is the RI profile of a straight fiber.

Let θ represent the bending angle of proposed SCF relative to the x-axis, and set the incident light wavelength to 1550 nm. Fig. 2.3(c-j) shows the mode profiles of two supermodes of SCF bent along two directions of $\theta = 0°$ and $\theta = 90°$ with the curvatures of 5 m^{-1} and 10 m^{-1}. The main energy of supermode-1 is confined to the center core of the SCF. As curvature increases, a small portion of the intensity will be transferred to the inner core. However, for supermode-2, more energy leaks from the center core and couples into the outer cores when SCF bends.

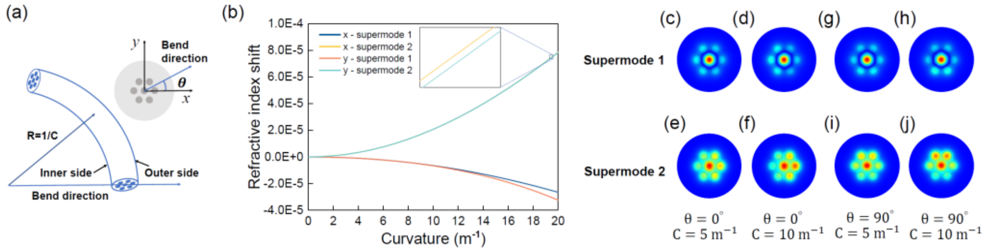

Fig. 2.3. (a) The bending simulation principle. (b) Calculated effective RI shifts of the two modes as a function of curvature for SCF bent along two orthogonal directions. (c-j) The mode profiles of two supermodes with different bending curvatures.

The RI as a function of curvature is shown in Fig. 2.3(b). As the curvature of SCF increases along the x and y directions, the RI of supermode-1 decreases, while the RI of supermode-2 increases. The result matches the previous description of the mode distribution, that is, the energy of the two supermodes is coupled to the inner core and the outer core respectively. Moreover, the RI variation curves of supermode-2 bending along the x-axis and y-axis overlap well, which means that the bending direction has little effect on supermode-2. However, the RI of supermode-1 depends on the bending direction. As the curvature increases, the difference in the RI curves of supermode-1 curved along the x and y directions becomes larger and larger.

The interference spectrum of a 4.8 cm SCF under different bending curvatures along the two directions is shown in Fig. 2.4 (a) and (b). As curvature increases, the entire transmission spectrum is blue-shifted. This is because the rate of change of RI becomes larger during this process. The bending sensitivity, represented by the ratio of wavelength shift to curvature, also increases. Fig. 2.4(c) illustrates wavelength shift as a function of bend radius. Two curves match very well when the curvature is less than 14 m^{-1}, which means that the spectral shifts caused by the slight bending of the SCF in x or y direction are very close. In vital sign monitoring applications, since the SCF bends caused by heartbeat and breath are very small, the effective RI changes of the two modes can be regarded as isotropic.

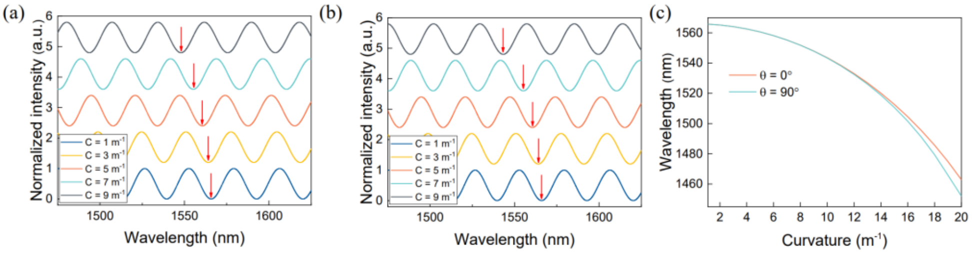

Fig. 2.4. The spectra changes of SCF when bending along (a) $\theta = 0°$ and (b) $\theta = 90°$. (c) The wavelength shift of the valley around 1550 nm as a function of curvature for SCF bent along $\theta = 0°$ and $\theta = 90°$.

Next, the bending response sensitivity of SCFs with lengths of 50 mm, 100mm, 150 mm and 200 mm was simulated, as shown in Fig. 2.5. Fig. 2.5(a) shows the wavelength as a function of the curvature, and the relationship between the wavelength shift and the curvature here is close to parabolic. The results from 4 m^{-1} to 13 m^{-1} are selected from Fig. 2.5(a) to quantify the bending sensitivity, as shown in Fig. 2.5(b). Within this relatively narrow range, this curve can be approximated by a linear fitting instead of a quadratic fitting, and the slope achieved from linear fitting results is the curvature response sensitivity. Linear fitting resulted in a curvature sensitivity of 4.56 nm/m^{-1}. Fig. 2.5(c) demonstrates the results of the analysis of four sensors with SCF lengths from 50 mm to 200 mm.

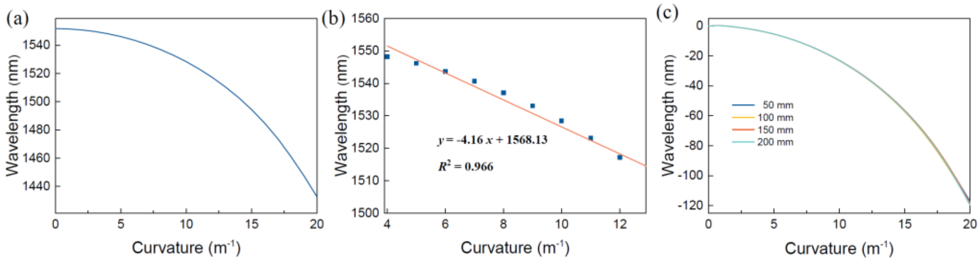

Fig. 2.5. The bending response sensitivity an SCF with 50 mm: the curvature range is from (a) 0 m^{-1} to 20 m^{-1} and (b) 4 m^{-1} to 13 m^{-1}. (c) Wavelength shifts of one valley as a function of curvature for 50 mm, 100 mm, 150 mm and 200 mm SCF.

2.2.3 Vital signs monitoring

After the investigation of the transmission characteristics of SCF and the bending response of SCF-based sensor, vital signs monitoring experiments were performed using the proposed system shown in Fig. 2.3(a). Based on our previous experimental results, the sensor is fabricated from SCF with a length of 1m to avoid exceeding the measurement range due to the subject's unavoidable body movements. The SCF for sensing and the SMF for transmitting light signals are fixed to the mattress with glue. During the test, the subject lay flat on the mattress with the chest above the FOS to obtain BCG signals in the front-to-back direction. The input light from TL is emitted into the vital signs monitoring system by a SMF and received by a PD after passing through FOS. The input light wavelength of TL is fixed at 1549.88 nm. The light in FOS is modulated by the tiny vibrations of the body caused by the heartbeat and the rise and fall of the chest caused by breathing. Recordings were performed using a MATLAB program via a National Instruments DAQ card (USB6210) with a sampling rate of 5000 Hz. The light intensity detected by PD changes with the spectral shift caused by heartbeat and breathing. The transmission spectrum of FOS is shown in Fig. 2.6(b), and its FSR is consistent with the simulation result of 1m SCF of 1.42 nm (Fig. 2.2(c)). The reference HR can be calculated from PPG signals collected using a commercial finger-clip PPG device.

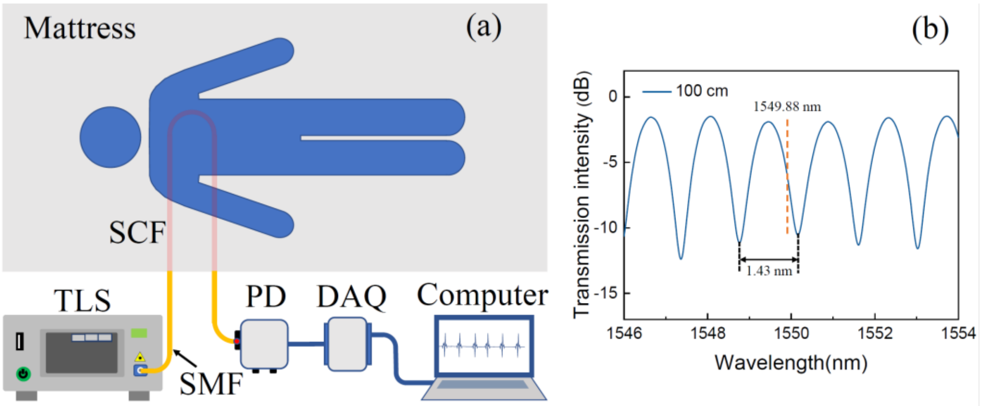

Fig. 2.6. (a) The experimental diagram. (b) The transmission spectrum of proposed FOS with 1m SCF.

Fig. 2.7(a) illustrates the FOS raw data collected in the resting state of the subject. Since the respiratory and heartbeat signals are signals of different frequencies, they can be obtained using an LPF or a BPF. Fig. 2.7(b) shows the spectral information obtained by FFT of the raw data. In particular, this experiment uses a BPF with a cut-off frequency of 0.05 Hz to 0.4 Hz to obtain the respiratory signal, and a BPF with a cut-off frequency of 0.8 Hz to 7 Hz to extract heartbeat signals.

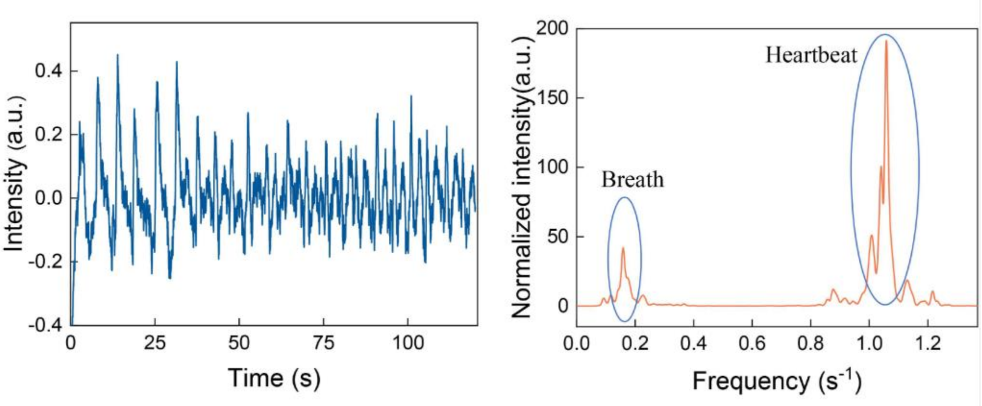

Fig. 2.7. (a) The raw data collected from proposed FOS. (b) The FFT result of the raw data processed with MATLAB.

Fig. 2.8 shows the 1-min RR and HR results obtained from the raw data. The respiratory signal has 14 peaks within 60 seconds, which is consistent with the number counted using an external recording instrument, as shown in Fig. 2.8(a). During the entire measurement process, the peak-to-peak interval of the respiratory signal fluctuated around 5 seconds, and the corresponding RR was 12 bpm. For heartbeat monitoring, the IBI of BCG obtained by our sensor is calculated by the J-J interval, while the reference IBI is calculated by the P-P interval of PPG, as shown in Fig. 2.8(b). The heart rate calculated based on BCG IBI is 72 bpm, which is consistent with the result calculated based on PPG IBI. Therefore, the SCF-based vital signs monitoring system can effectively and accurately achieve simultaneous measurement of HR and RR.

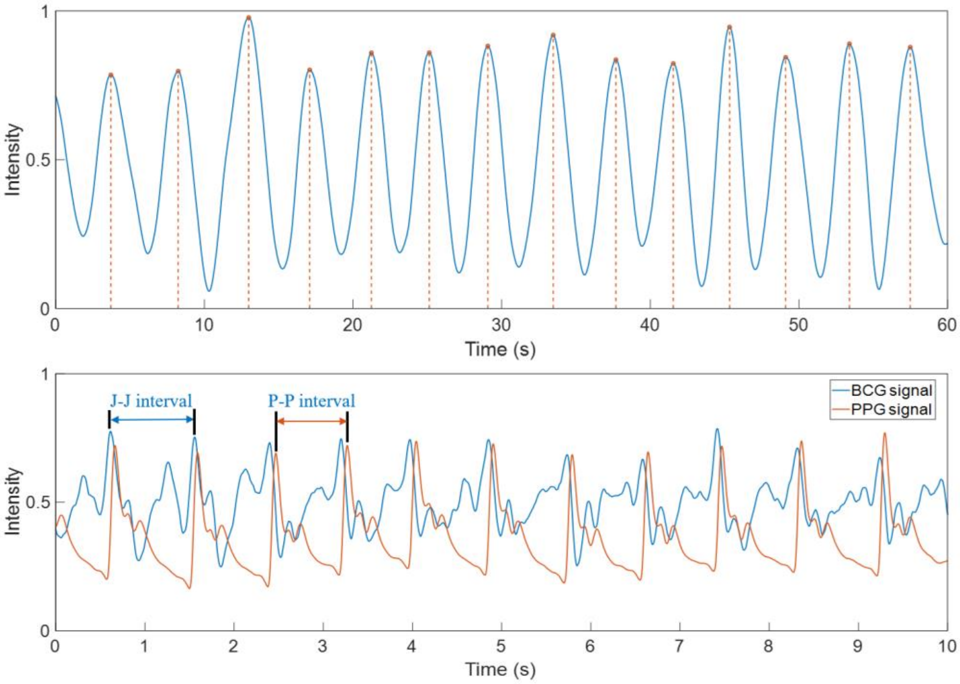

Fig. 2.8. The filtered results of respiration (top) and heartbeat (bottom).

Post-exercise HRV analysis is often used as a means to diagnose cardiovascular diseases [104]. The validity of HRV analysis based on the post-exercise BCG J-J interval has been demonstrated [105]. This work analyzed the changing trends of RR and HR after exercise calculated by the collected BCG and PPG signals. The subjects were asked to perform 20 burpees and then immediately lie on the mattress to collect data. Monitoring lasted approximately four minutes. To visualize the changes in RR and HR, Fig. 2.9 and Fig. 2.10 shows the 30-second RR and 10-second HR results, respectively. After the subject lay down, the peak-to-peak interval of the two signals showed a downward trend, which meant that RR and HR gradually returned to normal. At the end of the exercise, the RR reached 18.2 bpm and dropped to 14.0 bpm after 4 minutes. During this time, the

HR results decreased from 114 bpm to 106.9 bpm, which is consistent with the results calculated from the PPG signal.

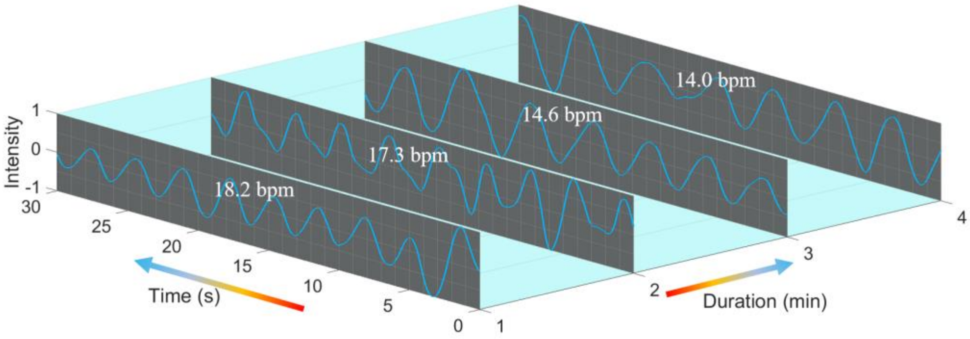

Fig. 2.9. RR results using SCF-based FOS system.

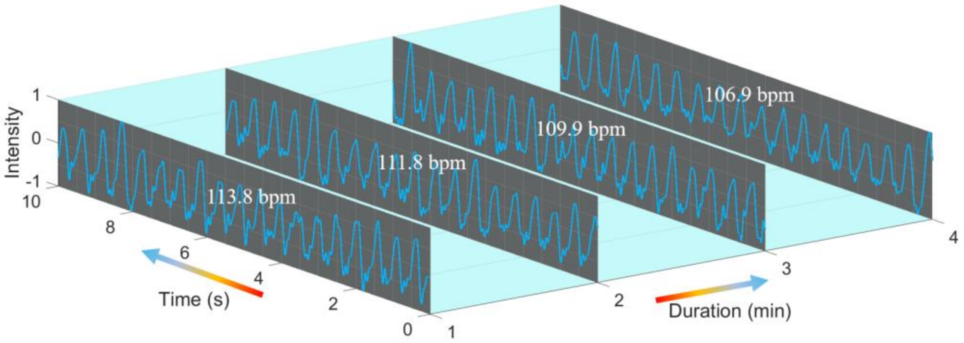

Fig. 2.10. HR results using SCF-based FOS system.

Experimental results demonstrate that our SCF-based vital sign detection system can simultaneously monitor HR and RR after exercise. In addition, our system has unique and superior performance compared to other FOS-based vital sign monitoring systems. First, some vital sign monitoring systems based on few-mode or multi-mode optical fibers take advantage of inter-mode interference between different modes, and their performance is affected by the length of sensing fiber. The length change may introduce more higher-order modes for interference, which gives the sensor an unstable interference spectrum. The inability to precisely control the length of sensing fiber makes this type of vital signs monitoring system less valuable in the commercial world. The SCF excited supermode used in this work can be guided with low loss, and the transmission spectrum can be accurately predicted. What's more, the FOS is fabricated simply by sandwiching the SCF between two SMFs using standard welding procedures. Small differences in SCF length only affect the FSR of the transmitted spectrum without changing the spectrum type. And compared with sensors based on weakly coupled multi-mode fiber offset splicing, this splicing method ensures that the FOS has better mechanical strength, better repeatability, and lower insertion loss. Therefore, we believe that SCF-based vital signs monitoring systems are very promising candidates in the health field.

2.3 Six hole fiber based vital signs monitoring sensor

2.3.1 Overview

In recent years, various electronic sensors based on different data acquisition methods have been proposed for HR monitoring, such as fingertip cardiotachometer, wrist cardiotachometer, and ECG instruments [106-108]. As for RR monitoring, the head-mounted respiratory monitor takes up the primary market [109]. However, all electronic sensors cannot be used in the high electromagnetic environment, such as magnetic resonance imaging equipment. Moreover, most electronic sensors are wearable, which is uncomfortable for humans.

BCG signals capture the ballistic force of the heart due to the sudden ejection of blood into the vessels with each heartbeat and can be measured non-invasively. Using non-invasive FOSs as the primary sensing element in a vital signs monitoring system is an ingenious way to solve electromagnetic interference and comfort problems. In addition, FOSs possess many unique advantages, such as compact size, lightweight, chemical corrosion resistance, and long-term stability. An increasing number of FOSs-based monitoring system proposed by researchers worldwide also proves the advantages above. In 2017, Presti et al. developed a smart textile based on 12 FBG arrays capable of monitoring RR and HR in both standing and supine postures [110]. In 2019, Tan et al. proposed an interferometer based on strongly coupled TCF for non-invasive RR and HR monitoring [80]. In 2020, Xu et al. proposed an all-fiber vital signs monitoring system with long-mode interference in MMF and applied it to achieve non-wearable vital signs monitoring [111]. However, FBG-based sensors are too expensive for widespread use. The TCF and MMF-based sensors are affected by external temperature variations which will cause signal fading problem.

In this section, a temperature-insensitive FOS is proposed for non-invasive vital signs monitoring. The core sensing element is an SI built by an optical coupler and a homemade SH-HiBiF. The SH-HiBiF is a type of temperature-insensitive fiber for its raw material is pure fused silica without doping any other particles. Due to the low temperature sensitivity of the proposed sensor, there is no signal fading problem caused by temperature changes in traditional interferometers. The proposed system is simple in structure and can achieve quadrature operation without complicated demodulation methods, like 3×3 coupler and phase generation carrier, commonly used in interferometers. The interference spectrum of the SI generated by a broad-spectrum light source can shift linearly with the lateral stress variation because of the stress-induced birefringence effect in this fiber. If the single-wavelength light around the Q points (the points on the interference spectrum with the highest slope) is injected into the SI, the heartbeat and respiratory signal can modulate the output light intensity. Then, the PD can be used to convert the heartbeat- and respiration-modulated optical signals into electrical signals, which are collected by the multi-modalities signal acquisition board together with the reference ECG signal. All signals are transmitted to a computer through a router. The HR and RR of the subjects with premature beats can be obtained directly through the spectrum analysis of the raw signal. The J peaks of BCG signals can be quickly identified using template matching and then used to recognize abnormal heartbeats. The average accuracy of normal and premature beats recognition based on a commonly used classification algorithm, SVM, is 98.4% and 97.9%.

2.3.2 Sagnac interferometer and experiment system

The core part of the proposed system is a temperature-insensitive optical fiber SI, built up by a 3 dB coupler and a section of homemade SH-HiBiF. Because of the circular asymmetric structure in the fiber, the time-domain spectroscopy of the SI will shift linearly as the lateral stress change.

Because of the circular asymmetric structure of the suspended core part, a stress-induced birefringent effect is introduced into this fiber. The cross-section of the fiber used for building up the SI is shown in Fig. 2.11(a).

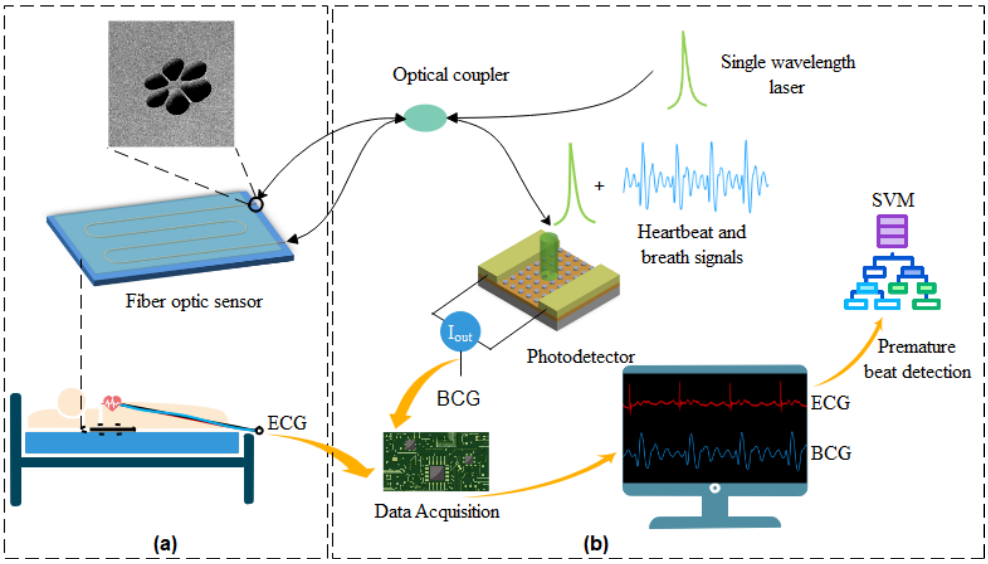

Fig. 2.11. System working principle. (a) vital signs monitoring sensors setup (FOS-based BCG sensor and commercial AD8232-based ECG sensor), (b) optical signal generation and signal processing system.

Fig. 2.11 demonstrates the working principle diagram of the vital signs monitoring system. Subjects with premature beats lie on the bed, and the FOS is placed under the chest to collect BCG signals, as shown in Fig. 2.11(a). In addition, three electrodes are attached to the chest and abdomen, and the commercial equipment AD8232 is used to collect synchronized ECG signals, which is convenient for experts to select BCG J peaks manually. Fig. 2.11(b) shows the laser source of FOS and the signal processing system. Signal light from a tunable laser is injected into the FOS, and the output signal is received by a PD. All data are collected by a multi-modal signal acquisition board with a sampling frequency of 1000 Hz, and then transmitted to a computer through a router. ECG and BCG waveform signals are displayed on the display device in real-time. Abnormal heartbeats (premature beats) can be identified with SVM after template matching.

2.3.3 Data processing and results

Fig. 2.12 shows the data processing block diagram of the proposed vital signs monitoring system. HR and RR can be directly obtained by MATLAB FFT function with the raw BCG signal and displayed on a monitor in real-time. The template matching method can be used to find out the J peak of BCG quickly and accurately, and SVM can be used to identify abnormal heartbeats.

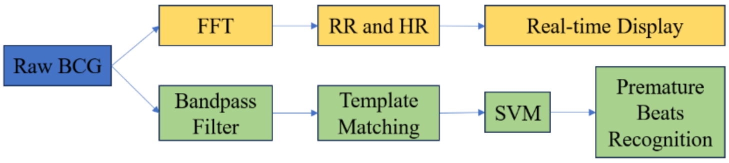

Fig. 2.12. The data processing block diagram of the proposed vital signs monitoring system.

Fig. 2.13 (a) shows the raw data collected by the subjects with premature beats at rest. Since the respiration and heartbeat signals have different frequencies, two BPFs can be used to extract them. The frequency distribution of the original BCG signal after FFT processing is shown in Fig. 2.13(b). According to the characteristics of the BCG signal, the respiration signals can be obtained using a BPF with a specified cutoff frequency of 0.1 Hz and 0.5 Hz, and the heartbeat signals can be obtained using a BPF with a specified cutoff frequency of 0.8 Hz and 25 Hz.

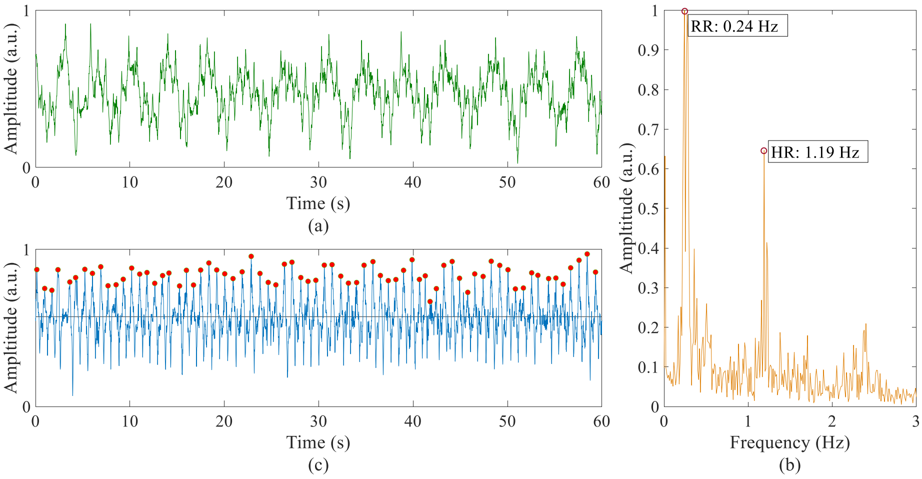

Fig. 2.13. (a) The raw data collected using SH-HiBiF-based vital signs monitoring system, (b) the frequency spectrum raw data, and (c) J peaks of BCG selected by template matching and expert.

For premature beats recognition, a simple and effortless template matching method is used to preprocess the raw BCG signal, which can extract the J-peak without ECG synchronization. The extraction method is based on template matching evaluated using a correlation function during a locally moving window. Template matching is performed with a local moving window function that generates correlation coefficients between the template constructed during the previous modeling process and the BCG signal. First, a BPF with a cutoff frequency of 0.5−20 Hz is used to remove the respiration signal from the original signal. The templates are selected by experts to represent the general shape of the BCG signal based on filtered BCG signals. The I-J-K complex of BCG corresponds to ventricular systole and the Q-R-S complex of ECG. Then, the correlation function computes the accuracy of the template versus the BCG signal using a local moving window. Fig. 2.13(c) shows that the J-peak detected by template matching (indicated by red dots) is entirely consistent with the expert analysis (indicated by green circles).

Since a premature beat is a heartbeat that occurs earlier than expected, it can be identified by the J-J intervals. After extracting the J peaks of BCG, a sudden shortened J-J interval is marked as a premature beat (judged by experts). The results can be expressed as:

$$\left(\vec{x}_1, y_1\right), \dots, \left(\vec{x}_n, y_n\right)$$

where x_i are the J-J intervals and y_i are either 1 (normal) or -1 (abnormal) indicating the class to which belongs. 75% of the data is used to train the SVM model, and then the remaining 25% works as a test set. The premature beats recognition result is shown in Fig. 2.14. The accuracy of premature beats recognition is 97.9%, and normal beats recognition is 98.4%.

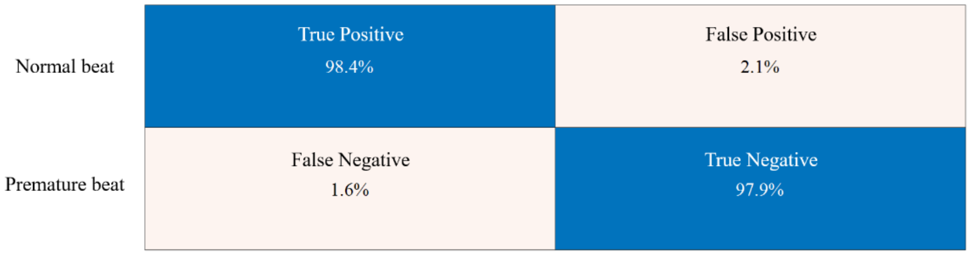

Normal beat	True Positive 98.4%	False Positive 2.1%
Premature beat	False Negative 1.6%	True Negative 97.9%

Fig. 2.14. Premature beats recognition results using SVM.

2.4 Summary

In this chapter, a novel inline MZI sensor based on homemade SCF supermodular interference is proposed and fabricated for non-contact vital signs monitoring. It is created by splicing a segment of SCF between two segments of SMF through a simple splicing procedure. Encapsulating sensing optical fibers under mattresses enables long-term monitoring of vital signs signals. Through filtering and FFT algorithms, accurate RR and HR can be obtained. Lower cost, simpler process and better accuracy make SCF-based vital sign detection systems highly competitive in the home healthcare field.

In addition, a non-invasive vital signs monitoring system based on optical fiber SI is proposed, which works well. The core part of this system is an optical fiber SI, built up by a 3 dB coupler and a section of homemade SH-HiBiF. Since the optical fiber material of the sensing part is pure fused silica, which is insensitive to temperature, the system does not need to apply any demodulation scheme to solve the signal fading problem. Moreover, the proposed system can be used to diagnose premature beats with 97.9% accuracy even without attaching the electrodes to the human body, which is more comfortable for the patients. Performed experiments demonstrate the system’s feasibility in further research in the biomedical field.

Chapter 3

Single-mode fiber-based robust vital signs monitoring system

3.1 Introduction

In recent decades, a lot of vital signs monitoring devices have been developed and widely used in daily life. The most commonly used cardiac monitoring device in the current healthcare system is the ECG device [112]. By attaching electrodes to the chest, abdomen, and limbs, the heart's electrical signals can be collected. In addition to ECG, PPG is a common heartbeat measurement method, and the pulse signal can be obtained by clipping a pulse oximeter on the finger [113]. The principle of PPG devices is to collect cardiac information through changes in transmitted or reflected light intensity on the skin. Spirometry, capnometry, and impedance pneumography are commonly used methods for respiratory monitoring [114]. However, traditional medical devices have some limitations that need to be addressed. During the ECG measurement process, several patches need to be attached to the body, which can cause discomfort to the user. PPG is also a contact measurement method. Clamping the finger with the device for a long time will cause poor blood flow. Spirometry interferes with the natural respiration of users, making continuous respiration monitoring difficult. As a contact measurement method, capnography also causes discomfort to the users. Impedance respirography requires the use of special equipment for analysis, resulting in high costs. Therefore, these heartbeat and respiration monitoring devices are not suitable for daily use at home. BCG reflects information about the mechanical vibration of the heart without attaching any patches to the body. At the same time, respiratory information can also be obtained from the BCG raw data. Taking advantage of the difference in heartbeat and respiratory rates, simultaneous monitoring of HR and RR can be achieved through a single monitoring system.

3.2 Sensor structure

Fig. 3.1 shows the system setup. The FOS consists of a 1×2 coupler and a 3×3 coupler. The light is injected into the 1×2 coupler of the MZI by the DFB laser and interferes at the 3×3 coupler after passing through the sensing arm and the reference arm. Asymmetric configurations can improve the sensitivity of the sensor by creating a larger phase difference between the interfering light waves. This makes it easier to detect small changes in the measured parameter. The interference light is divided into three signals and transmitted to the PD. The FOS is placed under the cushion to measure the BCG signal, and 3 electrodes are attached to the chest and abdomen to obtain 3-lead ECG signals. The optical signals output by FOS and ECG signal are collected by a multi-modalities signal acquisition board and transmitted to a computer through a router. The multi-modalities signal acquisition board contains a 1550 nm pigtailed DFB laser with a spectral width of 0.1 nm used as the light source in the FOS system, 3 PDs used to receive the optical signal output by the FOS, a MCU used for demodulation 3 channels optical signals, an AD 8232 module used for processing ECG signals, and a Wi-Fi module used for transmitting ECG and BCG signals. All the collected data can be viewed on the computer with processed waveforms and calculated HR. Since the paced respiration will significantly change the amplitude of HRV, the system acquired all four channels (three channels of BCG signals and one channel of ECG signals) at a sampling frequency of 1000 Hz to obtain more accurate data.

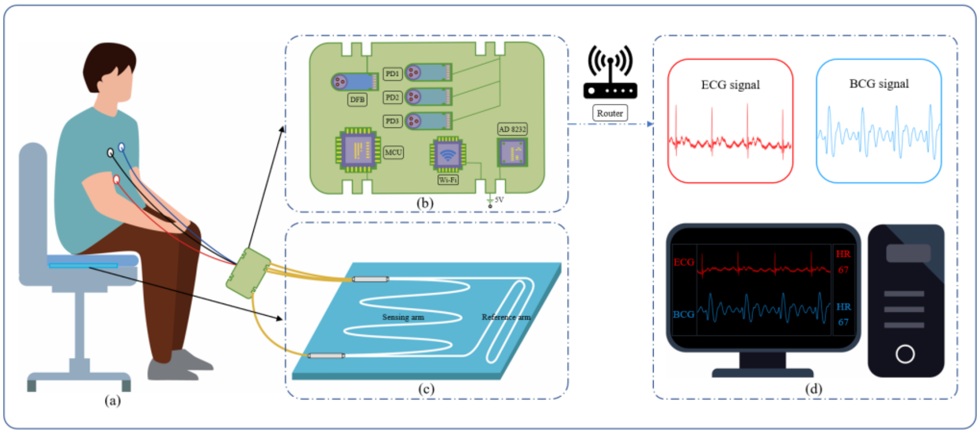

Fig. 3.1. (a) Experiment setup (FOS placed under a mattress, 3 electrodes attached to the chest and abdomen, a multi-modalities signal acquisition board for collecting BCG and ECG signals); (b) multi-modalities signal acquisition board schematic (containing 1 DFB laser, 3 PDs, 1 MCU, 1 Wi-Fi module, and 1 ECG module AD 8232); (c) interferometric FOS structure (containing a 1×2 coupler and a 3×3 coupler); (d) ECG and BCG HR signal real-time display.

A 1550 nm DFB laser is used as the light source in the FOS system. Since the FOS is based on the principle of interference, the changes of the external environment may cause the random phase drift of the sensor, which will make the working point of the fiber optic interferometer deviate from the center of the linear region. The random drift of the working point can seriously affect the working state of the interferometer. Thus, a 3×3 demodulation method was applied for analyzing the BCG signal, that is, using a 3×3 coupler to divide the interference light into three beams with a phase difference of 120° [115]. The light emitted from the DFB laser is transmitted into the reference and sensing fibers through a 1×2 coupler. Then the beams of light transmitting in the reference and sensing arms will interfere at the 3×3 coupler. The output light intensity of the interferometer can be calculated using the equation below:

$$I_k = D + I_0 \cos[\varphi(t) - (k-1)(2\pi/3)], \tag{3.1}$$

where $\varphi(t)$ is the phase difference of light signals, D is the average value of output light intensity, I_0 is the peak intensity of interference fringes, k is the number of the output light path, $k = 1, 2, 3$.

In practical application, φ(t) includes phase changes caused by the measured information and the environment variation which can be expressed as:

$$\varphi(t) = \phi(t) + \psi(t), \tag{3.2}$$

where $\varphi(t)$ represents the signal to be measured, and $\psi(t)$ is the phase difference caused by environmental changes.

The sensing arm and reference arm of FOS were fixed on the acrylic board with polypropylene/polyethylene glue, and then encapsulated with epoxy resin AB glue to ensure long-time stability of the sensor system. The transmission spectrum of the interferometric FOS can be observed by an optical spectrum analyzer (YOKOGAWA AQ6370D), as shown in Fig. 3.2.

Four interference dips can be observed in the spectrum at wavelengths 1549.4, 1549.72, 1550.03, and 1550.34 nm, respectively. All these dips can be used for BCG sensing.

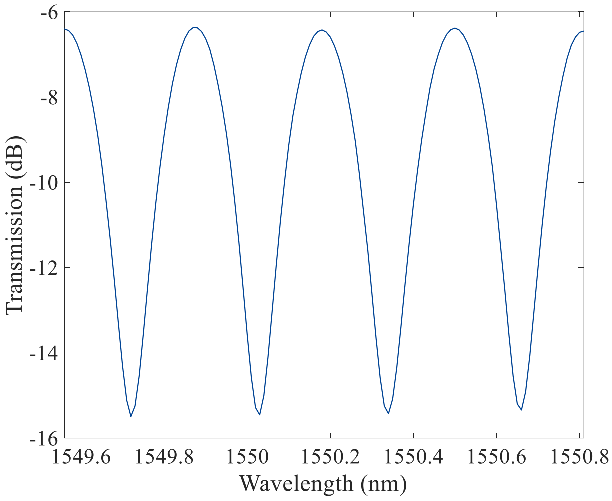

Fig. 3.2. Transmission spectrum of the interferometric FOS.

3.3 The 3×3 coupler demodulation method

According to Eq. (3.1), the three optical intensity signals can be demodulated by the 3×3 coupler demodulation scheme shown in Fig. 3.3.

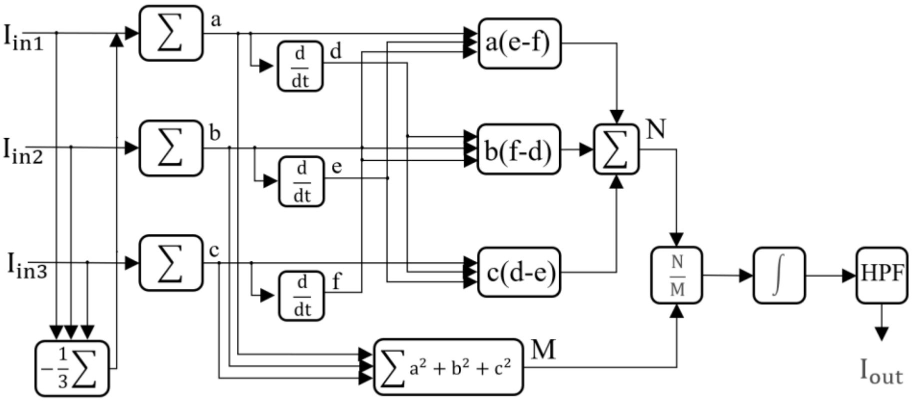

Fig. 3.3. Optical fiber 3×3 coupler demodulation scheme.

After differentiation and cross-multiplication, the demodulated signal is:

$$N = a(e - f) + b(f - d) + c(d - e) = \frac{3\sqrt{3}}{2} I_0^2 \varphi'(t). \qquad (3.3)$$

In the actual environment, fluctuations of the light intensity and changes of the polarization state will influence the value of I_0. In order to eliminate the influence factors, the following mathematical treatment is carried out.

First, square the three input signals to obtain:

$$M = a^2 + b^2 + c^2 = \frac{3I_0^2}{2}. \qquad (3.4)$$

Then divide N by M and eliminate I_0^2 to get:

$$P = \frac{N}{M} = \sqrt{3}\varphi'(t). \qquad (3.5)$$

After integral operation, the output is shown as:

$$\sqrt{3}\varphi(t) = \sqrt{3}\phi(t) + \psi(t). \qquad (3.6)$$

Usually, $\psi(t)$ is regarded as a slow change quantity, which can be filtered out through an HPF. I_{out} is the output signal of the 3×3 demodulation scheme, which is known as the BCG signal transmitted to the PC.

3.4 ECG and BCG data processing

HR is measured by the number of contractions of the heart per minute. The results of this experiment are calculated from the number of R peaks or J peaks in a minute. IBI is a scientific term used in reference to the time interval between individual beats. It is calculated from the time interval between two adjacent R or J peaks. The R peak corresponds to the peak of each QRS complex of the ECG, and the J peak corresponds to the peak of each IJK complex of the BCG. The R peaks of the ECG signal are detected by the "findpeaks" function of MATLAB. The reference IBI is calculated from the RR interval of the ECG. Since motion artifacts in the BCG signal can lead to power increase in all frequency bands which will significantly affect time and frequency domain results, we detect J peaks of the BCG signal by previous algorithm [116].

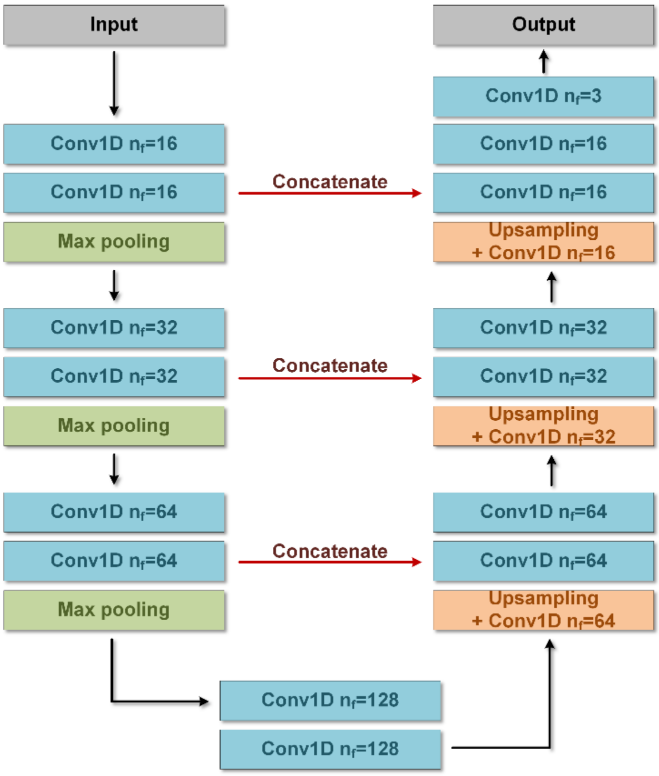

Fig. 3.4. The architecture of modified U-net.

This end-to-end algorithm is based on a modified U-net, and it can detect the position of IJK complex and body movement in the BCG signal. The architecture of the modified U-net is shown in Fig. 3.4, in which three contracting and expansive stages are included. n_f is the number of filters in 1-D convolution layer. The left part is the contracting path. Each stage consists of repeated two 15×1 1-D convolutional layers with ReLU activation function followed by a 2×1 max pooling layer with stride 2 to halve the size of feature maps. n_f in the convolutional layer doubles at each downsampling stage. The right part is the expansive path, and at each stage, an upsampling layer followed by a 2×1 convolutional layer is used to double the size of the feature map and halve the number of feature channels. The feature map in the corresponding contracting stage is directly duplicated and combined with the upsampled feature map in the expansive path. The combined feature map is followed by two 15×1 1-D convolutional layers with ReLU, and the filter number of the convolutional layer is halved at each upsampling stage. Finally, a convolutional layer with SoftMax activation functionis used in the output layer to predict the class of each sampling point, including IJK complex, body movement signal and background (non IJK complex). The kernel size and filter number of the function are 1×1 and 3. In this way, the motion artifacts can be removed and then accurate IJK complexes are obtained.

3.5 Results and discussion

The comparison between the demodulated BCG signal and the 3 channels of the original BCG signal is shown in Fig. 3.5. The top three pictures are three BCG output signals, and the bottom picture is the BCG signal after demodulation. Obviously, all three output signals have signal fading problem in a certain period of time. After demodulation, this problem is solved well.

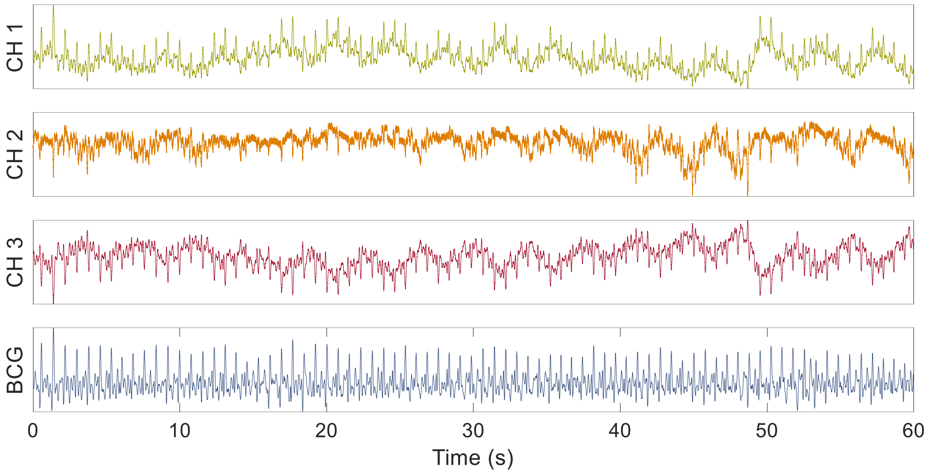

Fig. 3.5. Comparison between original and demodulation signals.

The R peaks of the ECG signal are detected by the “findpeaks” function of MATLAB. The reference IBI is calculated from the RR interval of the ECG. The BCG signals are demodulated using the above scheme and then filtered using a BPF with a lower cut-off frequency of 1.2 Hz and a higher frequency of 35 Hz [117]. This BPF can filter out breathing signal and get more details about the high frequency part of the BCG (i.e., J peak). The J peak of BCG is detected by the same function. Fig. 3.6 shows the 1-minute results for BCG and ECG. The FOS-based BCG-derived IBI shows high correlations with ECG-derived IBI, with a correlation coefficient of 0.9971.

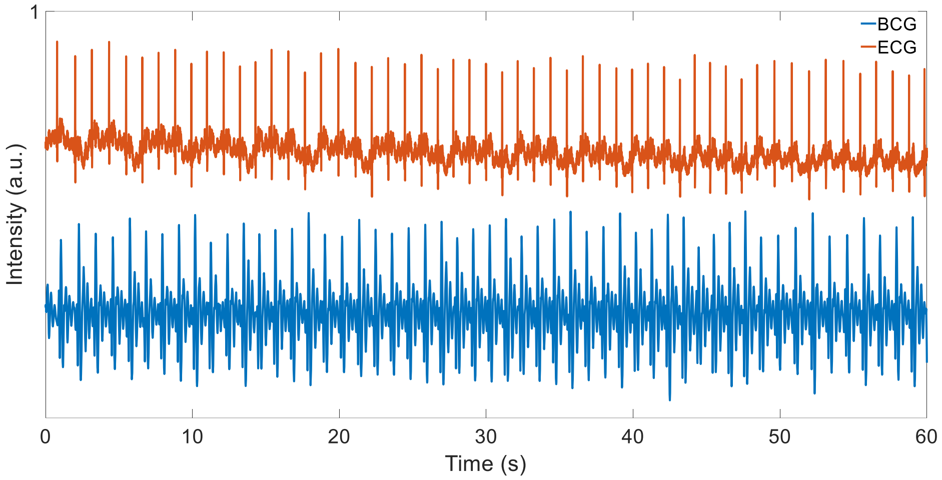

Fig. 3.6. 60-second BCG and ECG signal.

3.6 Summary

In this chapter, a low-cost FOS-based system is proposed for the long-term stable measurement of BCG, which can be used to collect accurate BCG signal. The core part of the system is a single-mode fiber-based MZI, which consists of a 1×2 coupler and a 3×3 coupler. Due to the asymmetric structure of the two MZI arms, the interference spectrum will be observed, which will move linearly with the change of the transverse stress. The incident light is emitted from a low-cost DFB laser and coupled into the MZI sensor. The vibrations induced by human respiration and heartbeat will result in the variation of light phase in MZI, and further give rise to the change of interfering light intensity which is detected by three PDs. The FOS-based BCG-derived IBI shows high correlations with ECG-derived IBI, with correlation coefficients of 0.9971. This system has the potential to become a preferred alternative for ECG in daily monitoring.

Chapter 4

Vital signs monitoring system applications

4.1 Introduction

The most pressing issue around the world today is to provide equitable and affordable health care for everyone. Equitable global healthcare means that everyone around the world has access to good healthcare services, which is a common challenge faced by developing countries [1]. The existing healthcare system is overburdened due to the increase in population and the lack of medical facilities, necessary infrastructure, qualified doctors and diagnostic equipment [2,3]. Researchers are working tirelessly to mitigate the effects of chronic and potentially fatal diseases such as heart disease, high BP, and asthma. in the past decade, with the maturity of smart wearable devices and the advancement of IoT and artificial intelligence technologies, continuous monitoring of vital signs such as HR, BP, heart sounds, RR and body temperature has become feasible in more and more application scenarios. Additionally, the daily monitoring of vital signs can aid in the diagnosis of viral infections like COVID-19.

As mentioned earlier, most traditional equipment requires contact measurement, which causes discomfort to patients. Contactless vital sign sensor technology can monitor a patient's vital signs without feeling. Continuous, non-contact vital sign monitoring reduces risk and increases alert for those requiring urgent attention. Camera-based vital signs monitoring products are already in use. The device detects severe early deterioration by continuously measuring HR and RR. An attractive option due to its ubiquity, high performance and cost-effectiveness. However, these camera-based vital sign monitoring devices are challenging in places where capturing images is prohibited. No one likes the feeling of being watched all the time, and this can cause discomfort for most people. The proposed fiber-based vital signs monitoring device can be seamlessly integrated into hotels, elderly care centers, homes, or outpatient care facilities, allowing truly sensorless measurements while protecting privacy.

Although continuous monitoring of dynamic vital signs can obtain a wealth of valuable health information, effective information extraction and monitoring device deployment remain challenging. The prediction of cardiovascular risk in different individuals and the assessment of sleep status are not yet satisfactory. Research on continuous monitoring of vital signs will play a significant role in the field of health care, because they can effectively help doctors make relevant treatment decisions. This chapter will show the application of optical fiber-based vital signs monitoring systems in different fields, protecting sleep monitoring, pulse monitoring and driver monitoring.

4.2 Sleep monitoring

4.2.1 Overview

With the aging of the global population, people are paying more and more attention to daily health monitoring. Health data that was only available in hospitals in the past can now be obtained by yourself at home. Cardiovascular diseases such as atrial fibrillation and hypertension require long-term monitoring during the prevention or recovery process. Therefore, the home vital signs monitoring system has attracted more and more people's attention. ECG is one of the widely used heart monitoring technologies in daily life, but it requires wired and multiple viscous Ag/AgCl electrodes to be attached to the body. PPG-based smart watches and smart bands are also used to provide daily HRV information. However, none of these technologies can reflect the mechanical vibration information of the heart. In the medical field, ICG can be used to measure the systolic and diastolic time interval of the heart, and has the advantages of non-invasive, safe, simple, continuous dynamic observation and so on. However, the equipment is bulky and expensive, and multiple electrodes need to be connected to the patient during the measurement process, which can cause discomfort, so it is not suitable for daily monitoring at home.

BCG is a non-invasive heart monitoring technology, which measures the tiny vibration caused by the blood pumped into the aorta during each heartbeat cycle [18]. This phenomenon was first discovered by Gordon in 1877. About 60 years later, Starr et al. conducted a lot of research on it. However, due to the limitations of sensor technology and measurement resolution, the development of BCG is very slow compared to ECG, and the research related to BCG almost disappeared in the late 20th century. In the past two decades, thanks to the development of sensor technology, academia has once again set off an upsurge in BCG research, and principle-based measurement equipment has appeared one after another [36,43,54,118,119]. Compared with the BCG system based on electrical sensors and thin film sensors, the BCG system based on interferometric FOS has higher sensitivity, lower cost, and is more suitable for home use.

Clinical studies have shown that sleep discontinuity caused by waking up at night increases the risk of cardiovascular disease, impairs immune function, and leads to obesity, diabetes, and cognitive dysfunction [120,121]. Therefore, it is very important to monitor the sleep state at night. The gold standard for sleep monitoring is PSG, but PSG equipment is complicated and expensive to use, and multiple wired sensors are installed on the face, head and limbs, which is extremely uncomfortable. Therefore, the BCG system is a better choice for continuous sleep and cardiovascular monitoring at home.

4.2.2 Methods

Fig. 4.1 shows the overall system setup and the FOS structure based on a 3×3 coupler. The heartbeat signal is collected by ECG equipment (AD 8232) and BCG equipment (FOS) at the same time. During sleep, 3 Ag/AgCl patches were attached to the subject’s chest and right abdomen to collect ECG signals, as shown in the red part of Fig. 4.1 (a). As shown in the green part of Fig. 4.1 (a), an optical fiber-based sensor is placed under the mattress to collect BCG signals. Fig. 4.1 (b) is a fiber optic sensor structure based on a 3×3 coupler, which can solve the signal fading problem. The components of the BCG and ECG sensors are packaged on the same circuit board and connected to the data acquisition card. All data is transmitted to the computer for processing through the USB data cable. In the optical fiber-based BCG sensor, the light from the 1550 nm distributed feedback laser is injected into the reference fiber and the sensing fiber through a 1×2 coupler. Then, the reference light will interfere with the light in the sensing fiber at the 2×3 coupler. The interference signal is received by three PDs, and the three-channel signal is sampled by a data acquisition card (National Instruments USB 6210). And the ECG signal is also sampled by the same data acquisition card.

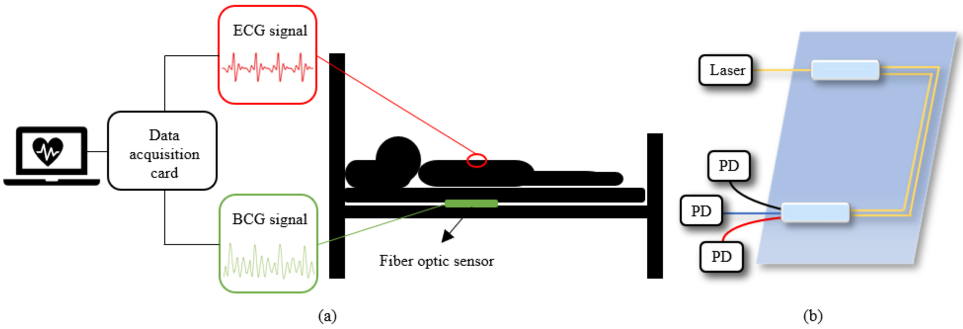

Fig. 4.1. (a) System setup, (b) fiber optic sensor structure based on 2 × 3 *coupler.*

4.2.3 Results and discussion

Fig. 4.2 shows the sleep data for 7.5 hours, the blue line is the ECG signal, and the red line is the BCG signal. The small image at the top of the figure shows the detailed information of ECG and BCG from 10100 s to 10150 s. In addition to being "insensitive" during the measurement, this sensor can detect tiny body movements during sleep due to the high sensitivity of the fiber-optic interferometer. Compared with the BCG signal, the data of the ECG signal is very stable all night, and the weak body movement during sleep has almost no effect on the signal. In the BCG signal, the signal amplitude increases significantly during body movement. The algorithm can easily analyze the sleep status using the BCG signal.

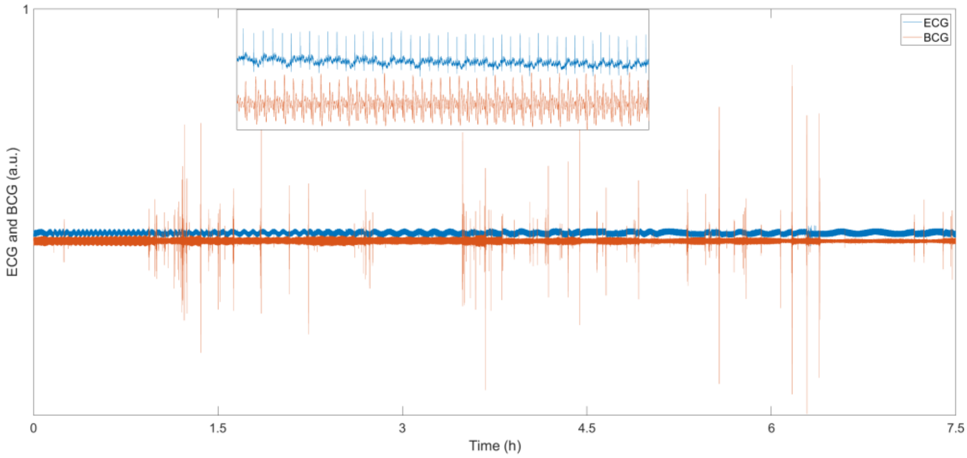

Fig. 4.2. BCG and ECG sleep signals.

Fig. 4.3 shows the HR calculated from the ECG signal and the BCG signal. During sleep, the HR basically fluctuates around 55 bpm. When the subject's body has small movements, the HR will also increase rapidly. As the body calms down, the HR returns to around 55 bpm. The correlation between the HR calculated by ECG signal and the HR calculated by BCG signal is 0.9907, which shows that the HR monitoring system based on FOS can be a good substitute for the traditional ECG system for sleep monitoring.

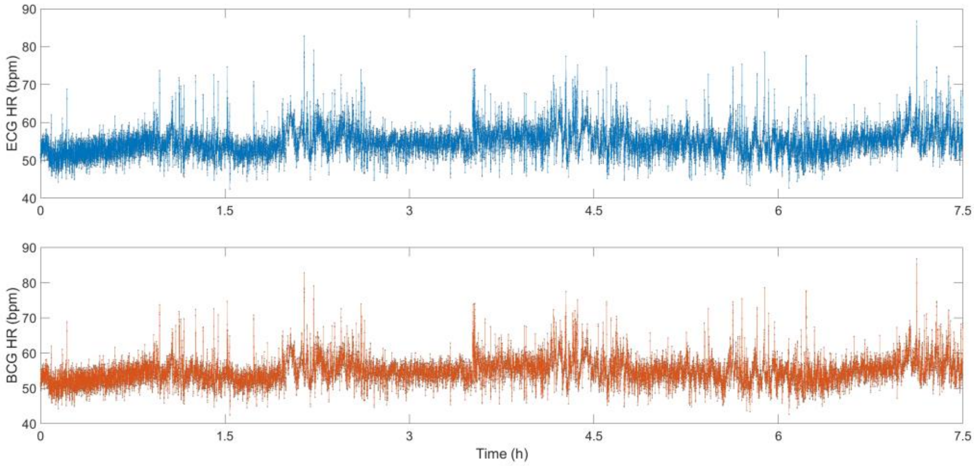

Fig. 4.3. HR signal calculated from BCG and ECG signals.

4.3 Pulse detection

4.3.1 Overview

Pulse diagnosis is the essence of Chinese medicine [122]. In recent years, with the rapid development of medical technology, people's requirements for medical pulse measurement are getting higher and higher. The pulse is the arterial pulse of the human body, and the condition of the pulse reflects the physiological health of the human body to a certain extent. The measurement of the human pulse is important data to measure whether the human body is healthy or not and can be used for pathological analysis. However, traditional pulse diagnosis relies on human subjective judgment, which affects the scientific nature of pulse diagnosis. Accurate monitoring of physiological signals such as pulse, heart sound, BP, and ECG can effectively obtain the health condition of the cardiovascular system [78,123]. At the same time, people also try to evaluate and diagnose the pathological changes in the human cardiovascular system based on the variability of the pulse wave.

When measuring the pulse, it is greatly affected by human factors and environmental factors. The shortcomings of traditional pulse measurement, such as long time and inaccurate measurement, have been gradually replaced by new technologies [124]. The human pulse contains a lot of physiological information, and an experienced doctor can make a diagnosis based on the signals from the pulse. Pulse measurement is not only limited to manual measurement but also electronic instruments and other equipment can be used to effectively measure accurate data in a short period of time, allowing clinicians to diagnose patients in a short period of time.

Currently, pulse measurement mainly includes piezoelectric, piezoresistive, photoelectric, and other methods [125]. Among them, the piezoelectric type and piezoresistive type convert the pulse into a signal output through micro-pressure materials such as piezoelectric sheets and bridges; the photoelectric type converts the light transmittance during the pulse beating process in the blood vessel through reflection or reflection. Changes are converted to signal outputs. With the continuous improvement of the precision requirements of pulse measurement equipment, the currently used pulse sensors still face severe challenges in terms of sensitivity and signal-to-noise ratio. The existing technology has been unable to meet the current precision requirements for pulse measurement equipment. How to design a method to measure the human pulse wave accurately has become the focus of research by those skilled in the art.

4.3.2 System structure

The wrist pulse sensor is based on a high-sensitivity fiber optic MZI. It contains two 3 dB couplers that act as optical splitters and optical couplers. The PDs convert the light intensity change signal carrying the pulse signal into an electrical signal.

Signal fading is a common problem for MZI, where the offset point shifts and the sensitivity change accordingly [126]. It can lead to pulse signal distortion. There are many phase modulation methods to solve this problem, such as active homodyne and passive homodyne. We use the 3×3 demodulation scheme to solve this problem [127].

The proposed wrist pulse sensor uses a 3×3 coupler to replace the 1×2 coupler in the traditional MZI. It has three outputs with the phase difference of 120°, and the signals are received by three PDs.

The two arms of the MZI used to measure the wrist pulse are 14 cm and 14.5 cm, respectively. As shown in Fig. 4.4(a), the two arms are bent side by side into an arc, and both sides are fixed on the pulse diagnosis table. During the experiment, the hand was placed on the table, and the optical fiber was fixed on the wrist with a mechanical finger, as shown in Fig. 4.4(b). The pulse will cause the optical path difference between the two arms, and the pulse waveform can be obtained by the change of the interference signal. After the signal collected at the sampling rate of 5000 Hz is processed by the BPF, a satisfactory pulse signal can be obtained.

(a) (b)

Fig. 4.4. System setup.

4.3.3 Results and discussion

Fig. 4.5 shows three signals collected simultaneously, one expected and two reference signals. The blue line is the PPG signal used as the HR reference. According to previous work, the fiber optic sensor-based BCG signal is used as a reference for RR [127], as shown by the yellow line in Fig. 4.5. The red line is a fiber optic MZI-based pulse signal that can calculate HR and RR simultaneously. In order to obtain a satisfactory pulse wave, we use a 0.5-15 Hz BPF to process the wrist pulse signal.

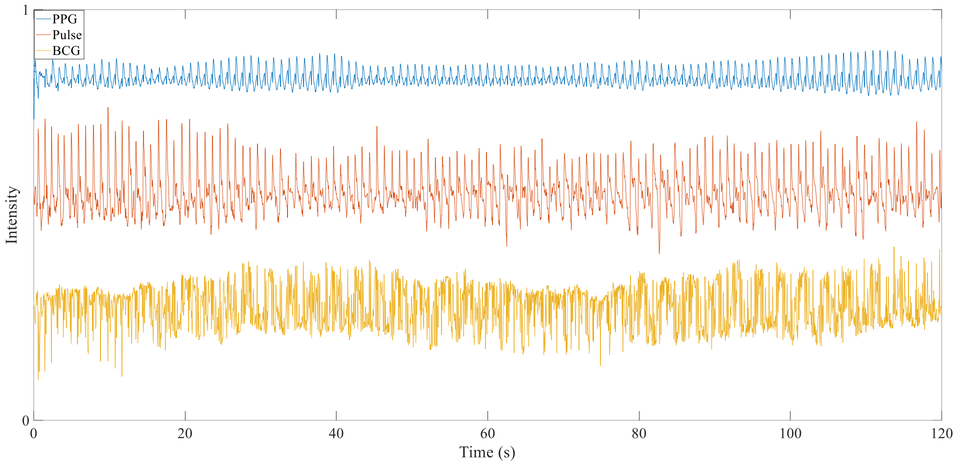

Fig. 4.5. PPG signal, BCG signal, and fiber-optic MZI-based wrist pulse signal.

In recent years, there has been increasing evidence that HR is a major correlator of BP and is associated with increased cardiovascular and cardiovascular disease risk [128]. According to the results in Fig. 4.5, both the wrist pulse signal and the PPG signal have been processed by a 0.5-15 Hz BPF to remove low-frequency effects. FFT is performed on the two signals to obtain their spectral information, as shown in Fig. 4.6. The highest peaks in Fig. 4.6(a) and (b) are both 1.04 Hz. It can be calculated that the average HR of the subject for 120 seconds is 62.4 bpm. The experimental results show that the HR measurement based on the wrist pulse is the same as the HR calculated from the reference signal.

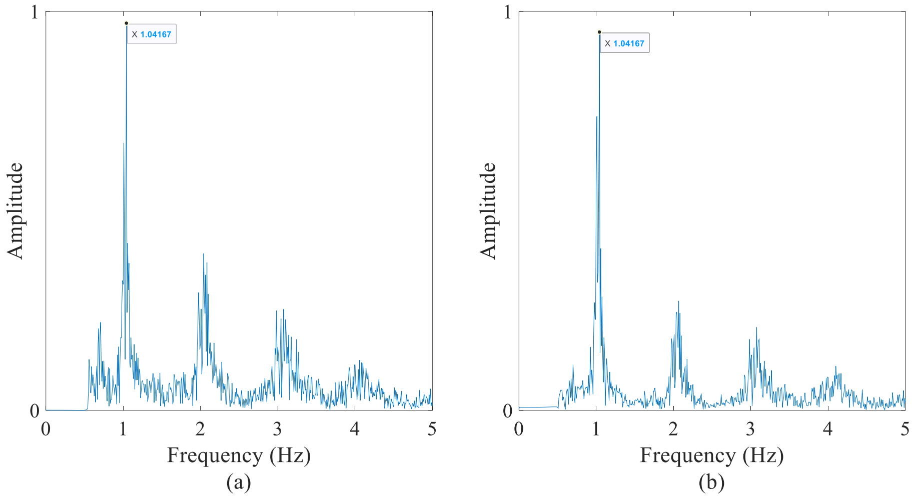

(a)
(b)

Fig. 4.6. (a) Frequency of fiber-optic sensor-based wrist pulse signal, (b) frequency of reference sensor-based pulse signal.

RR is also an important vital sign parameter. It is used to monitor disease progression, and abnormal RR is an essential marker of severe disease. Studies have shown that RR is superior to other necessary measures such as pulse and BP in distinguishing stable patients from high-risk patients [129]. In the previous data processing work, in order to obtain a satisfactory pulse wave, the respiratory information was filtered out. Change the BPF parameter to 0.1-15 Hz, and another peak of 0.33 Hz will appear in the frequency domain of the wrist pulse signal, as shown in Fig. 4.7(a). A peak at 0.34 Hz can be found in the frequency spectrum of the BCG signal shown in Fig. 4.7(b). The calculated RR from the two signals were 19.8 bpm and 20.4 bpm, respectively.

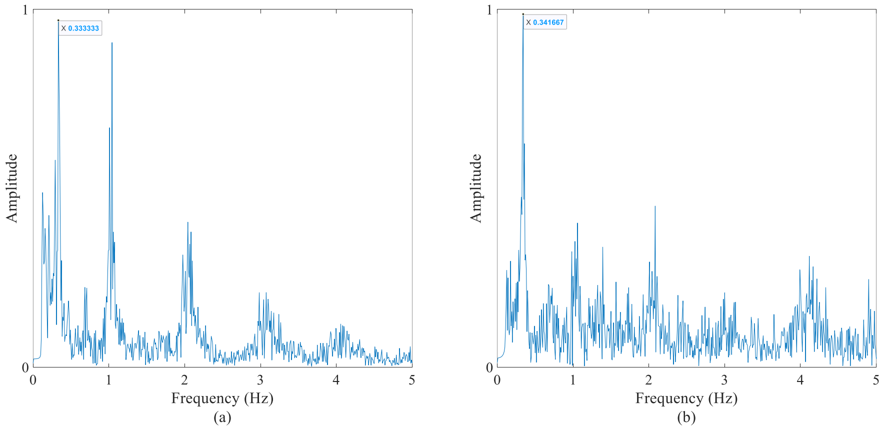

Fig. 4.7. (a) Frequency of fiber-optics sensor-based wrist pulse signal, (b) frequency of reference sensor-based respiration signal.

4.4 Driver monitoring

4.4.1 Overview

Long-distance travel tends to exacerbate driver fatigue, making it challenging to maintain sustained attention during the journey. The development of autonomous driving technology has made it easier for drivers to become fatigued, but drivers still need to be vigilant at all times before fully autonomous driving can be achieved. As road safety becomes an increasingly important topic [130], any research on this topic is very important for drivers. As a result, modified car seats capable of measuring and monitoring the driver's vital signs could become an integral part of every car. Researchers are currently working on various driver response systems, primarily detecting fatigue, stress, and the driver's health [131].

Since driver fatigue and drowsiness are the main causes of a large number of road accidents, assistance systems that monitor driver drowsiness and alert drivers when they are alert can play an important role in preventing such accidents. B. Hariri et al. track and monitor the driver in real-time using an on-board camera to detect whether the driver is yawning. A. Kolli et al. proposed a system using a single thermal imaging camera for driver emotion recognition [132]. M. Walter et al integrated capacitive ECG and piezoelectric film-based BCG into car seats to monitor the driver's HR [133]. However, camera-based sensors are based on classical image processing techniques rather than physiological sensors, especially drowsiness and fatigue detection rely on the recognition of multiple photos, which takes a long time [134]. From a practical point of view, the cable tie-down solution is not an option for driver condition monitoring outside of experiments. Therefore, unobtrusive and non-contact driver state monitoring using physiological information is currently receiving increasing attention.

Early BCG recording systems were usually designed longitudinally, corresponding to the z-axis of a standing person. Weight is also measured on this axis [34,135]. With the development of simple and inexpensive cushion-based BCG measurement instruments, this technique has received renewed interest in recent years.

BCG sensors have been attempted to be integrated into car seats, however, it was shown that engine vibrations still prevent reliable BCG monitoring in moving vehicles. Monitoring of important functions of the car faces many signal distortion problems due to interference caused by the vehicle and the driver itself [136]. The implementation of in-vehicle sensors remains a very challenging task today due to the presence of a large number of motion artifacts mainly caused by driving itself. Therefore, some studies use sensor fusion to handle their elimination, which means combining multiple sensors at different locations, even sensors of different types. This approach will be able to reduce the impact of motion artifacts by using advanced adaptive filtering techniques.

This paper proposes to use two independent optical fiber sensors to collect signals simultaneously, and eliminate the influence of simulated engine and other vehicle vibrations on BCG signals by calculating the frequency spectrum of the two signals.

4.4.2 Methods

The system is shown in Fig. 4.8. The monitoring system contains two FOSs, a main sensor for measuring vital signs and a reference sensor for noise cancellation. The main sensor is placed inside the cushion, as shown in Fig. 4.8 (a). The reference sensor is placed under a seat (Audi A3L driver seat), as shown in Fig. 4.8 (b). The car seat is placed on a vibration table, and the subject sits on the seat during the experiment. Then the vibration table is turned on, and the subject can feel the obvious vibrations while sitting in the car seat.

Two 1550 nm pigtailed DFB lasers with a spectral width of 0.1 nm are used as the laser source and 6 photodetectors are used to collect optical signals. After using the 3×3 demodulation scheme, the noisy signal and noise signal can be obtained respectively.

Fig. 4.8. (a) The main sensor placed in the seat, (b) system setup.

Since the purpose of this study is to recover the noisy BCG of the main sensor from the noise signal of the reference sensor, the response of the two sensors should preferably be close. In order to realize better performance, two FOSs with similar transmission spectrums were selected. The transmission spectrums of the two FOSs can be observed by an optical spectrum analyzer (YOKOGAWA AQ6370D), as shown in Fig. 4.9.

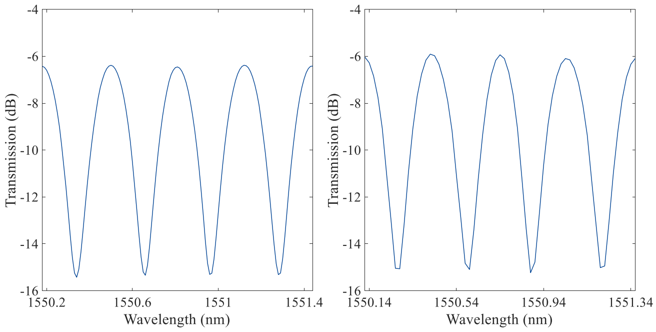

Fig. 4.9. (a) Transmittion spectrum of the main sensor, (b) Transmittion spectrum of the reference sensor.

In many practical application scenarios, the only signal available is a noisy signal. In these cases, random noise cannot be removed, but reducing the average impact of noise on the signal spectrum is a feasible operation.

Spectral subtraction is a simple and effective noise reduction method to solve this kind of problem. The average signal spectrum and the average noise spectrum are estimated and subtracted from each other in a fraction of the recordings, thereby increasing the average SNR. Assuming the signal is distorted by broadband, stationery, and additive noise, the noise estimate is the same during analysis and recovery, and the phase is the same in the original and recovered signals. The noisy signal model in the time domain is given by:

$$y(t) = x(t) + n(t), \tag{4.1}$$

where y(t), x(t) and n(t) are the pulse signal, the noise and the noisy signal respectively, and t is the discrete time index. In the frequency domain, the noisy signal model of equation (2) is expressed as:

$$Y(\omega) = X(\omega) + N(\omega), \tag{4.2}$$

where $y(t)$, $x(t)$ and $n(t)$ are the sampled noisy BCG, pure BCG, an4.d additive noise, respectively. Because the heartbeat signal is non-stationary and time variant, the noisy BCG signal can be processed as speech signal. The power spectrum is given by:

$$|Y(\omega)|^2 = |X(\omega)|^2 + |N(\omega)|^2 + X^*(\omega)N(\omega) + N^*(\omega)X(\omega). \tag{4.3}$$

Since the noise is uncorrelated with the pure BCG:

$$|Y(\omega)|^2 = |X(\omega)|^2 + |N(\omega)|^2. \tag{4.4}$$

Then the BCG signal can be calculated by:

$$|X(\omega)|^2 = |Y(\omega)|^2 - |N(\omega)|^2, \tag{4.5}$$

where $|Y(\omega)|^2$ can be obtained by the main sensor, and $|N(\omega)|^2$ can be obtained by reference sensor. Thus, the noise-reduced signal $|X(\omega)|^2$ can be obtained, and $x(t)$ can be obtained by performing inverse Fourier transform on $|X(\omega)|^2$.

4.4.3 Results and discussion

Fig. 4.10 shows the noisy BCG data from the main sensor and the noise signal from the reference sensor. When the vibration table is working, the amplitude of the noise signal is close to that of the BCG signal, causing severe interference to the raw BCG signal from the main sensor.

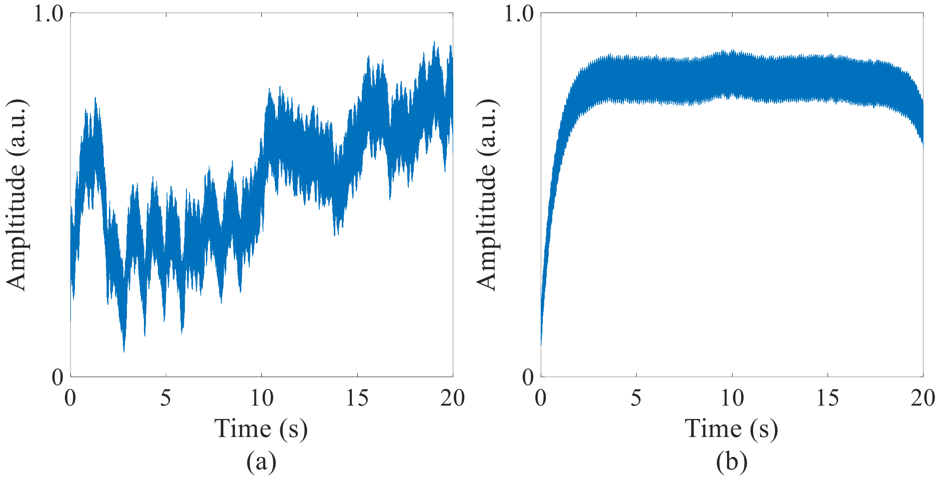

Fig. 4.10. (a) Noisy BCG data from the main sensor, (b) Noise signal from the reference sensor.

The signal in Fig. 4.10(a) is filtered using a BPF with a low cutoff frequency of 0.7 Hz and a high cutoff frequency of 30 Hz, and the result is shown in Fig. 4.11(a). It is difficult to accurately identify the J peak of BCG from the signal in Fig. 4.11(a), which brings difficulties to subsequent data analysis. After spectral subtraction processing with the noise signal collected by the reference sensor, the quality of the BCG signal is effectively improved, and the result is shown in Fig. 4.11(b). It is easy to find the exact J-peak using the "findpeak" function of MATLAB and calculate the HR of 62 bpm.

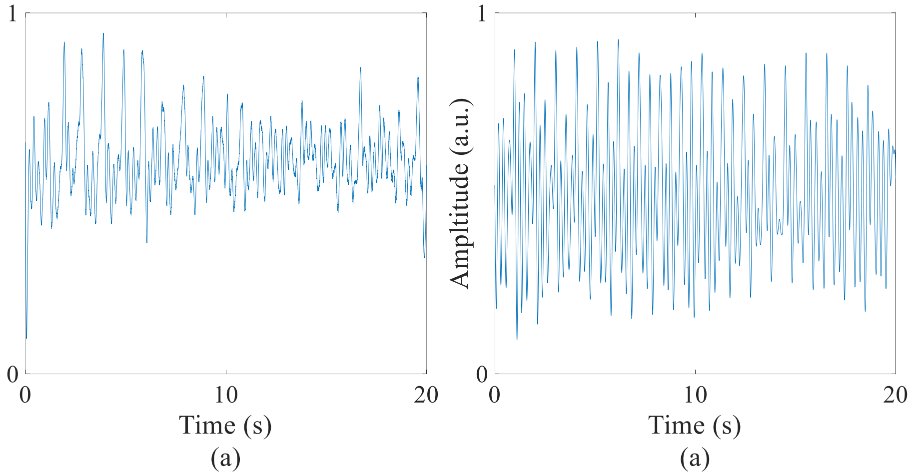

Fig. 4.11. (a) Filter-based BCG signal using only the main sensor, (b) spectral subtraction-based BCG signal using dual sensors.

4.5 Summary

In this chapter, an FOS-based sleep monitoring system is proposed for sleep stage analysis. In sleep state monitoring, the BCG system does not need to affix uncomfortable patches to the body, nor does it require a wired connection on the body, so it can monitor the sleep state in real-time without affecting sleep. The BCG system based on FOS has shown the accuracy of HR close to that of ECG equipment, and it can be used as a reliable device for HR analysis. Moreover, it is small, light, and low in cost, and it will have a good development in the field of intelligent health monitoring. In addition, the fiber-optic MZI-based wrist pulse sensor proposed in this chapter can be used to monitor HR and RR simultaneously. The HR calculation result of the sensor is completely consistent with the reference PPG signal. And the error between the RR result and the reference signal is within 1 breath per minute. The wrist pulse sensor based on optical fiber has great development prospects in the field of wearable devices. Moreover, a dual FOSs-based driver vital signs monitoring system is proposed in this chapter for extracting heartbeats in an environment that simulates car vibrations. The signal is processed by spectral subtraction, which can effectively eliminate the influence of simulated engine and other vehicle vibrations on the BCG signal, and significantly improve the accuracy of heartbeat extraction.

Chapter 5

BCG analysis

5.1 Introduction

Long-term and real-time services are essential for heartbeat monitoring whether in the clinic or at home. They can provide early detection of CVDs and avoid severe cardiovascular events. Benefiting from the development of information technology, vital signs sensors can be integrated with the IoT systems to monitor the physiological status, which is called the IoMT systems. The sensors can monitor the vital signs such as heartbeat, breathing, and temperature from users continuously and transmit these data to remote facilities for further analysis. However, long-term monitoring can produce a lot of data, and IoMT systems need to collect and store data from abundant sensors, which both results in high pressure on the transmission systems. Thus, it is necessary to develop signal compression algorithms for BCG signals.

5.2 Cardiac variations

5.2.1 Overview

In modern society, medical care is receiving more and more attention, and people are willing to invest more in this field. Monitoring the health of the elderly is essential in an aging society. In the past, many examinations could only be performed by medical staff, but many diseases such as AF, hypertension, myocardial infarction and heart failure require long-term monitoring. These requirements mean that medical services previously limited to hospitals need to gradually extend to people's homes to support their daily medical care.

For people with a high risk of heart disease, regular assessment of their cardiovascular parameters and taking measures at an early stage can reduce the risk of disease. For people with a high risk of heart disease, regular assessment of their cardiovascular parameters, and taking measures at an early stage can reduce their risk of disease. For patients with cardiovascular diseases (such as heart failure), implantable devices are often used for treatment [137,138]. More and more evidence shows that non-invasive monitoring outside the clinical environment can achieve early detection of CVD risks (such as arteriosclerosis) [139, 140]. However, cardiovascular health needs to be judged by many aspects. Parameters such as BP, HRV, and cardiac contractility must be measured accurately. Neither medical nor household equipment can satisfy long-term monitoring in a non-clinical environment. Common devices in the consumer field include ECG [141], PPG [142], smartwatches, etc. These devices can provide more accurate

HRV information, but cannot reflect mechanical health information of the cardiovascular system. In the research field, researchers have developed ICG that can measure the mechanical health of the cardiovascular system [143]. However, multiple electrodes need to be attached to the patient during measurement, which causes discomfort, and the equipment is bulky and expensive to purchase, which is not suitable for home monitoring.

Compared with other cardiovascular detection technologies, like ECG and ICG, BCG has the advantages of non-invasive and convenient detection. It is proposed to use it for cardiac diagnosis to achieve the same purpose. The research on the physiological significance of ECG signals is very mature, and the physiological importance of BCG signals is still under further study. This paper attempts to prove that FOS-based BCG can be used as a substitute for ECG, and analyzes the effects of different intensities of exercise on the heart.

5.2.2 Experiment

Before acquiring data, the subject was asked to perform four different exercises after resting for 60 seconds: RES exercise, DSE, VM, and running exercise. We hope to find the difference in the effects of different intensities of exercise on HR and PEP.

In Fig. 5.1, the overview of the experiment is shown. When performing breathing exercises, the subject breathes 6 times per minute (0.1 Hz), and the maximum HRV amplitude can be observed at this breathing rate [144]. The DSE was to perform 40 squats as fast as possible. During VM, the subject expiratory against the mouth closed and the nostrils pinched, which forces air into the eustachian tubes and increases pressure on the inside of the eardrum. This maneuver causes changes in BP and HR and is used in conjunction with other tests to diagnose heart abnormalities and treat various conditions, especially certain abnormal heart rhythms.

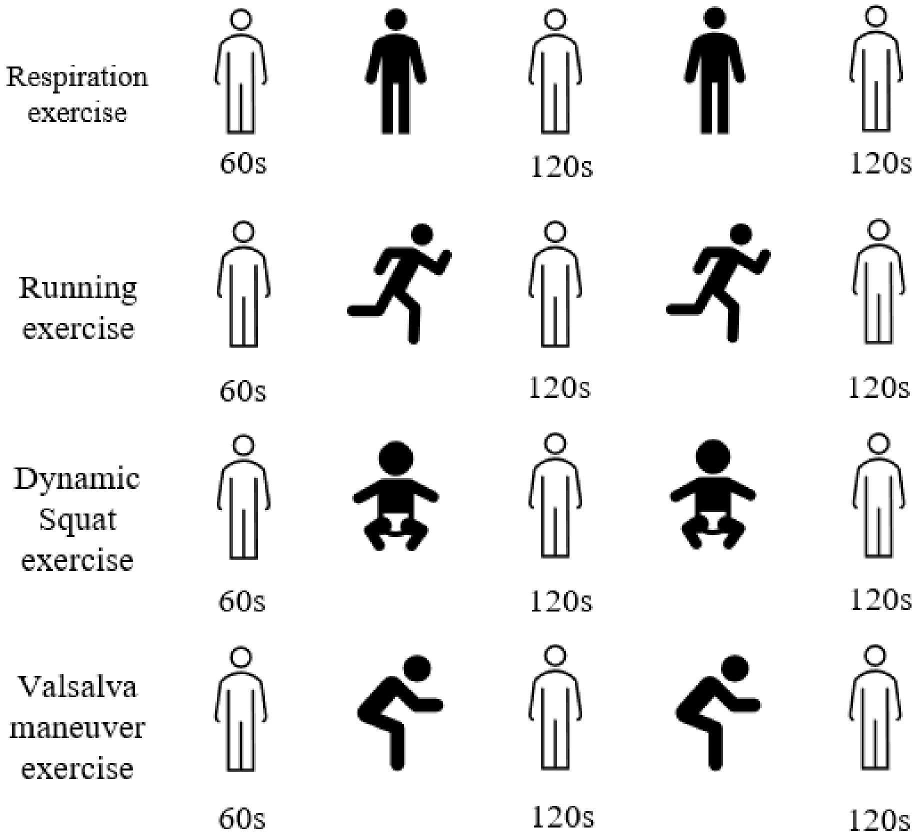

Fig. 5.1. The overview of the experiment.

5.2.3 Results and discussion

The common IBI is calculated from the R-R interval of ECG, called ECG IBI, and used as a reference for IBI validation in this study. The BCG IBI was calculated by the J-J interval. There are a total of 1060 heartbeats in a total of 580s in the four exercises. We use MATLAB to calculate the correlation between the two. The correlation between BCG IBI and ECG

IBI is 0.9862, and the RMSE is 0.0139. The IBI used in the analysis of HRV and PEP in this study was calculated by BCG.

Fig. 5.2 shows the IBI after four different exercises. All exercises increased HR, and the trend was not the same. In Fig. 5.2 (a), the VM was performed in the 10th second and released strains after 15 seconds, marked with red line. During this period, the HR gradually increases and returned to normal after released strains. The mean value of HR is 0.9381 s. In Fig. 5.2 (b) and (c), HR gradually slows down from fast. The mean values of DSE and RUN HR are 0.6572 s and 0.5277 s, respectively. Because running is more intense, the measured initial HR is faster. Fig. 5.2 (d) shows the HR during respiration exercise, and the mean value is 0.8054 s. It increases during inhalation (shortened J–J interval) and decreases during exhalation (extended J–J interval). This is called respiratory sinus arrhythmia (RSA) and reflects changes in cardiac autonomic regulation.

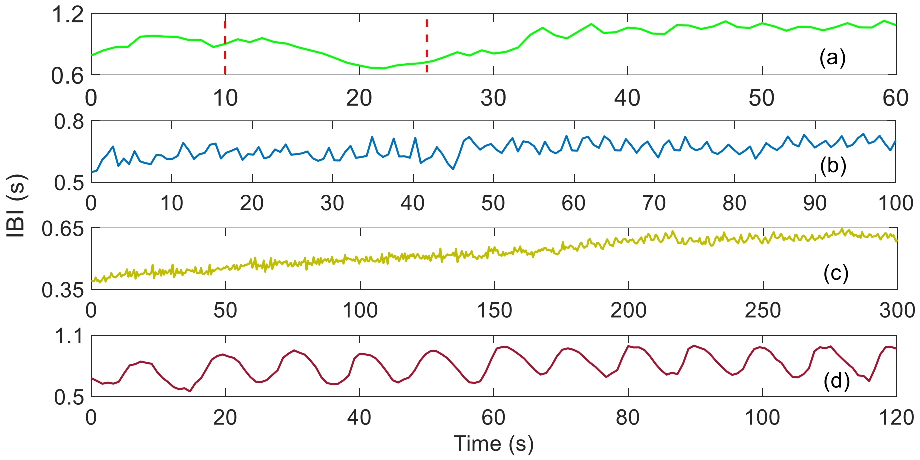

Fig. 5.2. (a) Valsalva maneuver IBI, (b) dynamic squat exercise IBI, (c) running exercise IBI, (d) respiration exercise IBI.

PEP is one of the systolic time intervals, measured from the Q wave of the ECG to the B wave of the ICG. It represents sympathetic activity and can be used to assess myocardial contractility. Because ICG equipment is expensive and the measurement is complicated, RJ interval is usually used as a substitute for PEP. It is defined as the interval between the R peak of ECG and the J peak of BCG, and has been investigated quantitively that the relationship between the PEP and R-J interval follows [38]:

$$Y_{RJ} = 1.05 \cdot PEP + 138, \qquad (6)$$

Fig. 5.3 shows the PEP after four different exercises. In Fig. 6 (a), when the VM starts, the PEP suddenly became smaller. This phenomenon may be due to deep breathing before the start of VM. During this process, the PEP is almost unchanged, and after released strains, it suddenly decreases and then gradually recovers. Throughout the testing process, the mean value of PEP is 116.344 ms. In Fig. 5.3 (b), the PEP mean value is 93.9704 ms, it fluctuates violently and shows no obvious trend after DSE. The PEP variation is shown in Fig. 5.3 (c), the mean value is 63.9383 ms. It fluctuates sharply after running exercise, and the overall trend has gradually increased. In Fig. 5.3 (d), the PEP mean value is 106.2365 ms, which trend is basically the same as HR during breathing.

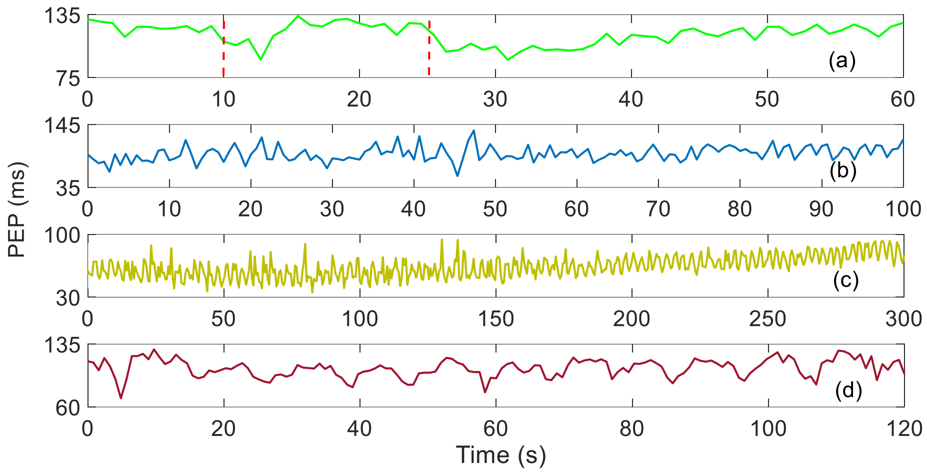

Fig. 5.3. (a) Valsalva maneuver PEP, (b) dynamic squat exercise PEP, (c) running exercise PEP, (d) respiration exercise PEP.

The goal of this study is to investigate IBI and the PEP variation after different exercises. The extremely high correlation between BCG IBI and ECG IBI shows that the IBI calculated by the J-J interval of BCG is accurate enough for HRV analysis. Because the subject needs to breathe quickly and deeply before VM, the larger mutations in HR and PEP may be caused by breathing in the early stage of VM. After the four exercises, the trends of IBI and PEP seem to show that the two are positively correlated to a certain extent. However, during VM, IBI first decreased and then increased, while PEP remained almost at a normal level. This result shows that PEP is not always consistent with the trend of IBI. Under ideal experimental conditions, the breathing rate during the test period should remain constant. However, experiments have shown that individuals cannot fully breathe following a fixed speed. In addition, swallowing was sometimes observed in a few cases, so there are differences in breathing rate. The change of HR and PEP in each breath is not exactly the same. In the same way, the fluctuations in HR and PEP during the whole test may also be caused by irregular breathing. As we all know, sports exercises will speed up HR. VM is the least intense exercise, so the recovery of HR is the fastest. Due to the short exercise time of DSE, HR does not increase as much as running. However, there are obvious differences in the trend of PEP after the two sport exercises. After DSE, the PEP fluctuates between 59 ms and 135 ms, with a central value of 97 ms. After running exercise, the PEP fluctuates between 30 ms and 100 ms, the central value first decreases from 59 ms to 49 ms, and gradually increases to 78 ms in the next 300 s, and there is a tendency to continue to increase. Both PEP values fluctuate greatly, but there is not much change from the normal value of 110 ms in DSE data (the PEP decreases to about 59 ms after running). It is not sure whether it is related to the exercise kinds, or to the intensity and duration of the exercise. During the RES exercise, IBI fluctuates around 0.8 s (0.6 s-1.0 s), and PEP fluctuates around 97 ms (78 ms-126 ms). Both of them change around the value in the normal resting state. All the changes of IBI and PEP show the variations in a healthy heart pumping under parasympathetic regulation after different exercises.

5.3 HRV analysis

5.3.1 Overview

The heart plays a vital role in the human body, maintaining blood flow and delivering nutrients to different cells and tissues. Good functioning of the cardiac system is essential for a healthy life [145]. The state of cardiac well-function is a complex pattern of variability. The ANS controls most of the body's physiological activities, the SNS and PNS innervate the heart and regulate HR. The balance between SNS and PNS affects the consistency in the time domain between heartbeats, which causes HR fluctuations. In 1996, the European Society of Cardiology and the North American Society for Pacing and Electrophysiology pointed out that HRV is the best quantitative indicator for evaluating autonomic nervous activity [147,148]. HRV analysis is one of many indicators of pathological conditions related to cardiovascular health [148]. The HRV represents a physiological phenomenon that may be analyzed to determine the state of the nervous system that controls the heart. The time-domain and frequency-domain information has significant clinical guiding value for predicting heart health. Conventional HRV is usually extracted from ECG signals and refers to the variations in consecutive time intervals between peaks of the QRS complex [149]. While beats per minute can be extracted in HR, HRV is closer to the exact time variation between consecutive heartbeats. In general, time-domain measures of HRV decline with declining health status. Low levels of HRV have been found to be one of the leading causes of death in adults.

However, the current ECG and PPG signals in common use are usually measured by using a device directly contacting with human skin, and the long-term measurement will cause discomfort to the users [150]. For people with allergies, skin contact may cause sensitization. Therefore, it is necessary to investigate non-contact monitoring equipment to obtain human HRV. Whereas BCG signals can be easily obtained by non-contact methods, that is, by sensing micro-strains in the human body caused by each heartbeat. In addition, BCG signals have a good correspondence with ECG and PPG signals [151, 152]. It is practical to adopt BCG as a non-contact and accurate HRV measurement.

Researchers have proposed various BCG measurement methods. For example, in 2007, Postolache et al. used an EMFi sensor installed on the back of a chair to detect mechanical waves generated by the heart to obtain BCG [153]. The signal acquired by their system is characterized by low SNR. After that, in 2012, Shin et al. obtained BCG using a scale that converts weight linearly to voltage [154]. They used the Valsalva maneuver and static exercise to induce changes in the spontaneous cardiac rhythm and estimate BP and HRV. Furthermore, in 2015, Jose et al. proposed a wearable device based on a piezoelectric sensor to measure wrist BCG [155]. And recently, Li et al. proposed a camera-based BCG measurement method. They placed a camera on the subject's head and obtained BCG from tiny head movements [156]. Unlike conventional BCG which captures facial images in a specific environment, this proposed method performs HR measurement by simply capturing any scene anywhere with a camera. However, the aforementioned sensors have limitations. Measurements based on EMFi sensors are less accurate and need adaptive neural network filtering to improve their SNR. Scale-based measurements require the subject to be upright, which can easily introduce motion artifacts. Sensors based on piezoelectric can only be utilized by contacting human body, which may cause discomfort to users. Camera-based measurements also have privacy concerns. Compared with the above methods, FOS is very user-friendly as it does not require body contact and can be used while keeping the user in comfort (sitting or lying down) [157].

Some researchers have analyzed HRV with the BCG signal of healthy subjects [158]. Since the HR of healthy individuals shows regularity in the time domain, further studies are needed to investigate the feasibility of BCG for HRV analysis in subjects with arrhythmias. Fig. 5.4 shows healthy and premature beats subjects' resting ECG IBI and BCG IBI. When premature beats occur, the heart beats about 100 ms earlier. Typically used in studies are the QRS complex and the IJK complex. This study aimed to investigate whether FOS-based BCG could be used as an alternative to traditional ECG signals for HRV analysis. HRV indexes of the time domain (SDSD (standard deviation of successive RR interval differences), SDNN (standard deviation of the IBI of normal sinus beats), RMSSD (root mean square of successive differences between normal heartbeats), and pNN50 (percentage of adjacent NN intervals that differ from each other by more than 50 ms)), frequency domain (VLF (very low frequency), LF (low frequency), HF (high frequency), and LF/HF), and nonlinear (SD1 (standard deviation of each point from the $y = x$ axis), SD2 (standard deviation of each point from the $y = -x + 2\overline{NN}$), and SD1/SD2) were compared. The reliability of the proposed FOS is validated by comparing with a commercial ECG device (AD 8232) which demonstrates its potential application on health monitoring.

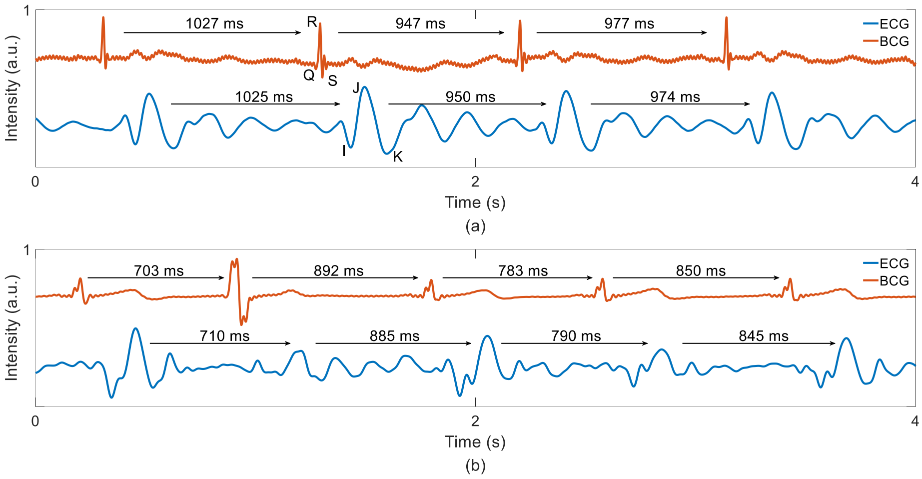

Fig. 5.4. Resting ECG and BCG waveforms of (a) a healthy subject and (b) a subject with premature beats.

5.3.2 Experiment

A total of 5 subjects aged 25, 27, 46, 52, and 54 were included, and subject 1 suffered from premature beats. The HR results were calculated separately by the simultaneously acquired ECG (AD 8232) and BCG (FOS). Each subject was asked to sit on a chair during data collection. The FOS was placed under a mattress for BCG measurement, and three electrodes were attached to the subject’s chest and abdomen for 3-lead ECG measurement. Fig. 2(b) shows the multi-modalities signal acquisition board structure, which is used to collect and demodulate optical signals output by FOS and ECG signal output by AD 8232 module. Then, all signals are transmitted to a computer through a router. The multi-modalities signal acquisition board contains a 1550 nm pigtailed DFB laser with a spectral width of 0.1 nm used as the light source in the FOS system, 3 PDs used to receive the optical signal output by the FOS, an STM32 MCU used for demodulation 3 channels optical signals, an AD 8232 module used for processing ECG signals, and a Wi-Fi module used for transmitting ECG and BCG signals. The FOS consists of a 1×2 coupler and a 3×3 coupler, as shown in Fig. 2(c). Two couplers are spliced using a commercial fusion splicer with a default single-mode fusion program. In the fabrication process, only standard fiber cutting and splicing are required rather than complex glass processing such as tapering, offset splicing, and corrosion with hydrofluoric acid. This ensures the high repeatability, simplicity of manufacture, and high mechanical strength of the device. The light is injected into the 1×2 coupler of the MZI by the DFB laser and interferes at the 3×3 coupler after passing through the sensing arm and the reference arm. The interference light is divided into three signals, which are separately detected by three PDs. The sensing arm and reference arm of FOS are fixed on an acrylic board with polypropylene/polyethylene glue to guarantee full contact between the optical fiber and the acrylic board. After 24 hours, the acrylic board is encapsulated with epoxy resin AB glue to ensure long-term stability for the sensor. Even extremely weak vibrations will induce the change of the optical path difference between the sensing arm and the reference arm, that is, the phase difference between the two beams of light will change. Variations in phase difference cause variations in the intensity of the interference light. All external perturbations, including breathing, heartbeat, environmental temperature, will cause intensity changes of output signal. After removing the noise signal, the respiratory signal and heartbeat signal can be filtered and obtained simultaneously taking advantage of their different frequencies. All the collected data can be viewed on the computer with processed waveforms and calculated HR, as shown in Fig. 2(d). ECG HR and BCG HR are calculated by calculating the number of R peaks and J peaks per minute. The HRV is a measure of the variation in time between each heartbeat (ECG IBI and BCG IBI).

Since the paced respiration will significantly change the amplitude of HRV, the system acquired all four channels (three channels of BCG signals and one channel of ECG signals) at a sampling frequency of 1000 Hz to obtain more accurate data. Prior to conducting the study, informed consent was obtained from all subjects for participation. During the paced respiration experiment, each subject sat on a comfortable chair in a natural posture in a quiet room. They were asked to breathe at a fixed rate of 0.1 Hz (6 breaths per minute) and 0.25 Hz (15 breaths per minute) to induce changes in cardiac autonomic rhythm. Every test lasted 5 minutes and was repeated 5 times. Before the paced respiration experiment, the stability of the system was validated. Resting BCG and ECG were collected from 5 subjects every 3 days, and a total of 10 measurements were performed for each subject.

A 1550 nm DFB laser is used as the light source in the FOS system. Since the FOS is based on the principle of interference, the changes of the external environment may cause the random phase drift of the sensor, which will make the working point of the fiber optic interferometer deviate from the center of the linear region. The random drift of the working point can seriously affect the working state of the interferometer. Thus, a 3×3 demodulation method was applied for analyzing the BCG signal, that is, using a 3×3 coupler to divide the interference light into three beams with a phase difference of 120°. The light emitted from the DFB laser is transmitted into the reference and sensing fibers through a 1×2 coupler. Then the beams of light transmitting in the reference and sensing arms will interfere at the 3×3 coupler. The output light intensity of the interferometer can be calculated using the equation below:

$$I_k = D + I_0 \cos[\varphi(t) - (k-1)(2\pi/3)], \tag{5.1}$$

where $\varphi(t)$ is the phase difference of light signals, D is the average value of output light intensity, I_0 is the peak intensity of interference fringes, k is the number of the output light path, $k = 1, 2, 3$.

In practical application, $\varphi(t)$ includes phase changes caused by the measured information and the environment variation which can be expressed as:

$$\varphi(t) = \phi(t) + \psi(t), \tag{5.2}$$

where $\varphi(t)$ represents the signal to be measured, and $\psi(t)$ is the phase difference caused by environmental changes.

The signal light emitted from a broadband source (BBS, SLED-1488/1650-10-FA-B, Shanghai Mai Xuan Laser CO., LTD) is launched into the interferometric FOS and the transmission spectrum is detected by an optical spectrum analyzer (YOKOGAWA AQ6370D) with a resolution of 0.01 nm, as shown in Fig. 3. Four interference dips can be observed in the spectrum at wavelengths 1549.4, 1549.72, 1550.03, and 1550.34 nm, respectively. All these dips can be used for BCG sensing.

HR is measured by the number of contractions of the heart per minute. The results of this experiment are calculated from the number of R peaks or J peaks in a minute. IBI is a scientific term used in reference to the time interval between individual beats. It is calculated from the time interval between two adjacent R or J peaks. The R peak corresponds to the peak of each QRS complex of the ECG, and the J peak corresponds to the peak of each IJK complex of the BCG. The R peaks of the ECG signal are detected by the "findpeaks" function of MATLAB. The reference IBI is calculated from the RR interval of the ECG. The BCG signal with the signal fading resolved is demodulated using a previously proposed method [158]. Motion artifacts can increase power in all frequency bands, significantly affecting time and frequency domain results. Motion artifacts are also removed using the previous method, and then accurate IJK complexes are obtained.

5.3.3 Stability experiments

Fig. 5.5 shows the results of the one-month system stability test. Taking ECG HR as a reference, the error of BCG HR is within 1 bpm, and the error between each BCG IBI and ECG IBI does not exceed 20 ms.

HR results are calculated from the number of R peaks or J peaks in a minute. IBI results are calculated from the time interval between two adjacent R or J peaks. The bars show the results calculated by ECG and the red error lines show the errors between BCG results and ECG results.

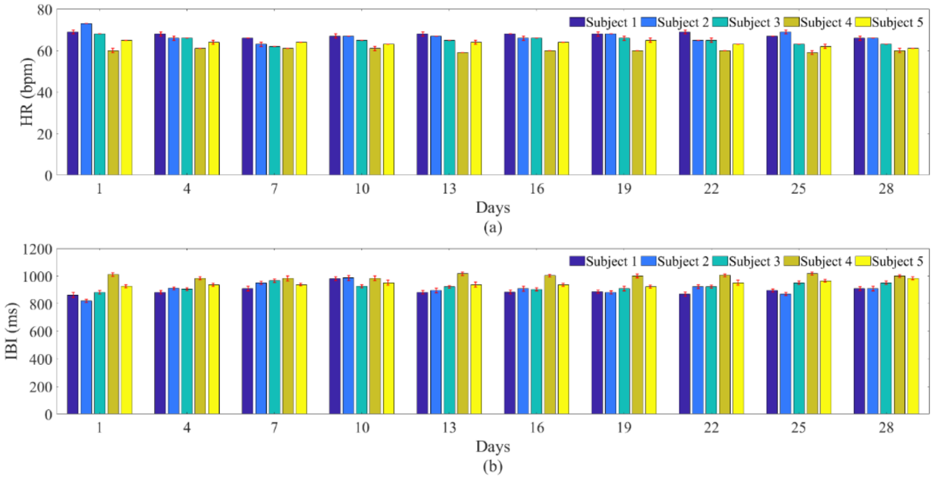

Fig. 5.5. One-month system stability test results of (a) HR and (b) IBI. HR results are calculated from the number of R peaks or J peaks in a minute. IBI results are calculated from the time interval between two adjacent R or J peaks. The bars show the results calculated by ECG and the red error lines show the errors between BCG results and ECG results.

5.3.4 Instantaneous HR

Short-term HRV typically requires monitoring cardiac variability over a set period (usually 5 minutes). In this experiment, all subjects were asked to perform a 5-minute paced respiration to observe the variations in their HR. The HR calculated from the JJ interval extracted from the BCG signal and the HR calculated from the RR interval extracted from the ECG signal showed a high correlation, with correlation coefficients of 0.9971 and 0.9581 for healthy and premature beats subjects, respectively. Fig. 5.6(a) and (b) show the instantaneous HR of a healthy subject at 0.1 Hz and 0.25 Hz paced respiration, respectively. Fig. 5.6(c) and (d) show the instantaneous HR of a subject with premature beats at 0.1 Hz and 0.25 Hz paced respiration, respectively. It is obvious that the HR slows down during exhaling and increases during inhaling. This phenomenon is called RSA. In healthy individuals, RSA can be increased by slow, deep breathing. Changes in respiratory rate can produce large-scale changes in RSA amplitude without affecting vagal tone [19]. The results also revealed an inverse relationship between HRV amplitude and respiratory rate. Breathing at 6 bpm resulted in a more significant change in HR than breathing at 15 bpm for all subjects. This suggests that the vagus nerve is more active at lower respiratory rates. This is consistent with the experimental results proposed by Grossman [159]. Although paced respiration brought varying degrees of periodic HR variation, the mean HR did not change significantly during this period because of unvaried vagal tone.

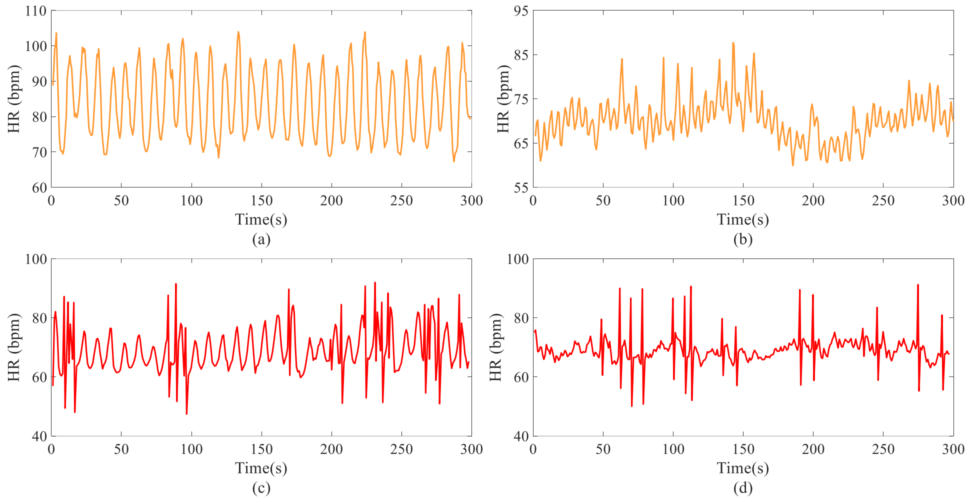

Fig. 5.6. Instantaneous HR of a healthy subject at (a) 0.1 Hz and (b) 0.25 Hz paced respiration. Instantaneous HR of a subject with premature beats at (c) 0.1 Hz and (d) 0.25 Hz paced respiration.

Fig. 5.7 shows the RSA amplitude of paced respiration at 0.1 Hz and 0.25 Hz. For each subject, the amplitude of RSA change at the respiratory rate of 0.1 Hz was more significant than that of 0.25 Hz. At both rates, RSA amplitudes decreased with age increasing. Greater RSA reflects increased baroreflex sensitivity, which worsens with age. Many abnormal heartbeats during the experiment made the RSA amplitude of subject 1 much larger than that of the other four subjects.

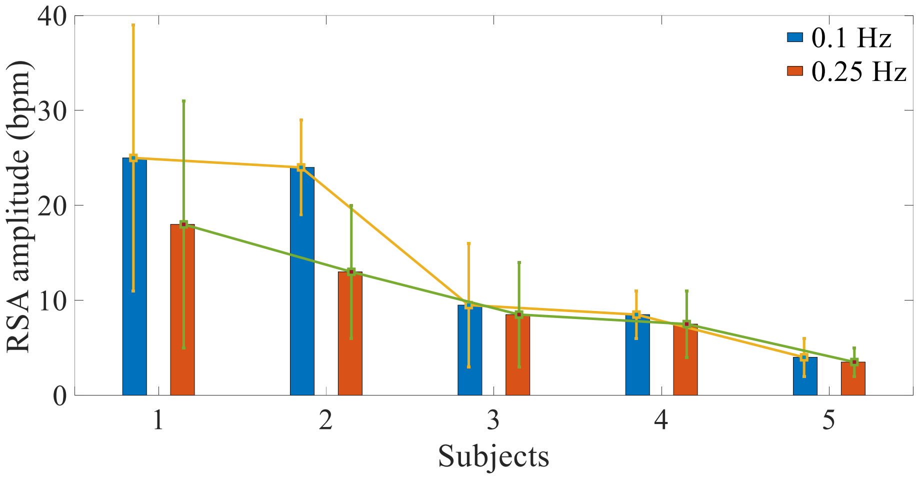

Fig. 5.7. (a) RSA amplitude at 0.1 Hz and 0.25 Hz paced respiration.

5.3.5 Resonance frequency breathing

There is a delay between respiration and cardiac oscillations during spontaneous breathing that decreases as the respiratory rate decreases and disappears when the respiratory rate reaches approximately 0.1 Hz [160]. The combination of respiratory rhythm and heart rhythm by slowing down the respiratory rate is called resonant breathing, and a respiratory rate of 0.1 Hz is often referred to as the "resonant frequency" [161,162]. When the respiratory rate was 0.1 Hz, all natural and imposed cardiac oscillations occurred at the same frequency, and the amplitude of the imposed cardiac oscillation was the largest. This is slow diaphragmatic breathing (6 bpm) that maximizes HRV by stimulating the vagus nerve to calm the body's sympathetic nervous system. Resonance was observed in both ECG and BCG signals at 0.1 Hz respiratory rate for each test subject. Fig. 5.8 shows the IBIs of ECG and BCG and respiratory signals of a subject, where the resonance can be clearly observed. The IBI and respiration waveforms rise and fall at the same time, this maximally stimulates the baroreflex and increases RSA.

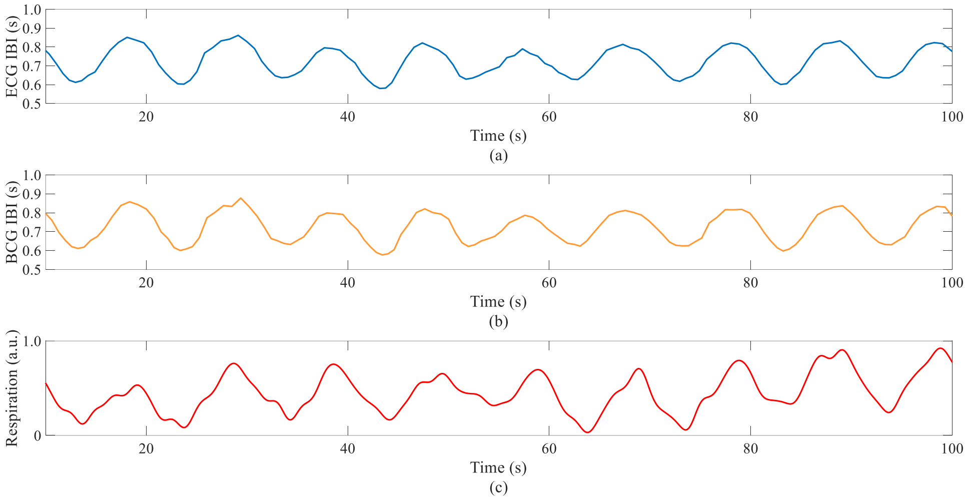

Fig. 5.8. (a) ECG IBI and (b) BCG IBI fluctuations with respiration, and (c) respiration signal. BCG IBI shows similar resonance frequency breathing phenomena to ECG IBI at a respiratory rate of 0.1 Hz.

5.3.6 HRV time domain analysis

Table 1 summarizes the most frequently used time domain HRV indexes. These statistical time domain indexes include beat-to-beat intervals or variables derived directly from the intervals themselves or the instantaneous HR and intervals derived from the differences between adjacent NN intervals [163]. SDNN is the standard deviation of the R-R interval, which reflects the overall level of HRV and is related to the overall regulatory capacity of the ANS system [164]. RMSSD is the mean square root of the quadratic sum of the differences between adjacent R-R intervals, showing the magnitude of the high-frequency component of HRV. RMSSD is generally known as the primary time-domain measure used to estimate vagus-mediated changes reflected in HRV. SDSD is the standard deviation of the difference between adjacent R-R intervals. Similar to RMSSD, it indicates the size of high-frequency components in HRV. pNN50 is the proportion of the difference between adjacent R-R intervals greater than 50ms and also indicates the size of the high-frequency components in HRV. These indicators can be used to assess aspects of cardiac autonomic regulation, stress levels, emotional state, etc. [165].

TABLE I

DEFINITION AND FORMULA OF HRV TIME DOMAIN INDEXES

Index	**Definition**	**Formula (unit)**
SDSD	Standard deviation of differences between adjacent NN intervals	$\sqrt{\frac{\sum_{i=1}^{N}(NN_i - mNN)^2}{N-1}}\ (ms)$
SDNN	Standard deviation of all NN intervals	$\sqrt{\frac{\sum_{i=1}^{N}(RR_i - mRR)^2}{N-1}}\ (ms)$
RMSSD	Square root of the mean of the sum of the squares of differences between adjacent NN interval	$\sqrt{mean\sum_{i=1}^{N}(RR_{i+1} - RR_i)^2}\ (ms)$
pNN50	Percent of difference between adjacent NN intervals that are greater than 50ms	$\frac{count(\lvert NN_{i+1} - NN_i \rvert) > 50ms}{N-1} \times 100\%$

NN: the interval between two adjacent heartbeats, RR: the interval between two adjacent R spikes in the ECG QRS complex.

Fig. 5.9 and Fig. 5.10 show the HRV indexes calculated by ECG and BCG signals under 0.1 Hz and 0.25 Hz paced respiration, respectively. The indexes calculated by the BCG have an error of a few milliseconds from the corresponding indexes calculated by the ECG. This is because the RJ interval changes with the condition of the heart, so the RR interval and JJ interval are not completely constant [166]. Since the respiratory rate of 0.1 Hz causes a larger HRV amplitude, values of SDSD, SDNN, RMSSD, and pNN50 will all be larger than those tested at 0.25 Hz paced respiration. All indexes show acceptable errors at both respiratory rates. The four time domain HRV indexes show a downward trend with age increasing. However, SDSD and RMSSD results from subjects 2 and 3 showed opposite trends with age, which may be related to the health of their heart. In addition, due to the irregular heartbeat, the SDSD of subject 1 was significantly higher than that of subject 2 of similar age.

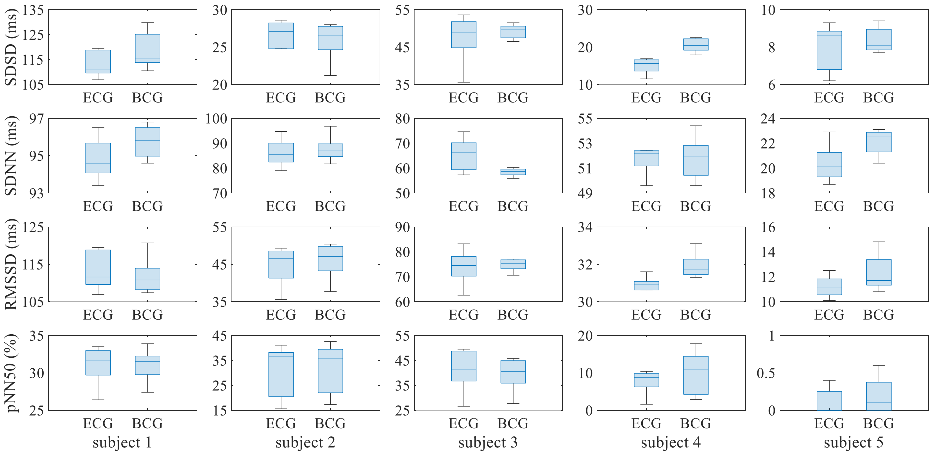

Fig. 5.9. BCG and ECG HRV time-domain indexes at 0.1 Hz paced respiration.

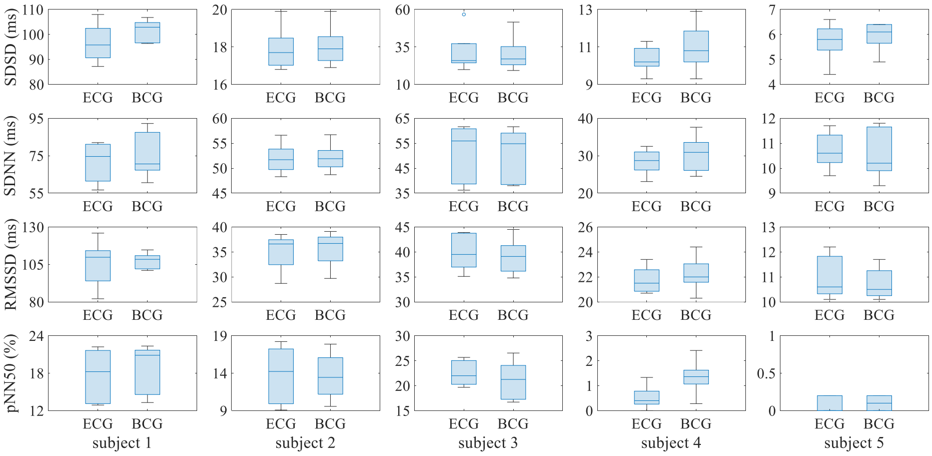

Fig. 5.10. BCG and ECG HRV time-domain indexes at 0.25 Hz paced respiration.

5.3.7 HRV frequency domain analysis

HRV frequency domain indexes are important because they provide information about the distribution of power in different frequency bands of HRV [167]. These indexes reflect ANS activity, which is essential for maintaining homeostasis in the body and for responding to stressors. HR is not constant but oscillates around a mean value, and these oscillations are due to modulations of ANS activity, which control HR through the sympathetic and parasympathetic systems. Abnormal ANS activity is associated with various diseases, such as cardiovascular disease, diabetes, and depression. HRV frequency domain indexes are calculated by analyzing the PSD of HRV signals [168]. PSD is a mathematical representation of the power distribution in the different frequency bands of the HRV signal, showing a function of power and frequency. Power is calculated for each individual component (the area under the portion of the PSD curve related to each component), represented by the total area under the PSD curve. It can be provided in absolute units (ms^2). The frequency domain indexes are divided into three main categories: VLF, LF, and HF bands [169-171]. The band ranges are 0.0033–0.04 Hz, 0.04–0.15 Hz, and 0.15–0.4 Hz. Table 2 shows the definition of HRV frequency domain indexes. LF and HF are used to label parasympathetic and sympathetic control, respectively. The role of VLF in spectral content remains uncertain. The LF/HF ratio is an indicator of the interaction between sympathetic and vagal activity [172]. It is used to assess the distribution of scores between the two systems and it’s also an important marker of sympathovagal balance.

TABLE II

DEFINITION OF HRV FREQUENCY DOMAIN INDEXES

Index	Definition
VLF	Very low frequency power, 0.0033-0.04 Hz
LF	Low frequency power, 0.04-0.15 Hz
HF	High frequency power, 0.15-0.4 Hz
LF/HF	Ratio of LF to HF

Fig. 5.11(a)-(d) show the ECG and BCG HRV PSD of a healthy subject at 0.1 Hz and 0.25 Hz respiratory rate. Fig. 5.11(e)-(h) show the ECG and BCG-derived HRV PSD of a subject with premature beats at 0.1 Hz and 0.25 Hz respiratory rate. Changes in sinus rhythm in the higher frequency domain reflect parasympathetic (vagal) regulation, whereas those in the lower frequency domain reflect parasympathetic and sympathetic regulation as well as involuntary factors. The PSD of the BCG and ECG signals at the two respiratory rates show similar distributions. The LF band is the dominant component of the PSD at 0.1 Hz paced respiration. However, at 0.25 Hz paced respiration, the LF component is significantly reduced, and the components of VLF and HF are increased.

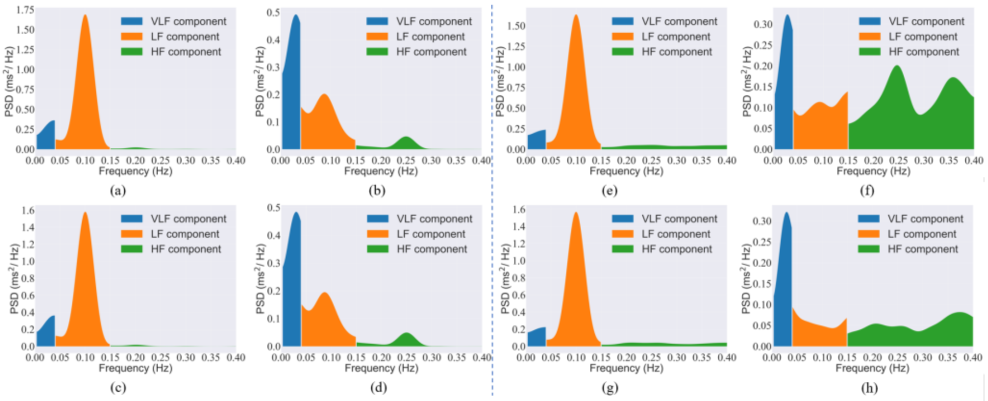

Fig. 5.11. BCG HRV PSD of a healthy subject at (a) 0.1Hz and (b) 0.25 Hz paced respiration. ECG HRV PSD of a healthy subject at (c) 0.1 Hz and (d) 0.25 Hz paced respiration. BCG HRV PSD of a subject with premature beats at (e) 0.1Hz and (f) 0.25 Hz paced respiration. ECG HRV PSD of a subject with premature beats at (g) 0.1 Hz and (h) 0.25 Hz paced respiration.

The resulting frequency spectrum varies widely due to artificially controlled breathing that cannot be maintained consistently. Therefore, the correlation coefficients of LF, HF, VLF and LF/HF calculated from ECG and BCG for each 5-min recording were analyzed in the frequency domain to describe the accuracy of BCG HRV compared to ECG HRV.

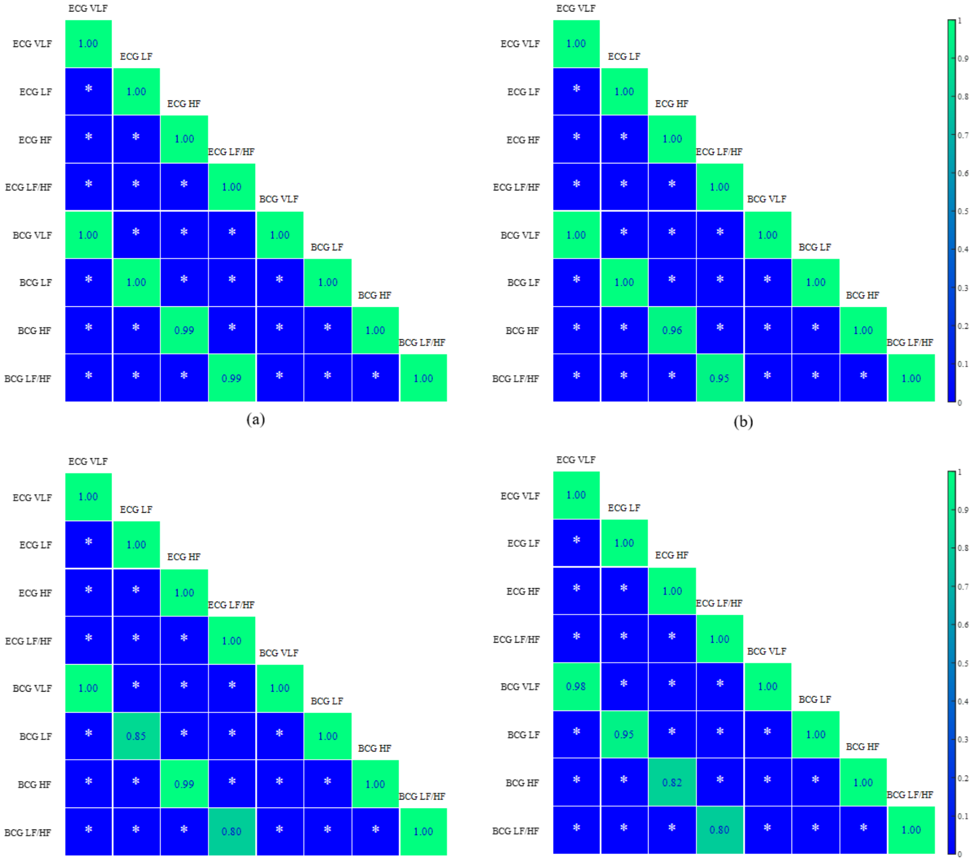

	ECG VLF	ECG LF	ECG HF	ECG LF/HF	BCG VLF	BCG LF	BCG HF	BCG LF/HF
ECG VLF	1.00							
ECG LF	*	1.00						
ECG HF	*	*	1.00					
ECG LF/HF	*	*	*	1.00				
BCG VLF	1.00	*	*	*	1.00			
BCG LF	*	1.00	*	*	*	1.00		
BCG HF	*	*	0.99	*	*	*	1.00	
BCG LF/HF	*	*	*	0.99	*	*	*	1.00

(a)

	ECG VLF	ECG LF	ECG HF	ECG LF/HF	BCG VLF	BCG LF	BCG HF	BCG LF/HF
ECG VLF	1.00							
ECG LF	*	1.00						
ECG HF	*	*	1.00					
ECG LF/HF	*	*	*	1.00				
BCG VLF	1.00	*	*	*	1.00			
BCG LF	*	1.00	*	*	*	1.00		
BCG HF	*	*	0.96	*	*	*	1.00	
BCG LF/HF	*	*	*	0.95	*	*	*	1.00

(b)

	ECG VLF	ECG LF	ECG HF	ECG LF/HF	BCG VLF	BCG LF	BCG HF	BCG LF/HF
ECG VLF	1.00							
ECG LF	*	1.00						
ECG HF	*	*	1.00					
ECG LF/HF	*	*	*	1.00				
BCG VLF	1.00	*	*	*	1.00			
BCG LF	*	0.85	*	*	*	1.00		
BCG HF	*	*	0.99	*	*	*	1.00	
BCG LF/HF	*	*	*	0.80	*	*	*	1.00

(c)

	ECG VLF	ECG LF	ECG HF	ECG LF/HF	BCG VLF	BCG LF	BCG HF	BCG LF/HF
ECG VLF	1.00							
ECG LF	*	1.00						
ECG HF	*	*	1.00					
ECG LF/HF	*	*	*	1.00				
BCG VLF	0.98	*	*	*	1.00			
BCG LF	*	0.95	*	*	*	1.00		
BCG HF	*	*	0.82	*	*	*	1.00	
BCG LF/HF	*	*	*	0.80	*	*	*	1.00

(d)

Fig. 5.12. Correlations between ECG and BCG frequency domain indexes in healthy subjects at (a) 0.1Hz and (b) 0.25 Hz paced respiration. Correlations between ECG and BCG frequency domain indexes in premature beats subject at (c) 0.1 Hz and (d) 0.25 Hz paced respiration.

Fig. 5.12 shows the correlations between ECG and BCG HRV frequency domain indexes for healthy subjects and premature beats subject at 0.1 Hz and 0.25 Hz paced respiration. The results show that BCG HRV at both respiratory rates (6 bpm and 15 bpm) has a strong correlation with

ECG HRV at all frequency bands. The accuracy of experimental results in subjects with premature beats is slightly lower than that in healthy subjects due to small changes in RJ intervals. The accuracy of the LF band at 0.1 Hz is higher than that of 0.25 Hz, on the contrary, the accuracy of the HF band at 0.1 Hz is lower than that of 0.25 Hz. In addition, the accuracy is slightly lower in the LF/HF bands at both respiratory rates.

5.3.8 HRV nonlinear analysis

It must be assumed that the data in the sample is stationary when doing analysis in the frequency domain of HRV which means the method can be invalidated by sudden changes in HR [173]. The change of respiration pattern from spontaneous breathing to controlled breathing can also significantly affect HRV. To overcome this, the Poincaré plot of HRV is proposed in this work which does not require quiescence of the HRV signal and is widely used to monitor changes in the sympathovagal nerve [174-176]. The Poincaré plot is a geometric representation that can visually identify the presence of nonlinear HRV components [177]. It shows the correlation of NN_{i+1} to NN_i, where NN is the beat interval. In the Poincaré plot, SD1 width reflects parasympathetic activity, and SD2 length reflects sympathetic modulation [178]. SD1 is a measure of the short-term HRV that is defined as the width of an ellipse fitted to scatter points of a Poincaré map and may be expressed as the standard deviation of the distances from the identity line ($y = x$ axis) of the Poincaré plot [179-181]. SD2 is the length of an ellipse fitted to the scatter points of a Poincaré map that reflects the long-term HRV and is calculated as the standard deviation of the distance of points from the $y = -x + 2\overline{NN}$ axis. The larger the SD1, the wider the graph, inversely, the larger the SD2, the thinner the graph. SD1/SD2 is the ratio between SD1 and SD2 which reflects the unpredictability of the HR [182]. Table 3 shows the definition of HRV nonlinear indexes.

TABLE III

DEFINITION OF HRV NONLINEAR INDEXES

Index	Definition	Formula (unit)
SD1	Poincaré plot standard deviation perpendicular the line of identity	$SD1 = stddev\left(\frac{\lvert NN_{i+1} - NN_i \rvert}{\sqrt{2}}\right)$
SD2	Poincaré plot standard deviation along the line of identity	$SD2 = stddev\left(\frac{\lvert NN_{i+1} - NN_i \rvert}{\sqrt{2}} - 2\overline{NN}\right)$
SD1/SD2	Ratio of SD1 to SD2	

Poincaré plots may uncover anomalies that cannot be easily detected using traditional time- and frequency-domain measurements. In a clinical setting, Poincaré plot analysis of the RR interval provides prognostic information in patients with heart failure and those predisposed to life-threatening arrhythmias [183]. It has been shown that during heightened sympathovagal activation, HR behavior becomes very erratic. Dynamic analysis of Poincaré plots can better identify these features of HR dynamics compared to conventional HRV analysis techniques. Its strength lies in its ability to identify beat-to-beat periods and patterns in the data. The shape of the Poincaré plots can be used to visually assess sympathovagal activity. An elongated torpedo-like shape with a reduced SD1/SD2 ratio is associated with elevated sympathetic tone, while a more elliptical fan-shaped configuration resulting from an increased SD1/SD2 ratio indicates lower sympathetic tone [180]. The spots become more diffuse when vagal activity increases or sympathetic activity decreases. Fig. 13 (a)-(d) show the Poincaré plots for healthy subjects at 0.1 Hz and 0.25 Hz respiratory rates. Fig. 13 (e)-(h) show the Poincaré plots at respiratory rates of 0.1 Hz and 0.25 Hz for subjects with premature beats. Comparing the top four graphs (Fig. a, b, e, and f) and the bottom four graphs (Fig. c, d, g, and h), the BCG- and ECG-derived Poincaré plots show the similar distributions. The area of the ellipses represents the overall IBI distribution [184]. Compared with respiration of 0.25 Hz, paced respiration of 0.1 Hz brings a greater change in HR, and the areas in Fig. 13 (a) and (c) are significantly larger than those in Fig. 13 (b) and (d).

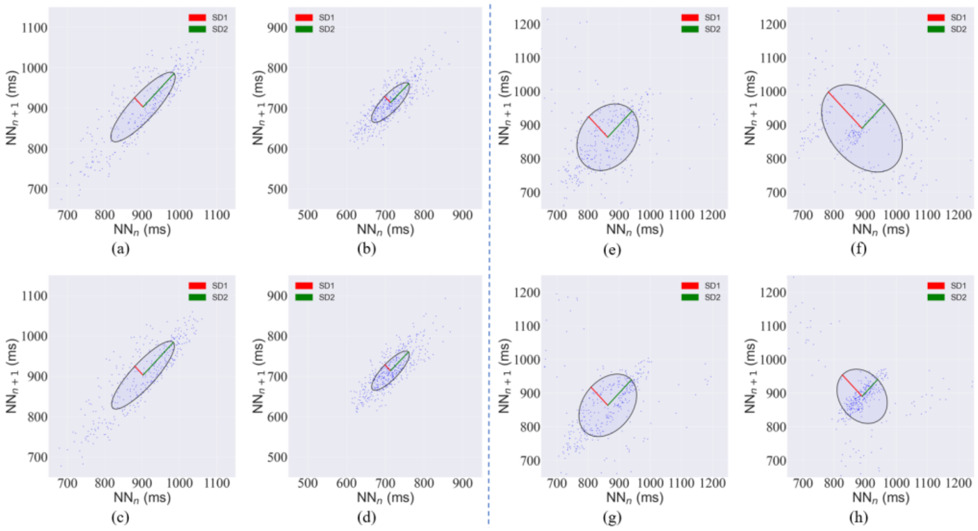

Fig. 13. Healthy subject BCG HRV Poincaré plots at (a) 0.1Hz and (b) 0.25Hz paced respiration. Healthy subject ECG HRV Poincaré plots at (c) 0.1Hz and (d) 0.25Hz paced respiration. Subject with premature beats BCG HRV Poincaré plots at (e) 0.1 Hz and (f) 0.25 Hz paced respiration. Subject with premature beats ECG HRV Poincaré plots at (g) 0.1 Hz and (h) 0.25 Hz paced respiration.

5.4 Summary

In this chapter, cardiac responses after different exercises are studied using a BCG monitoring system based on a 3×3 demodulation scheme. A FOS-based smart cushion is used to replace the traditional inconvenient ECG for HRV. The BCG HRV calculated from the demodulated signal can be used as a new accurate heart condition analysis signal. The correlation between BCG-derived IBI and ECG-derived IBI is 0.9862, and the RMSE is 0.0139. The BCG signal can assess cardiac contractility by analyzing RJ interval with ECG, which is a practical alternative to the PEP. Thanks to its non-contact measurement, BCG based on FOS will become an important part of heart condition analysis.

HRV analysis provides insight into autonomic function. Many diseases, whether cardiac or noncardiac, are associated with alterations in HRV. The FOS-based BCG-derived IBI shows high correlations with ECG-derived IBI, with correlation coefficients of 0.9971 and 0.9581 for healthy and premature beats subjects respectively. During the one-month stability test, the FOS-based BCG monitoring system realized high accuracy. The paced respiration data at 0.1 Hz and 0.25 Hz is collected from 5 subjects of different ages, including a subject with premature beats. Studies have shown that breathing at 0.1 Hz causes larger RSA amplitude, and resonant frequency breathing is observed simultaneously in both BCG and ECG IBI signals. At both respiratory rates, the amplitude of HRV decreases with age increasing. This study also analyzes the short-term HRV accuracy of 5 subjects based on the FOS. Time domain indexes of BCG HRV and ECG

HRV showed minor errors via box plots. Higher correlation coefficients are observed in the frequency domain analysis, and the PSD trend is also close. Poincaré plot of non-linear analysis can visualize the response of BCG-derived HRV and ECG-derived HRV to RSA. By analyzing the results in the time domain, frequency domain, and nonlinearity, the proposed HRV monitoring system enables reliable heart health monitoring in the chair. In addition to high accuracy, the FOS-based BCG monitoring system also has the unique advantage of flexible configuration, contactless and accurate monitoring, long-term and continuous HR detection. In future work, by extending sensor width, the designed novel fiber-optic sensor can be placed under the mattress for long-term HRV monitoring during sleep. The proposed non-contact sensing system is convenient and accurate. It should also be noted that achieving the HRV information of the moving subjects is still a puzzle to be solved. In this case, wearable sensors are worthy of development.

Chapter 6

Conclusion and future works

6.1 Conclusion

This thesis proposes and fabricates a novel inline MZI sensor based on homemade SCF and SH-HiBiF for non-contact vital signs monitoring. Encapsulating FOS under a mattress allows for long-term monitoring of vital signs. Through filtering and FFT algorithms, accurate RR and HR can be obtained. Even without connecting the electrodes to the human body, the proposed system can diagnose premature beats with 97.9% accuracy, which is more comfortable for patients. Lower cost, simpler process, and higher accuracy make SCF-based vital sign detection systems highly competitive in the home healthcare field. The experiments of this work demonstrate the feasibility of FOS systems based on special optical fibers for further research in the biomedical field.

In order to collect accurate BCG signals stably and long-term for heart health analysis, this thesis proposes a low-cost and robust system based on FOS. The core part of the system is the MZI based on single-mode fiber, which consists of a 1×2 coupler and a 3×3 coupler. Due to the asymmetric structure of the two MZI arms, an interference spectrum will be observed, which will shift linearly with changes in lateral stress. Incident light is emitted from a low-cost DFB laser and coupled into the MZI sensor. Vibrations caused by human breathing and heartbeat will cause changes in the light phase in the MZI, which in turn will cause changes in the interference light intensity detected by the three PDs. FOS-based BCG-derived IBI showed a high correlation with ECG-derived IBI, with a correlation coefficient of 0.9971.

Based on the proposed system, we tried its application in different scenarios. In sleep status monitoring, the BCG system does not require uncomfortable patches on the body or wired connections on the body, so it can monitor sleep status in real-time without affecting sleep. The FOS-based BCG system shows a heart rate accuracy close to that of an electrocardiogram device and can be used as a reliable device for heart rate analysis. Furthermore, the proposed system can be placed on the wrist pulse for simultaneous monitoring of HR and RR. The HR calculation result is completely consistent with the reference PPG signal, and the error between the RR result and the reference signal is within 1 breath per minute. The proposed system can be equipped with dual FOS for extracting the driver's heartbeat in an environment that simulates car vibrations. Spectral subtraction processing of the signal can effectively eliminate the impact of vehicle vibrations such as simulated engines on the BCG signal, and significantly improve the accuracy of heartbeat extraction.

A BCG monitoring system based on the proposed 3×3 demodulation scheme was used to study cardiac responses after different exercises. The BCG HRV calculated from the demodulated signal can be used as a new accurate heart condition analysis signal. The BCG signal can be used to evaluate myocardial contractility through electrocardiographic analysis of the RJ interval, which is a practical alternative to PEP. Due to its non-contact measurement, FOS-based BCG will become an important part of heart disease analysis. HRV analysis provides insight into autonomic function. Many diseases, both cardiac and non-cardiac, are associated with changes in HRV. BCG-derived IBI showed a high correlation with ECG-derived IBI, with correlation coefficients of 0.9971 and 0.9581 for healthy subjects and premature subjects, respectively. During the one-month stability test, the FOS-based BCG monitoring system achieved high accuracy. Pace respiratory data at 0.1 Hz and 0.25 Hz were collected from 5 subjects of different ages, including one subject with premature beats. Studies have shown that breathing at 0.1 Hz results in larger RSA amplitudes, and resonant frequency breathing is observed in both BCG and ECG IBI signals. The amplitude of HRV decreased with age at both respiratory rates. This study also analyzed short-term HRV accuracy in 5 subjects based on FOS. The time-domain indices of BCG HRV and ECG HRV showed smaller errors via boxplots. A higher correlation coefficient is observed in the frequency domain analysis, and the PSD trend is also close. Poincaré plots from nonlinear analysis visualize BCG HRV and ECG HRV responses to RSA. By analyzing the results in the time domain, frequency domain, and nonlinearity, the proposed HRV monitoring system enables reliable heart health monitoring in a chair. In addition to high accuracy, the FOS-based BCG monitoring system also has unique advantages such as flexible configuration, non-contact precise monitoring, and long-term continuous HR detection. In future work, by extending the sensor width, the designed new fiber optic sensor can be placed under the mattress for long-term HRV monitoring during sleep. The proposed contactless sensing system is convenient and accurate. It should also be noted that obtaining HRV information of moving objects is still a difficult problem to be solved. In this case, wearable sensors are worthy of development.

6.2 Future works

Based on the monitoring system and current research results proposed in this article, more in-depth analysis of BCG signals can be performed in the future.

Hypertension is a common chronic disease that can lead to stroke, heart attack, heart failure, kidney damage, and many other health problems. It causes up to 7.6 million deaths worldwide each year [185]. Because accurate diagnosis of masked hypertension, white-coat hypertension, and nocturnal hypertension is challenging, implementation of effective hypertension care is critical to saving lives [186,187]. In terms of assessment and diagnosis, more widespread 24-hour ambulatory BP monitoring is needed [188]. Studies have found that 24-hour ambulatory BP monitoring is more meaningful than clinical one-time BP measurement in diagnosing various CVDs [189]. Most methods of measuring BP in non-clinical settings require a cuff to be worn on the upper arm. However, the inconvenience of this approach prevents many individuals from measuring their BP regularly.

The most common method of cuffless BP estimation is using ECG, PPG, or dual PPG signals. It is known that PTT and PWV calculated from the above signals are highly correlated with BP [188,189]. PTT measures the travel time of a pressure wave between two points in the arterial. It has attracted widespread attention because of its potential for convenient and universal BP monitoring. Compared with currently widely used BP measurement techniques (e.g. auscultation and oscillometric methods), PTT can achieve cuff-less BP monitoring [191].

BCG is a measurement of the body's reaction to the heart's effort to pump blood into the aorta. Since the time interval between R peaks of ECG and J peaks of BCG has been shown to be closely related to PEP [127], we believe that BCG serves as a reliable and convenient proximal timing reference for obtaining PTT measurements. Our future work will focus on continuous BP monitoring based on BCG.

Bibliography

[1] F. Zhang, Y. Yu, and J. Zhong, “Research Status and Development Prospects of Human Vital Signs Monitoring Clothing,” 2018 International Conference on Construction, Aviation and Environment Engineering, vol. 233, no. 4, pp. 42031–, 2019.

[2] C. W. Tsao et al., “Heart Disease and Stroke Statistics-2022 Update: A Report From the American Heart Association,” Circulation (New York, N.Y.), vol. 145, no. 8, pp. E153–E639, 2022.

[3] G. Finocchiaro, N. Sheikh, E. Biagini, M. Papadakis, G. Sinagra, A. Pelliccia, C. Rapezzi, S. Sharma, I. Olivotto, “The Electrocardiogram in the Diagnosis and Management of Patients with Hypertrophic Cardiomyopathy,” Heart Rhythm, vol. 17, no. 1, pp. 142–151, 2020.

[4] H. Liu, J. Allen, D. Zheng, and F. Chen, “Recent Development of Respiratory Rate Measurement Technologies,” Physiological Measurement, vol. 40, no. 7, pp. 07-TR01, 2019.

[5] J. Alametsä et al., “Automatic Detection of Spiking Events in EMFi Sheet During Sleep,” Medical Engineering & Physics, vol. 28, no. 3, pp. 267–275, 2006.

[6] R. M. Wiard, O. T. Inan, B. Argyres, M. Etemadi, G. T. A. Kovacs, and L. Giovangrandi, “Automatic Detection of Motion Artifacts in the Ballistocardiogram Measured on a Modified Bathroom Scale,”

Medical & Biological Engineering & Computing, vol. 49, no. 2, pp. 213–220, 2011.

[7] M. A. Hassan, A. S. Malik, D. Fofi, N. M. Saad, Y. S. Ali, and F. Meriaudeau, “Video-Based Heartbeat Rate Measuring Method Using Ballistocardiography,” IEEE Sensors Journal, vol. 17, no. 14, pp. 4544–4557, 2017.

[8] D. Cimr and F. Studnička, “Automatic Detection of Breathing Disorder from Ballistocardiography Signals,” Knowledge-based Systems, vol. 188, pp. 104973-, 2020.

[9] C. Lu, J. Su, X. Dong, T. Sun, and K. T. V. Grattan, “Simultaneous Measurement of Strain and Temperature With a Few-Mode Fiber-Based Sensor,” Journal of Lightwave Technology, vol. 36, no. 13, pp. 2796–2802, 2018.

[10] S. Akita, H. Sasaki, K. Watanabe, and A. Seki, “A Humidity Sensor Based on a Hetero-core Optical Fiber,” Sensors and Actuators. B, Chemical, vol. 147, no. 2, pp. 385–391, 2010.

[11] H. Sun, S. Yang, X. Zhang, L. Yuan, Z. Yang, and M. Hu, “Simultaneous Measurement of Temperature and Strain or Temperature and Curvature Based on An Optical Fiber Mach–Zehnder Interferometer,” Optics Communications, vol. 340, pp. 39–43, 2015.

[12] X. Wu, X. Wang, S. Li, S. Huang, Q. Ge, and B. Yu, “Cantilever Fiber-Optic Accelerometer Based on Modal Interferometer,” IEEE

Photonics Technology Letters, vol. 27, no. 15, pp. 1632–1635, 2015.

[13] H. Z. Yang, M. M. Ali, Md. R. Islam, K.-S. Lim, D. S. Gunawardena, and H. Ahmad, “Cladless Few Mode Fiber Grating Sensor for Simultaneous Refractive Index and Temperature Measurement,” Sensors and Actuators A: Physical, vol. 228, pp. 62–68, 2015.

[14] X. Yang, Z. Chen, C. S. M. Elvin, L. H. Y. Janice, S. H. Ng, J. T. Teo and R. Wu, “Textile Fiber Optic Microbend Sensor Used for Heartbeat and Respiration Monitoring,” IEEE Sensor Journal, vol. 15, no. 2, pp. 757-761, 2015.

[15] Ł. Dziuda, M. Krej, and F. W. Skibniewski, “Fiber Bragg Grating Strain Sensor Incorporated to Monitor Patient Vital Signs During MRI,” IEEE Sensors Journal, vol. 13, no. 12, pp. 4986–4991, 2013.

[16] R. G. Priest, “Analysis of Fiber Interferometer Utilizing 3 x 3 Fiber Coupler,” IEEE Transactions on Microwave Theory and Techniques, vol. 30, no. 10, pp. 1589–1591, 1982.

[17] D. A. Jackson, R. Priest, A. Dandridge, and A. B. Tveten, “Elimination of Drift in a Single-mode Optical Fiber Interferometer Using a Piezoelectrically Stretched Coiled Fiber,” Applied Optics, vol. 19, no. 17, pp. 2926–2929, 1980.

[18] I. Starr, A. J. Rawson, H. A. Schroeder, and N. R. Joseph, “Studies on the Estimation of Cardiac Output in Man, and of Abnormalities in Cardiac Function, from the Heart’s Recoil and the Blood’s

Impacts; the Ballistocardiogram," American Journal of Physiology-Legacy Conten, vol. 127, pp. 1–28, 1939.

[19] J. W. Gordon, "Certain Molar Movements of the Human Body Produced by the Circulation of the Blood," Journal of Anatomy and Physiology, vol. 11, no. Pt3, pp. 533–536, 1877.

[20] C. S. Kim, S. L. Ober, M. S. Mcmurtry, B. A. Finegan, O. T. Inan, R. Mukkamala, and J. O. Hahn, "Ballistocardiogram: Mechanism and Potential for Unobtrusive Cardiovascular Health Monitoring," Scientific Reports, vol. 6, no. 1, pp. 31297–31297, 2016.

[21] J. Williams, "Bridge Circuits: Marrying Gain and Balance," Linear Technology Application, vol. 43, pp. 1-46, 1990.

[22] O. T. Inan, M. Etemadi, R. M. Wiard, L. Giovangrandi, and G. T. A. Kovacs, "Robust Ballistocardiogram Acquisition for Home Monitoring," Physiological Measurement, vol. 30, no. 2, pp. 169, 2009.

[23] R. González-Landaeta, O. Casas, and R. Pallàs-Areny, "Heart Rate Detection from An Electronic Weighing Scale," Physiological Measurement, vol. 29, no. 8, pp. 979–988, 2008.

[24] J. H. Shin, K. M. Lee, and K. S. Park, "Non-constrained Monitoring of Systolic Blood Pressure on A Weighing Scale," Physiological Measurement, vol. 30, no. 7, pp. 679–693, 2009.

[25] J. Alihanka, K. Vaahtoranta, and I. Saarikivi, "A New Method for Long-term Monitoring of the Ballistocardiogram, Heart Rate, and Respiration," American Journal of Physiology, Regulatory,

Integrative and Comparative Physiology, vol. 240, no. 5, pp. 384-R392, 1981.

[26] A. Vehkaoja, S. Rajala, P. Kumpulainen, and J. Lekkala, “Correlation Approach for the Detection of the Heartbeat Intervals Using Force Sensors Placed under the Bed Posts,” Journal of Medical Engineering & Technology, vol. 37, no. 5, pp. 327–333, 2013.

[27] J. M. Kortelainen and J. Virkkala, “FFT Averaging of Multichannel BCG Signals from Bed Mattress Sensor to Improve Estimation of Heart Beat Interval,” in 2007 29th Annual International Conference of the IEEE Engineering in Medicine and Biology Society, pp. 6685-6688, 2007.

[28] J. Paalasmaa, M. Waris, H. Toivonen, L. Leppakorpi, and M. Partinen, “Unobtrusive Online Monitoring of Sleep at Home,” in 2012 Annual International Conference of the IEEE Engineering in Medicine and Biology Society, pp. 3784-3788, 2012.

[29] F. Wang, M. Tanaka, and S. Chonan, “Development of a PVDF Piezopolymer Sensor for Unconstrained In-Sleep Cardiorespiratory Monitoring,” Journal of Intelligent Material Systems and Structures, vol. 14, no. 3, pp. 185–190, 2003.

[30] X. Zhu, W. Chen, T. Nemoto, Y. Kanemitsu, K. Kitamura, K. Yamakoshi, and D. Wei, “Real-Time Monitoring of Respiration Rhythm and Pulse Rate During Sleep,” IEEE Transactions on Biomedical Engineering, vol. 53, no. 12, pp. 2553–2563, 2006.

[31] J. Kortelainen, M. V. Gils, and J. Parkka, “Multichannel Bed Pressure Sensor for Sleep Monitoring,” in 2012 Computing in Cardiology, pp. 313-316, 2012.

[32] M. Walter, B. Eilebrecht, T. Wartzek, and S. Leonhardt, “The Smart Car Seat: Personalized Monitoring of Vital Signs in Automotive Applications,” Personal and Ubiquitous Computing, vol. 15, no. 7, pp. 707–715, 2011.

[33] J. Alametsä, J. Viik, J. Alakare, A. Värri, and A. Palomäki, “Ballistocardiography in Sitting and Horizontal Positions,” Physiological Measurement, vol. 29, no. 9, pp. 1071, 2008.

[34] I. Starr, A. J. Rawson and H. A. Schroeder, "Studies on the Estimation of Cardiac Output in Man and of Abnormalities in Cardiac Function from the Hearts Recoil and the Bloods Impacts; the Ballistocardiogram", The American Journal of Physiology, vol. 127, no. 1, pp. 1-28, 1939.

[35] I. Starr and F. C. Wood, "Studies with the Ballistocardiograph in Acute Cardiac Infarction and Chronic Angina Pectoris", American Heart Journal, vol. 25, no. 1, pp. 81-101, 1943.

[36] O. T. Inan, M. Etemadi and R. M. Wiard, "Robust Ballistocardiogram Acquisition for Home Monitoring", Physiological Measurement, vol. 30, no. 2, pp. 169-185, 2009.

[37] D. D. He, E. S. Winokur and C. G. Sodini, "A Continuous Wearable and Wireless Heart Monitor Using Head Ballistocardiogram (BCG) and Head Electrocardiogram (ECG)", in

2011 Annual International Conference of the IEEE Engineering in Medicine and Biology Society, pp. 4729-4732, 2011.

[38] M. Etemadi, O. T. Inan, L. Giovangrandi, and G. T. A. Kovacs, “Rapid Assessment of Cardiac Contractility on a Home Bathroom Scale,” IEEE Transactions on Information Technology in Biomedicine, vol. 15, no. 6, pp. 864–869, 2011.

[39] O. T. Inan, M. Etemadi and A. Paloma, "Non-invasive Cardiac Output Trending During Exercise Recovery on a Bathroom-scale-based Ballistocardiograph", Physiological Measurement, vol. 30, no. 3, pp. 261-274, 2009.

[40] E. Pinheiro, O. Postolache and P. Girao, "Pulse Arrival Time and Ballistocardiogram Application to Blood Pressure Variability Estimation", in 2009 IEEE International Workshop on Medical Measurements and Applications, New York: IEEE, pp. 132-136, 2009.

[41] J. H. Shin, K. M. Lee and K. S. Park, "Non-constrained Monitoring of Systolic Blood Pressure on a Weighing Scale", Physiological Measurement, vol. 30, no. 7, pp. 679–693, 2009

[42] R. Casanella, J. Gomez-Clapers and R. Pallas-Areny, "On Time Interval Measurements Using BCG", in 2012 Annual International Conference of the IEEE Engineering in Medicine and Biology Society, pp. 5034-5037, 2012.

[43] E. S. Winokur, D. D. He and C. G. Sodini, "A Wearable Vital Signs Monitor at the Ear for Continuous Heart Rate and Pulse

Transit Time Measurements", 2012 Annual International Conference of the IEEE Engineering in Medicine and Biology Society, pp. 2724–2727, 2012.

[44] A. Q. Javaid, H. Ashouri, and O. T. Inan, “Estimating Systolic Time Intervals during Walking Using Wearable Ballistocardiography,” in 2016 IEEE-EMBS International Conference on Biomedical and Health Informatics (BHI), pp. 549–55, 2016.

[45] K. C. Kao and G. A. Hockham, "Dielectric-fibre Surface Waveguides for Optical Frequencies," Proceedings of the Institution of Electrical Engineers, vol, 113, no. 7, pp. 1151-1158, 1966.

[46] N. Bai, E. Ip, Y.-K. Huang, E. Mateo, F. Yaman, M.-J. Li, S. Bickham, S. Ten, J. Liñares, C. Montero, V. Moreno, X. Prieto, V. Tse, K. Man Chung, A. P. T. Lau, H.-Y. Tam, C. Lu, Y. Luo, G.-D. Peng, G. Li, and T. Wang, "Mode-division Multiplexed Transmission with Inline Few-mode Fiber Amplifier," Optics Express, vol. 20, no. 3, pp. 2668-2680, 2012.

[47] A. Mecozzi, C. Antonelli, and M. Shtaif, “Nonlinear Propagation in Multi-mode Fibers in the Strong Coupling Regime,” Optics Express, vol. 20, no. 11, pp. 11673–11678, 2012.

[48] S. Inao, T. Sato, S. Sentsui, T. Kuroha, and Y. Nishimura, “Multicore optical fiber,” in Optical Fiber Communication Conference (OFC), WB1, 1979.

[49] T. A. Birks, J. C. Knight, and P. S. Russell, “Endlessly Single-Mode Photonic Crystal Fiber,” Optics Letters, vol. 22, no. 13, pp. 961-, 1997.

[50] N. Zeng, C. Z. Shi, M. Zhang, L. W. Wang, Y. B. Liao, and S. R. Lai, “A 3-component Fiber-optic Accelerometer for Well Logging,” Optics Communications, vol. 234, no. 1, pp. 153–162, 2004.

[51] S. Šprager, D. Donlagić, and D. Zazula, “Monitoring of Basic Human Vital Functions Using Optical Interferometer,” in IEEE 10th International Conference Signal Processing Proceedings, 1738-1741, 2010.

[52] J. M. López-Higuera and L. R. Cobo, A. Q. Incera, and A. Cobo, “Fiber Optic Sensors in Structural Health Monitoring,” Journal of Lightwave Technology, vol. 29, no. 4, pp. 587–608, 2011.

[53] L. Duan, P. Zhang, M. Tang, R. Wang, Z. Zhao, S. Fu, L. Gan, B. Zhu, W. Tong, D. Liu, and P. P. Shum, “Heterogeneous All-solid Multicore Fiber Based Multipath Michelson Interferometer for High Temperature Sensing,” Optics Express, vol. 24, no. 18, pp. 20210–20218, 2016.

[54] L. Dziuda, M. Krej, and F. W. Skibniewski, “Fiber Bragg Grating Strain Sensor Incorporated to Monitor Patient Vital Signs During MRI,” IEEE Sensors Journal, vol. 13, no. 12, pp. 4986–4991, 2013.

[55] S. K. Yao and C. K. Asawa, “Fiber Optical Intensity Sensors”, IEEE Journal on Selected Areas in Communications, vol. 1, no. 3, pp. 562-575, 1983.

[56] N. Lagakos, J. H. Cole, and J. A. Bucaro, “Microbend Fiber-optic Sensor,” Applied optics, vol. 26, no. 11, pp. 2171-2180, 1987.

[57] H. Golnabi, “Design and Operation of a Fiber Optic Sensor for Liquid Level Detection,” Optics and Lasers in Engineering, vol. 41, no. 5, pp. 801–812, 2004.

[58] R. Suresh, S. C. Tjin, and J. Hao, “Fiber Bragg Grating,” Smart Materials in Structural Health Monitoring, pp. 413-439, 2012.

[59] I. L. Bundalo, K. Nielsen, G. Woyessa, and O. Bang, "Long-term Strain Response of Polymer Optical Fiber FBG Sensors," Optical Materials Express, vol. 7, no. 3, pp. 967-976, 2017.

[60] J. Jung, H. Nam, B. Lee, J. O. Byun, and N. S. Kim, “Fiber Bragg Grating Temperature Sensor with Controllable Sensitivity,” Applied Optics, vol. 38, no. 13, pp.2752-2754, 1999.

[61] C. H. Yeh, Y. H. Zhuang, N. Tsai, and C. W. Chow, “Capacity and Capability Enhancements of FBG Sensor System by Utilizing Intensity and WDM Detection Technique," Smart Materials and Structures, vol. 26, no. 3, 2017.

[62] M. J. Schmid, M. S. Müller, and A. W. Koch, "Fiber Bragg Grating Measurement Technology in Industry," 17th International Conference on Sensors and Measurement Technology, vol. 19, no.21, pp. 5, 2015.

[63] P. Lu, K. Byerly, M. Buric, P. Zandhuis, and P. R. Ohodnicki, “Distributed Fiber-optic Sensor for Real-time Monitoring of

Energized Transformer Cores," International Society for Optics and Photonics, vol. 10194, pp. 101941S, 2017.

[64] M. Imai, T. Ohashi, and Y. Ohtsuka, "Fiber-optic Michelson Interferometer Using an Optical Power Divider," Optics Letters, vol. 5, no. 10, pp. 418–420, 1980.

[65] G. B. Hocker, "Fiber-optic Sensing of Pressure and Temperature," Applied Optics, vol. 18, no. 9, pp. 1445–1448, 1979.

[66] T. Yoshino, K. Kurosawa, K. Itoh, and T. Ose, "Fiber-Optic Fabry-Perot Interferometer and Its Sensor Applications," IEEE Journal of Quantum Electronics, vol. 18, no. 10, pp. 1624–1633, 1982.

[67] A. Y. Chang, V. F. Skirbekk, S. Tyrovolas, N. J. Kassebaum, and J. L. Dieleman, "Measuring Population Ageing: an Analysis of the Global Burden of Disease Study 2017," The Lancet Public Health, vol. 4, no. 3, pp. e159–e167, 2019.

[68] J. J. DiNicolantonio, J. H. O'Keefe, and W. Wilson, "Subclinical Magnesium Deficiency: A Principal Driver of Cardiovascular Disease and A Public Health Crisis," Open heart, vol. 5, no. 1, pp. e000668–e000668, 2018.

[69] P. Bjerregaard, "Premature Beats in Healthy Subjects 40–79 Years of Age," European Heart Journal, vol. 3, no. 6, pp. 493–503, 1982.

[70] C. Gimpel, C. Bergmann, D. Bockenhauer, L. Breysem, M. A. Cadnapaphornchai, M. Cetiner, J. Dudley, F. Emma, M. Konrad, T. Harris, et al., "International Consensus Statement on the Diagnosis and Management of Autosomal Dominant Polycystic Kidney

Disease in Children and Young People," Nature Reviews Nephrology, vol. 15, no. 11, pp. 713–726, 2019.

[71] E. E. De Roeck, P. P. De Deyn, E. Dierckx, and S. Engelborghs, "Brief Cognitive Screening Instruments for Early Detection of Alzheimer's Disease: A Systematic Review," Alzheimer's Research & Therapy, vol. 11, no. 1, pp. 1–14, 2019.

[72] K. Wilson and J. S. Brownstein, "Early Detection of Disease Outbreaks Using the Internet," Canadian Medical Association journal (CMAJ), vol. 180, no. 8, pp. 829–831, 2009.

[73] M. M. Wagner, F.-C. Tsui, J. U. Espino, V. M. Dato, D. F. Sittig, R. A. Caruana, L. F. McGinnis, D. W. Deerfield, M. J. Druzdzel, and D. B. Fridsma, "The Emerging Science of Very Early Detection of Disease Outbreaks," Journal of Public Health Management and Practice, vol. 7, no. 6, pp. 51–59, 2001.

[74] N. Sarrafzadegan and N. Mohammmadifard, "Cardiovascular Disease in Iran in the Last 40 Years: Prevalence, Mortality, Morbidity, Challenges and Strategies for Cardiovascular Prevention," Archives of Iranian Medicine, vol. 22, no. 4, pp. 204–210, 2019.

[75] C. C. Young, R. H. Bonow, G. Barros, M. Mossa-Basha, L. J. Kim, and M. R. Levitt, "Magnetic Resonance Vessel Wall Imaging in Cerebrovascular Diseases," Neurosurgical Focus, vol. 47, no. 6, pp. E4, 2019.

[76] R. Basatneh, B. Najafi, and D. G. Armstrong, “Health Sensors, Smart Home Devices, and the Internet of Medical Things: An Opportunity for Dramatic Improvement in Care for the Lower Extremity Complications of Diabetes,” Journal of Diabetes Science and Technology, vol. 12, no. 3, pp. 577–586, 2018.

[77] O. V. Bitkina, H. K. Kim, and J. Park, “Usability and User Experience of Medical Devices: An Overview of the Current State, Analysis Methodologies, and Future Challenges,” International Journal of Industrial Ergonomics, vol. 76, pp. 102932, 2020.

[78] D. Dias and J. Paulo Silva Cunha, “Wearable Health Devices—Vital Sign Monitoring, Systems and Technologies,” Sensors, vol. 18, no. 8, pp. 2414, 2018.

[79] E. J. Benjamin, P. Muntner, A. Alonso, M. S. Bittencourt, C. W. Callaway, A. P. Carson, A. M. Chamberlain, A. R. Chang, S. Cheng, S. R. Das, et al., “Heart Disease and Stroke Statistics—2019 Update: A Report from the American Heart Association,” Circulation, vol. 139, no. 10, pp. e56–e528, 2019.

[80] F. Tan, S. Chen, W. Lyu, Z. Liu, C. Yu, C. Lu, and H.-Y. Tam, “Non-invasive Human Vital Signs Monitoring Based on Twin-core Optical Fiber Sensors,” Biomedical Optics Express, vol. 10, no. 11, pp. 5940–5952, 2019.

[81] Z. C. Haberman, R. T. Jahn, R. Bose, H. Tun, J. S. Shinbane, R. N. Doshi, P. M. Chang, and L. A. Saxon, “Wireless Smartphone ECG Enables Large-scale Screening in Diverse Populations,” Journal of

Cardiovascular Electrophysiology, vol. 26, no. 5, pp. 520–526, 2015.

[82] J. Liu, Y. Chen, Y. Wang, X. Chen, J. Cheng, and J. Yang, “Monitoring Vital Signs and Postures During Sleep Using Wifi Signals,” IEEE Internet of Things Journal, vol. 5, no. 3, pp. 2071–2084, 2018.

[83] M. Nosrati, S. Shahsavari, S. Lee, H. Wang, and N. Tavassolian, “A Con-current Dual-beam Phased-array Doppler Radar Using Mimo Beamforming Techniques for Short-range Vital-signs Monitoring,” IEEE Transactions on Antennas and Propagation, vol. 67, no. 4, pp. 2390–2404, 2019.

[84] N. Wadhwa, J. G. Chen, J. B. Sellon, D. Wei, M. Rubinstein, “Motion Microscopy for Visualizing and Quantifying Small Motions,” Proceedings of the National Academy of Sciences, vol. 114, no. 44, pp. 11639–11644, 2017.

[85] Z. Fang, K. Chin, R. Qu, and H. Cai, Fundamentals of optical fiber sensors, vol. 226. John Wiley & Sons, 2012.

[86] J. Amorebieta, A. Ortega-Gomez, G. Durana, R. Fernández, E. Antonio-Lopez, A. Schülzgen, J. Zubia, R. Amezcua-Correa, and J. Villatoro, “Compact Omnidirectional Multicore Fiber-based Vector Bending Sensor,” Scientific Reports, vol. 11, no. 1, pp. 1–11, 2021.

[87] A. Van Newkirk, J. Antonio-Lopez, A. Velazquez-Benitez, J. Albert, R. Amezcua-Correa, and A. Schülzgen, “Bending Sensor

Combining Multicore Fiber with A Mode-selective Photonic Lantern,” Optics Letters, vol. 40, no. 22, pp. 5188–5191, 2015.

[88] D. A. May-Arrioja and J. R. Guzman-Sepulveda, “Highly Sensitive Fiber Optic Refractive Index Sensor Using Multicore Coupled Structures,” Journal of Lightwave Technology, vol. 35, no. 13, pp. 2695–2701, 2017.

[89] D. Varshneya and J. L. Maida Jr, “Fiber Optic Monitor Using Interferometry for Detecting Vital Signs of A Patient,” Dec. 24, 2002. US Patent 6,498,652.

[90] D. Varshneya, J. L. Maida Jr, and L. A. Jeffers, “Fiber Optic Interferometric Vital Sign Monitor for Use in Magnetic Resonance Imaging, Confined Care Facilities and In-hospital,” Nov. 9, 2004. US Patent 6,816,266.

[91] S. ˇSprager and D. Zazula, “Heartbeat and Respiration Detection from Optical Interferometric Signals by Using a Multimethod Approach,” IEEE Transactions on Biomedical Engineering, vol. 59, no. 10, pp. 2922–2929, 2012.

[92] X. Yang, Z. Chen, C. S. M. Elvin, L. H. Y. Janice, S. H. Ng, J. T. Teo, and R. Wu, “Textile Fiber Optic Microbend Sensor Used for Heartbeat and Respiration Monitoring,” IEEE Sensors Journal, vol. 15, no. 2, pp. 757–761, 2014.

[93] S. Chen, Z. Huang, F. Tan, T. Yang, J. Tu, and C. Yu, “Vital Signs Monitoring Using Few-mode Fiber-based Sensors,” in

Optoelectronic Devices and Integration VII, vol. 10814, pp. 108140P, International Society for Optics and Photonics, 2018.

[94] J. Villatoro, O. Arrizabalaga, G. Durana, I. Saez de Ocariz, E. Antonio-Lopez, J. Zubia, A. Schülzgen, and R. Amezcua-Correa, “Accurate Strain Sensing Based on Super-mode Interference in Strongly Coupled Multi-core Optical Fibres,” Scientific Reports, vol. 7, no. 1, pp. 1–7, 2017.

[95] J. A. Flores-Bravo, R. Fernández, E. A. Lopez, J. Zubia, A. Schülzgen, R. A. Correa, and J. Villatoro, “Simultaneous Sensing of Refractive Index and Temperature with Supermode Interference,” Journal of Lightwave Technology, vol. 39, no. 22, pp. 7351–7357, 2021.

[96] Z. Liu, D. Zheng, J. Madrigal, J. Villatoro, J. E. Antonio-Lopez, A. Schülzgen, R. Amezcua-Correa, X. Zou, W. Pan, and S. Sales, “Temperature-Insensitive Curvature Sensor Based on Bragg Gratings Written in Strongly Coupled Multicore Fiber,” Optics Letters, vol. 46, no. 16, pp. 3933–3936, 2021.

[97] J. Villatoro, A. Van Newkirk, E. Antonio-Lopez, J. Zubia, A. Schülzgen, and R. Amezcua-Correa, “Ultrasensitive Vector Bending Sensor Based on Multicore Optical Fiber,” Optics Letters, vol. 41, no. 4, pp. 832–835, 2016.

[98] J. Villatoro, E. Antonio-Lopez, A. Schülzgen, and R. Amezcua-Correa, “Miniature Multicore Optical Fiber Vibration Sensor,” Optics Letters, vol. 42, no. 10, pp. 2022–2025, 2017.

[99] D. May-Arrioja and J. Guzman-Sepulveda, “Fiber Optic Sensors Based on Multicore Structures,” Fiber Optic Sensors, pp. 347–371, 2017.

[100] J. Amorebieta, G. Durana, A. Ortega-Gomez, R. Fernández, J. Velasco, et al., “Packaged Multi-core Fiber Interferometer for High-Temperature Sensing,” Journal of Lightwave Technology, vol. 37, no. 10, pp. 2328–2334, 2019.

[101] M. C. Alonso-Murias, D. Monzón-Hernández, O. Rodríguez-Quiroz, J. E. Antonio-Lopez, A. Schülzgen, R. Amezcua-Correa, and J. Villatoro, “Long-range Multicore Optical Fiber Displacement Sensor,” Optics Letters, vol. 46, no. 9, pp. 2224–2227, 2021.

[102] A. Van Newkirk, E. Antonio-Lopez, G. Salceda-Delgado, R. Amezcua-Correa, and A. Schülzgen, “Optimization of Multicore Fiber for High-temperature Sensing,” Optics Letters, vol. 39, no. 16, pp. 4812–4815, 2014.

[103] F. Poletti, “Nested Antiresonant Dodeless Hollow Core Fiber,” Optics Express, vol. 22, no. 20, pp. 23807–23828, 2014.

[104] J. H. Shin, S. H. Hwang, M. H. Chang, and K. S. Park, “Heart Rate Variability Analysis Using a Ballistocardiogram During Valsalva Manoeuvre and Post Exercise,” Physiological Measurement, vol. 32, no. 8, p. 1239, 2011.

[105] R. González-Camarena, S. Carrasco-Sosa, R. Roman-Ramos, M. J. Gaitan-Gonzalez, V. Medina-Bañuelos, and J. Azpiroz-Leehan,

"Effect of Static and Dynamic Exercise on Heart Rate and Blood Pressure Variabilities," Medicine and Science in Sports and Exercise, vol. 32, no. 10, pp. 1719–1728, 2000.

[106] N. Giardino, P. Lehrer, and R. Edelberg, "Comparison of Finger Plethysmograph to ECG in the Measurement of Heart Rate Variability," Psychophysiology, vol. 39, no. 2, pp. 246–253, 2002.

[107] D. Biswas, N. Simoes-Capela, C. Van Hoof, and N. Van Helleputte, "Heart Rate Estimation from Wrist-Worn Photoplethysmography: A Review," IEEE Sensors Journal, vol. 19, no. 16, pp. 6560–6570, 2019.

[108] C. L. Levkov, "Orthogonal Electrocardiogram Derived from the Limb and Chest Electrodes of the Conventional 12-lead System," Medical & Biological Engineering & Computing, vol. 25, no. 2, pp. 155–164, 1987.

[109] C. Massaroni et al., "Validation of a Wearable Device and an Algorithm for Respiratory Monitoring During Exercise," IEEE Sensors Journal, vol. 19, no. 12, pp. 4652–4659, 2019.

[110] D. L. Presti et al., "Smart Textile Based on 12 Fiber Bragg Gratings Array for Vital Signs Monitoring," IEEE Sensors Journal, vol. 17, no. 18, pp. 6037–6043, 2017.

[111] W. Xu, Y. Shen, C. Yu, B. Dong, W. Zhao, and Y. Wang, "Long Modal Interference in Multimode Fiber and Its Application in Vital Signs Monitoring," Optics Communications, vol. 474, pp. 126100-, 202.

[112] Y.-C. Yeh, C. W. Chiou, and H.-J. Lin, “Analyzing ECG for Cardiac Arrhythmia Using Cluster Analysis,” Expert Systems with Applications, vol. 39, no. 1, pp. 1000–1010, 2012.

[113] P. Manimegalai, D. Jacob, and K. Thanushkodi, “Estimation of Cardiovascular Parameters from ECG and PPG Signals,” in 2012 38th Annual Northeast Bioengineering Conference (NEBEC), 2012, pp. 237–238.

[114] M. Folke, L. Cernerud, M. Ekström, and B. Hök, “Critical Review of Non-invasive Respiratory Monitoring in Medical Care,” Medical & Biological Engineering & Computing, vol. 41, no. 4, pp. 377–383, 2003.

[115] Z. Zhao, M. S. Demokan, and M. MacAlpine, “Improved Demodulation Scheme for Fiber Optic Interferometers Using an Asymmetric 3×3 coupler,” Journal of Lightwave Technology, vol. 15, no. 11, pp. 2059–2068, 1997.

[116] S. Chen, F. Tan, W. Lyu, and C. Yu, “Ballistocardiography Monitoring System Based on Optical Fiber Interferometer Aided with Heartbeat Segmentation Algorithm,” Biomedical Optics Express, vol. 11, no. 10, pp. 5458-5469, 2020.

[117] J. Gomez-Clapers, A. Serra-Rocamora, R. Casanella, and R. Pallas-Areny, “ Towards the Standardization of Ballistocardiography Systems for J-peak Timing Measurement,” Measurement, vol. 58, pp. 310-316, 2014.

[118] J. Q. Wang, C. X. Zheng, X. J. Jin, G. H. Lu, and A. S. Ni, “Study on A Non-contact Life Parameter Detection System Using Millimeter Wave,” Journal of Space Medicine & Medical Engineering of China, vol. 17, pp. 157–161, 2004.

[119] D. Shao, F. Tsow, C. Liu, Y. Yang, and N. Tao, “Simultaneous Monitoring of Ballistocardiogram and Photoplethysmogram Using a Camera,” IEEE Transactions on Biomedical Engineering, vol. 64, no. 5, pp. 1003-1010, 2016.

[120] M. Irwin, “Effects of Sleep and Sleep Loss on Immunity and Cytokines,” Brain, Behavior, and Immunity, vol. 16, no. 5, pp. 503–512, 2002.

[121] F. Lopez-Jimenez, F. H. Sert Kuniyoshi, A. Gami, and V. K. Somers, “Obstructive Sleep Apnea: Implications for Cardiac and Vascular Disease,” Chest, vol. 133, no. 3, pp. 793–804, 2008.

[122] J.-J. Shu and Y. Sun, “Developing Classification Indices for Chinese Pulse Diagnosis,” Complementary Therapies in Medicine, vol. 15, no. 3, pp. 190–198, 2006.

[123] J. Lin et al., “Wearable Sensors and Devices for Real-time Cardiovascular Disease Monitoring,” Cell Reports Physical Science, vol. 2, no. 8, p. 100541–, 2021.

[124] R. Kusche, P. Klimach, and M. Ryschka, “A Multichannel Real-Time Bioimpedance Measurement Device for Pulse Wave Analysis,” IEEE Transactions on Biomedical Circuits and Systems, vol. 12, no. 3, pp. 614–622, 2018.

[125] Y. Fu and J. Liu, “System Design for Wearable Blood Oxygen Saturation and Pulse Measurement Device,” Procedia Manufacturing, vol. 3, pp. 1187–1194, 201.

[126] W. Lyu, F. Tan, S. Chen, and C. Yu, “Myocardial Contractility Assessment Using Fiber Optic Sensors,” in Asia Communications and Photonics Conference (ACP), Paper M4A.152, pp. 1-3, 2019.

[127] W. Lyu, W. Xu, F. Yang, S. Chen, F. Tan, and C. Yu, “Non-Invasive Measurement for Cardiac Variations Using A Fiber Optic Sensor,” IEEE Photonics Technology Letters, vol. 33, no. 18, pp. 990–993, 2021.

[128] P. Palatini and S. Julius, “Heart Rate and the Cardiovascular Risk,” Journal of Hypertension, vol. 15, no. 1, pp. 3–17, 1997.

[129] C. P. Subbe, R. G. Davies, E. Williams, P. Rutherford, and L. Gemmell, “Effect of Introducing the Modified Early Warning Score on Clinical Outcomes, Cardio-pulmonary Arrests and Intensive Care Utilisation in Acute Medical Admissions,” Anaesthesia, vol. 58, no. 8, pp. 797–802, 2003.

[130] Y. Wang, J. Ma, and L. Wei, “Investigating the Effect of Long Trip on Driving Performance, Eye Blinks, and Awareness of Sleepiness Among Commercial Drivers: A Naturalistic Driving Test Study,” Scientia Iranica, vol. 26, no. 1, pp. 95–102, 2019.

[131] J. A. Healey and R. W. Picard, “Detecting Stress During Real-world Driving Tasks Using Physiological Sensors,” IEEE

Transactions on Intelligent Transportation Systems, vol. 6, no. 2, pp. 156–166, 2005.

[132] B. Hariri, S. Abtahi, S. Shirmohammadi, and L. Martel, “Demo: Vision Based Smart In-car Camera System for Driver Yawning Detection,” in 2011 5th ACM/IEEE International Conference on Distributed Smart Cameras, ICDSC 2011, 2011, pp. 1–2.

[133] A. Kolli, A. Fasih, F. Al Machot, and K. Kyamakya, “Non-intrusive Car Driver’s Emotion Recognition Using Thermal Camera,” in Proceedings of the Joint 3rd International Workshop on Nonlinear Dynamics and Synchronization, INDS’11 and 16th International Symposium on Theoretical Electrical Engineering, ISTET’11, 2011, pp. 1–5.

[134] S. Begum, "Intelligent Driver Monitoring Systems Based on Physiological Sensor Signals: A Review", In Proceedings of the 16th International IEEE Annual Conference on Intelligent Transportation Systems (ITSC), pp. 282-289, The Hague, The Netherlands, 6–9 October 2013.

[135] J. W. Gordon, "Certain Molar Movements of the Human Body Produced by the Circulation of the Blood", Journal of Anatomy and Physiology, vol. 11, pp. 533-536, 1877.

[136] J. Scheunemann, A. Unni, K. Ihme, M. Jipp, and J. W. Rieger, “Demonstrating Brain-Level Interactions Between Visuospatial Attentional Demands and Working Memory Load While Driving

Using Functional Near-Infrared Spectroscopy,” Frontiers in Human Neuroscience, vol. 12, pp. 542–542, 2019.

[137] W. T. Abraham et al., “Wireless Pulmonary Artery Haemodynamic Monitoring in Chronic Heart Failure: A Randomised Controlled Trial”, The Lancet (British edition), vol. 377, no. 9766, pp. 658–666, 2011.

[138] A. L. Bui, and G. C. Fonarow, "Home Monitoring for Heart Failure Management," Journal of the American College of Cardiology, vol. 59, no. 2, pp. 97-104, 2012.

[139] F. U. S. Mattace-Raso et al., “Determinants of Pulse Wave Velocity in Healthy People and in the Presence of Cardiovascular Risk Factors: ‘Establishing Normal and Reference Values,’” European Heart Journal, vol. 31, no. 19, pp. 2338–2350, 2010.

[140] T. Willum-Hansen, J. A. Staessen, C. Torp-Pedersen, S. Rasmussen, L. Thijs, H. Ibsen, and J. Jeppesen, “Prognostic Value of Aortic Pulse Wave Velocity as Index of Arterial Stiffness in the General Population,” Circulation, vol. 113, no. 5, pp. 664-70, 2006.

[141] D. Dubin, “Rapid Interpretation of EKG's: an Interactive Course,” Cover Publishing Company, 2000.

[142] H. Ashouri, and O. T. Inan, "Automatic Detection of Seismocardiogram Sensor Misplacement for Robust Pre-ejection Period Estimation in Unsupervised Settings”, IEEE Sensors Journal, vol. 17, no. 12, pp. 3805-3813, 2017.

[143] R. P. Patterson, "Fundamentals of Impedance Cardiography", IEEE Engineering in Medicine and Biology Magazine, vol. 8, no. 1, pp. 35-38, 1989.

[144] C. Li, Q. Chang, J. Zhang, and W. Chai, “Effects of Slow Breathing Rate on Heart Rate Variability and Arterial Baroreflex Sensitivity in Essential Hypertension,” Medicine (Baltimore), vol. 97, no. 18, pp. e0639–e0639, 2018.

[145] G. Tomei et al., “Occupational Exposure to Noise and the Cardiovascular System: A Meta-analysis,” The Science of the Total Environment, vol. 408, no. 4, pp. 681–689, 2010.

[146] J. Hayano and E. Yuda, “Pitfalls of Assessment of Autonomic Function by Heart Rate Variability,” Journal of Physiological Anthropology, vol. 38, no. 1, pp. 3–3, 2019.

[147] M. Malik et al., “Heart Rate Variability: Standards of Measurement, Physiological Interpretation, and Clinical Use,” Circulation (New York, N.Y.), vol. 93, no. 5, pp. 1043–1065, 1996.

[148] E. Kristal-Boneh, M. Raifel, P. Froom, and J. Ribak, “Heart Rate Variability in Health and Disease,” Scandinavian Journal of Work, Environment & Health, vol. 21, no. 2, pp. 85–95, 1995.

[149] J. Sztajzel, “Heart Rate Variability: A Noninvasive Electrocardiographic Method to Measure the Autonomic Nervous System,” Swiss Medical Weekly, vol. 134, no. 35–36, pp. 514–522, 2004.

[150] P. Karthikeyan, M. Murugappan, and S. Yaacob, “Detection of Human Stress Using Short-term ECG and HRV Signals,” Journal of Mechanics in Medicine and Biology, vol. 13, no. 2, pp. 1350038–1350029, 2013.

[151] S. Siecinski, E. J. Tkacz, and P. S. Kostka, “Comparison of HRV indices obtained from ECG and SCG Signals from CEBS Database,” Biomedical Engineering Online, vol. 18, no. 1, pp. 69–69, 2019.

[152] S. Sieciński, P. S. Kostka, and E. J. Tkacz, “Heart Rate Variability Analysis on Electrocardiograms, Seismocardiograms and Gyrocardiograms on Healthy Volunteers,” Sensors, vol. 20, no. 16, pp. 1–16, 2020.

[153] O. Postolache, P. S. Girao, and G. Postolache, “New Approach on Cardiac Autonomic Control Estimation Based on BCG Processing,” in 2007 Canadian Conference on Electrical and Computer Engineering, pp. 876–879, 2007.

[154] J. H. Shin and K. S. Park, “HRV Analysis and Blood Pressure Monitoring on Weighing Scale Using BCG,” 2012 Annual International Conference of the IEEE Engineering in Medicine and Biology Society, pp. 3789–3792, 2012.

[155] S. K. Jose, C. M. Shambharkar, and J. Chunkath, “HRV Analysis Using Ballistocardiogram with LabVIEW,” in 2015 International Conference on Computing and Communications Technologies (ICCCT), 2015, pp. 128–132.

[156] F. Li et al., “A Camera-based Ballistocardiogram Heart Rate Measurement Method,” Review of Scientific Instruments, vol. 91, no. 5, pp. 054105–054105, 2020.

[157] W. Lyu, S. Chen, F. Tan, and C. Yu, “Vital Signs Monitoring Based on Interferometric Fiber Optic Sensors,” Photonics, vol. 9, no. 2, pp. 50, 2022.

[158] L. Shen et al., “WaveFlex Sensor: Advancing Wearable Cardiorespiratory Monitoring with Flexible Wave-Shaped Polymer Optical Fiber,” IEEE Journal of Selected Topics in Quantum Electronics, pp. 1–8, 2023.

[159] S. Laborde, E. Mosley, and J. F. Thayer, “Heart Rate Variability and Cardiac Vagal Tone in Psychophysiological Research - Recommendations for Experiment Planning, Data Analysis, and Data Reporting,” Frontiers in Psychology, vol. 8, pp. 213–213, 2017.

[160] P. M. Lehrer and R. Gevirtz, “Heart Rate Variability Biofeedback: How and Why Does It Work?,” Frontiers in Psychology, vol. 5, pp. 756–756, 2014.

[161] C. Sevoz-Couche and S. Laborde, “Heart Rate Variability and Slow-Paced Breathing: when Coherence Meets Resonance,” Neuroscience and Biobehavioral Reviews, vol. 135, pp. 104576–104576, 2022.

[162] F. Shaffer and Z. M. Meehan, “A Practical Guide to Resonance Frequency Assessment for Heart Rate Variability Biofeedback,” Frontiers in Neuroscience, vol. 14, pp. 570400–570400, 2020.

[163] L. A. Fleisher, “Heart Rate Variability as An Assessment of Cardiovascular Status,” Journal of Cardiothoracic and Vascular Anesthesia, vol. 10, no. 5, pp. 659–671, 1996.

[164] F. Shaffer and J. P. Ginsberg, “An Overview of Heart Rate Variability Metrics and Norms,” Frontiers in Public Health, vol. 5, pp. 258–258, 2017.

[165] H.-G. Kim, E.-J. Cheon, D.-S. Bai, Y. H. Lee, and B.-H. Koo, “Stress and Heart Rate Variability: A Meta-analysis and Review of the Literature,” Psychiatry Investigation, vol. 15, no. 3, pp. 235–245, 2018.

[166] G. Parchani, G. Kumar, R. Rao, K. Udupa, and V. Saran, “Efficacy of Non-contact Ballistocardiography System to Determine Heart Rate Variability,” Annals of Neurosciences, vol. 29, no. 1, pp. 16–20, 2022.

[167] N. P. Novani, L. Arief, R. Anjasmara and A. S. Prihatmanto, "Heart Rate Variability Frequency Domain for Detection of Mental Stress Using Support Vector Machine," 2018 International Conference on Information Technology Systems and Innovation (ICITSI), Bandung, Indonesia, 2018, pp. 520-525.

[168] H. Cohen, M. A. Matar, Z. Kaplan, and M. Kotler, “Power Spectral Analysis of Heart Rate Variability in Psychiatry,” Psychotherapy and Psychosomatics, vol. 68, no. 2, pp. 59–66, 1999.

[169] T. Pham, Z. J. Lau, S. H. A. Chen, and D. Makowski, “Heart Rate Variability in Psychology: A Review of HRV Indices and An Analysis Tutorial,” Sensors, vol. 21, no. 12, p. 3998–, 2021.

[170] R. Castaldo, P. Melillo, U. Bracale, M. Caserta, M. Triassi, and L. Pecchia, “Acute Mental Stress Assessment Via Short Term HRV Analysis in Healthy Adults: A Systematic Review with Meta-Analysis,” Biomedical Signal Processing and Control, vol. 18, pp. 370–377, 2015.

[171] J. D. Blood et al., “The Variable Heart: High Frequency and Very Low Frequency Correlates of Depressive Symptoms in Children and Adolescents,” Journal of Affective Disorders, vol. 186, pp. 119–126, 2015.

[172] R. McCraty, M. Atkinson, W. A. Tiller, G. Rein, and A. D. Watkins, “The Effects of Emotions on Short-term Power Spectrum Analysis of Heart Rate Variability,” The American Journal of Cardiology, vol. 76, no. 14, pp. 1089–1093, 1995.

[173] M.-K. Yum, J.-T. Kim, and H.-S. Kim, “Increased Non-stationarity of Heart Rate During General Anaesthesia with Sevoflurane or Desflurane in Children,” British Journal of Anaesthesia: BJA, vol. 100, no. 6, pp. 772–779, 2008.

[174] P.W. Kamen, H. Krum, A.M. Tonkin, “Poincaré Plot of Heart Rate Variability Allows Quantitative Display of Parasympathetic Nervous Activity in Humans,” Clinical Science (Lond), vol, 91, no. 2, pp. 201-8, 1996.

[175] M. Bootsma, C. A. Swenne, H. H. Van Bolhuis, P. C. Chang, V. M. Cats, and A. V. Bruschke, “Heart Rate and Heart Rate Variability as Indexes of Sympathovagal Balance,” American Journal of Physiology. Heart and Circulatory Physiology, vol. 266, no. 4, pp. H1565–H1571, 1994.

[176] B. Silke and J. G. Riddell, “Heart Rate Variability Effects of An Agonist or Antagonists of the β-adrenoceptor Assessed with Scatterplot and Sequence Analysis,” Clinical Autonomic Research, vol. 8, no. 3, pp. 145–153, 1998.

[177] D. C. Michaels, D. R. Chialvo, E. P. Matyas, and J. Jalife, “Chaotic Activity in a Mathematical Model of the Vagally Driven Sinoatrial Node,” Circulation Research, vol. 65, no. 5, pp. 1350–1360, 1989.

[178] M. Brennan, M. Palaniswami, and P. Kamen, “Poincaré Plot Interpretation Using a Physiological Model of HRV Based on A Network of Oscillators,” American Journal of Physiology - Heart and Circulatory Physiology, vol. 283, no. 5, pp. 1873–1886, 200.

[179] A. B. Ciccone, J. A. Siedlik, J. M. Wecht, J. A. Deckert, N. D. Nguyen, and J. P. Weir, “Reminder: RMSSD and SD1 are Identical Heart Rate Variability Metrics,” Muscle & Nerve, vol. 56, no. 4, pp. 674–678, 2017.

[180] M. Brennan, M. Palaniswami, and P. Kamen, “Do Existing Measures of Poincare Plot Geometry Reflect Nonlinear Features of Heart Rate Variability?,” IEEE Transactions on Biomedical Engineering, vol. 48, no. 11, pp. 1342–1347, 2001.

[181] Y. İşler and M. Kuntalp, “Combining Classical HRV Indices with Wavelet Entropy Measures Improves to Performance in Diagnosing Congestive Heart Failure,” Computers in Biology and Medicine, vol. 37, no. 10, pp. 1502–1510, 2007.

[182] L. F. M. De Souza Filho et al., “Evaluation of the Autonomic Nervous System by Analysis of Heart Rate Variability in the Preterm Infants,” BMC Cardiovascular Disorders, vol. 19, no. 1, pp. 198–198, 2019.

[183] J. Brouwer et al., “Prognostic Value of Heart Rate Variability During Long-term Follow-up in Patients with Mild to Moderate Heart failure,” Journal of the American College of Cardiology, vol. 28, no. 5, pp. 1183–1189, 1996.

[184] S. Rahman, M. Habel, and R. J. Contrada, “Poincaré Plot Indices as Measures of Sympathetic Cardiac Regulation: Responses to Psychological Stress and Associations with Pre-ejection Period,” International Journal of Psychophysiology, vol. 133, pp. 79–90, 2018.

[185] M. H. Olsen et al., “A Call to Action and A Lifecourse Strategy to Address the Global Burden of Raised Blood Pressure on Current and Future Generations: the Lancet Commission on Hypertension,”

The Lancet (British edition), vol. 388, no. 10060, pp. 2665–2712, 2016.

[186] E. O'Brien et al., "Practice Guidelines of the European Society of Hypertension for Clinic, Ambulatory and Self Blood Pressure Measurement," Journal of Hypertension, vol. 23, no. 4, pp. 697–701, 2005.

[187] T. G. Pickering, G. A. Harshfield, H. D. Kleinert, S. Blank, and J. H. Laragh, "Blood Pressure During Normal Daily Activities, Sleep, and Exercise: Comparison of Values in Normal and Hypertensive Subjects," JAMA : the Journal of the American Medical Association, vol. 247, no. 7, pp. 992–996, 1982.

[188] R. Mukkamala et al., "Toward Ubiquitous Blood Pressure Monitoring via Pulse Transit Time: Theory and Practice," IEEE Transactions on Biomedical Engineering, vol. 62, no. 8, pp. 1879–1901, 2015.

[189] J. R. Banegas et al., "Relationship between Clinic and Ambulatory Blood-Pressure Measurements and Mortality," The New England Journal of Medicine, vol. 378, no. 16, pp. 1509–1520, 2018.

[190] Y.-L. Zheng, B. P. Yan, Y.-T. Zhang, and C. C. Y. Poon, "An Armband Wearable Device for Overnight and Cuff-Less Blood Pressure Measurement," IEEE Transactions on Biomedical Engineering, vol. 61, no. 7, pp. 2179–2186, 2014.